The Dissertation Committee for Mathew J. Boyer Certifies that this is the approved version of the following Dissertation:

Atomistic Simulation of the Early Stages of Solid Electrolyte Interphase Formation in Lithium Ion Batteries

Committee:

Gyeong S. Hwang, Supervisor

Benny D. Freeman

Arumugam Manthiram

Pengyu Ren

Atomistic Simulation of the Early Stages of Solid Electrolyte Interphase Formation in Lithium Ion Batteries

by

Mathew J. Boyer

Dissertation

Presented to the Faculty of the Graduate School of

The University of Texas at Austin

in Partial Fulfillment

of the Requirements

for the Degree of

Doctor of Philosophy

The University of Texas at Austin

August 2019

Dedication

To my mother and father, Paula and John Boyer.

Acknowledgements

I would first like to thank my advisor, Professor Gyeong S. Hwang, for his support and mentorship which allowed me to grow as a researcher and teacher. His enthusiasm for solving challenging fundamental problems and drive to conduct impactful research has provided me with many opportunities to learn as both a scientist and an engineer. I would like to thank Professor Arumugam Manthiram and Dr. Xingwen Yu for providing me with the opportunity to collaborate with them on several studies which have broadened my research interests. I thank my committee, Professor Arumugam Manthiram, Professor Benny Freeman, and Professor Pengyu Ren, for their interest and insight. Lastly, I want to thank past and present members of the Hwang Group, particularly Dr. Linas Vilčiauskas, Dr. Chia-Yun Chou, Dr. Eunsu Paek, Dr. Alex Pak, Dr. Yu-Hao Tsai, Dr. Haley Stowe, Myungsuk Lee, and Greg Hartmann.

Atomistic Simulation of the Early Stages of Solid Electrolyte Interphase Formation in Lithium Ion Batteries

Mathew J. Boyer, Ph. D.

The University of Texas at Austin, 2019

Supervisor: Gyeong S. Hwang

Lithium ion batteries have fueled a technological revolution in consumer electronics, power tools, and electric vehicles. Further advancements of this technology to improve charge times and capacity while maintaining safe operability, however, require a deeper fundamental understanding of electrode and electrolyte materials as well as their interfaces. In particular, interfacial stability between the high energy anode and the electrolyte represents one of the greatest hurdles to improving current-generation batteries as well as moving onto next-generation technologies like lithium metal or silicon. Despite the commercial availability of lithium ion batteries for more than a decade, there is no intrinsically stable electrolyte which is able to satisfy the design requirements of a commercial device. Instead, a protective layer formed during the first charge cycle known as the solid electrolyte interphase (SEI) is relied upon to ensure stable operation over subsequent charge/discharge cycles. Despite being critical to battery operability, the SEI and the process by which it forms remains poorly understood. As the SEI is only several to tens of nm thick and decomposes in ambient conditions, its study through experiments presents many challenges. However, computational tools can easily access the size- and time-scales required to elucidate the processes which govern the formation of the SEI. This dissertation presents a computational framework by which reductive decomposition of the electrolyte during the early stages of SEI formation may be studied through atomistic

simulations including classical molecular dynamics and density functional theory. Additionally, fundamental descriptions of several reaction and diffusion processes involved in the formation of the SEI from a conventional electrolyte on a graphite electrode are presented. This methodology may be later applied to more complex electrolytes or other electrodes like silicon, but also lays the groundwork for exploring later stages of the SEI formation and growth.

Table of Contents

List of Tables

List of Figures

Chapter 1 : Introduction

Since the invention of the lithium ion battery (LIB)[1], portable electronics have experienced a technological revolution. In comparison to previous secondary battery technologies like nickel-cadmium (NiCd) or nickel metal hydride (NiMH), LIBs are lightweight, operate at high voltages with large energy densities, possess long cycles lives, and exhibit low to no memory effect.[2–8] However, the growing demand for electric vehicles (EVs) is currently fueling a need for further increases in charge rate, cycle life, and energy density while maintaining safe operability.[9] Yet, the volumetric energy density (a critical parameter for EVs) of current LIBs is presently approaching its physiochemical limit[10] creating an impetus for development of new technologies which may allow for movement beyond the limitations of the original.

The original LIB consisted of a graphite anode[11] and a layered $LiCoO_2$ cathode[12] separated by a an electrolyte composed of a Li-containing salt dissolved in propylene carbonate (PC).[2] However, the electrochemical reduction of PC eventually results in the exfoliation and destruction of graphite electrodes.[13,14] Ultimately, this problem was alleviated through the substitution of PC with a new solvent, ethylene carbonate (EC), which differed only by the substitution of the methyl functional group with a H atom.[15,16] While neither solvent is electrochemically stable at electrode-electrolyte interface, the EC-based electrolyte was shown to produce a passivating layer during the first charge which protected the graphite electrode from being pulverized and thus the cell from failure: this

layer has been termed the solid electrolyte interphase (SEI).[17–25] Without the formation of an SEI layer, LIBs would require an electrolyte with an electrochemical stability window wide enough to prevent oxidation by the cathode and reduction by the anode; one of LIBs most beneficial qualities, their high operating voltages, makes satisfying this requirement nearly impossible without sacrificing other necessary qualities of the electrolyte.[4] Yet, much like the electrolyte itself, the properties of the SEI can influence those of the LIB; specifically, the SEI has been shown to affect the cell impedance,[26–30] irreversible capacity loss,[31,32] thermal stability,[33–36] and rate of capacity fade at higher charge rates[33]. However, despite its importance, a detailed understanding of the mechanism by which the SEI is formed and how factors such as operating temperature, cutoff voltage, voltage ramp-rate, bulk electrolyte composition, and additives effect it remains elusive.

The *in situ* formation of the SEI during the first cycle creates several challenges which must be overcome during its study. For example, it was shown that *ex situ* analysis of the SEI may result in secondary reactions with air or moisture changing its composition.[37–39] Furthermore, many of the proposed decomposition mechanism include radical intermediates[40] which may be short-lived and difficult to observe at time-scales accessible by experiments[41,42]. The large variation in SEI properties under different formation conditions suggest that its structure is highly dependent upon its formation process; by this account, there is no single SEI which can be studied, but rather a multitude of SEIs making fundamental understanding of this formation process critical to its improvement.

While the transient nature of electrochemical processes and the size- and time-scales at which they occur are prohibitive for many experimental techniques, computational techniques provide access to such spatial and temporal domains[43–45]. Over the past few decades, advances in both computing power and algorithms have expanded the capabilities of simulation tools greatly. By combining basic understanding of nanoscale structure, transport phenomena, and reaction systems with experimental data, current-generation batteries may finally be fully understood and the insights gained could lead to the development of next-generation secondary batteries. In this dissertation, the early-stages of SEI formation in LIBs and the factors which influence it are explored through the application of classical molecular dynamics and quantum mechanical simulations. The theoretical background of these methods as well as some enhanced sampling techniques employed within them are introduced in Chapter 2.

In Chapter 3, the electrode/electrolyte interface structure is described for a conventional mixed carbonate electrolyte at a graphite edge plane surface prior to the initial reduction of the electrolyte. Here, the effect of electrode polarization due to the application of a potential by an external voltage source on the distribution of electrode species at the interface is discussed. For the remainder of this dissertation, benchmark potentials described in this chapter are used to correlate electrode surface charge density to this applied potential relative to the Li/Li^+ electrochemical couple. Particular attention is placed on the composition of the first electrolyte layer of the interfacial structure at the onset potential of electrolyte reduction which ultimately results in the formation of the SEI. Additionally, an

approach to modeling ion transport near a solid/liquid interface is demonstrated through prediction of Li^+ cation transport behavior.

Chapter 4 then focuses on the reductive decomposition of EC prior to its incorporation into the SEI layer. Here, the selective reduction of EC in mixed carbonate systems is analyzed through quantum mechanical calculations. By combining the description of the interfacial structure at the reduction potential from Chapter 3 with these results, simulations may explain the experimental observation that SEI primarily consists of EC-based species[38,46–48]. The remainder of the chapter focuses on description of the thermodynamics and kinetics of the reduced EC ring-opening reaction and the factors that influence it in order to elucidate its role in SEI formation. Within this analysis, the importance of representing the complex environments within LIBs in as much detail as computationally feasible (specifically representing solvent with explicit molecules) for accurate prediction of reaction energetics is highlighted.

Next, in Chapter 5 the transport behavior of the reduced EC intermediate is evaluated near a graphite electrode prior to the formation of the SEI. Particular attention is paid to the effects of the applied potential and the electrolyte composition on the diffusion of the intermediate away from the electrode. The difference in mobility near the interface prior to and after ring-opening is compared to demonstrate the impact of ring-opening kinetics discussed in Chapter 4 on the parasitic loss of capacity by diffusion of charged intermediates away from the anode. The effect of intermediate diffusion behavior only the final decomposition product is also discussed within this chapter.

Chapter 6 describes the interaction between reduced EC intermediates in solution (both in bulk and near the interface) prior to bimolecular reaction to form alkyl carbonates as well as the reactions by which ethylene dicarbonate and butylene dicarbonate are formed. In particular, the effect of local concentration on the aggregation of the anion intermediate is studied in detail as well as the resulting aggregate structures likely to form during the early stages of SEI formation. These structures are then used as the basis for investigation of the bimolecular reactions to form the alkyl carbonate products and the reaction energetics between the two pathways are compared.

Finally, Chapter 7 summarizes the computational framework outlined in this dissertation and the findings of its application to the study of the early stages of SEI formation by the reductive decomposition of an electrolyte composed of EC, DMC, and $LiPF_6$ at a graphite anode. Future opportunities for extension of this framework to the later stages of SEI formation as well its application to better understanding influencing factors on the early stages of SEI formation, such as the inclusion of additives, are then discussed.

Chapter 2 : Theoretical Background

2.1 Quantum Mechanical Methods

In order to evaluate chemistry from first-principles, a quantum level description is required. The most fundamental level at which a system may be reasonably described here is by the time-independent Schrödinger Equation:

$$\hat{H}\Psi(r) = E\Psi(r) \tag{2.1.1}$$

where $\Psi(r)$ is the wave function, $\hat{H}$ is the Hamiltonian operator, and E is the energy. For a many-body system consisting of both electrons and nuclei, $\Psi(r)$ is a function of the positions of both the electrons and nuclei. $\hat{H}$ may be decomposed into a linear combination of the potential ($\hat{V}$) and kinetic ($\hat{T}$) energy operators.

$$\hat{H} = \hat{V} + \hat{T} \tag{2.1.2}$$

$\hat{V}$ consists of the sum of all electron-electron, electron-nucleus, and nucleus-nucleus Coulombic interactions:

$$\hat{V} = (1/2\sum e^2/|r_i - r_j|^2 - \sum Ze^2/|r_i - R_m| \sum Z_m Z_n e^2/|R_m - R_n|)/4\pi\varepsilon_0 \tag{2.1.3}$$

where r and R are the positions of electrons and nuclei in space, e is the charge of an elementary particle, Z is the atomic number of the atom in which the nucleus resides, and ε_0 is the permittivity of free space. Similarly, $\hat{T}$ is given by the sum of all particle kinetic energies:

$$\hat{T} = (-\hbar^2/2m_e)\sum\nabla^2 + (-\hbar^2/2)\sum M_m\nabla^2 \tag{2.1.4}$$

where $\hbar$ is the reduced Planck's constant, m_e is the electron mass, M_m is the atomic weight of the nuclei, and ∇^2 is the Laplacian. Due to the relative masses between electrons and atomic nuclei, it is convenient to assume that the nuclei are stationary relative to electron motion thus allowing for the second term to be ignored in what is referred to as the Born-Oppenheimer approximation[49]. Yet even with this approximation, the exact solution of the Schrödinger Equation may only be arrived at for very small numbers of particles. In order to reform the Schrödinger Equation such that it may be solved for relevant systems, additional degrees of freedom must be eliminated.

Although several approaches are widely used to solve this issue, density functional theory (DFT)[50–52] is the workhorse of quantum mechanical methods for chemistry applications. DFT is fundamentally based upon the Hohenberg-Kohn theorem[53] which states that for the electronic ground state of an interacting electron gas, a universal functional ($f(\mathrm{n}(r))$) of the electron density ($\mathrm{n}(r)$) exists which is independent of the static potential ($\mathrm{v}(r)$) and that the expression:

$$E \equiv \int \mathrm{v}(r)\mathrm{n}(r)\mathrm{d}\mathrm{r} + f(\mathrm{n}(r)) \tag{2.1.5}$$

possesses a minimum value which is the ground-state energy for a given external potential. Therefore, for a given functional, $\mathrm{n}(r)$ may be arrived at by the variational principle and Equation 2.1.5. Within density functional theory, this equation becomes:

$$E \equiv \mathrm{T_s}(\mathrm{n}(\mathrm{r})) + \mathrm{E_{coul}}(\mathrm{n}(\mathrm{r})) + \mathrm{E_{ext}}(\mathrm{n}(\mathrm{r})) + \mathrm{E_{xc}} \tag{2.1.6}$$

where $\mathrm{T_s}$ is the kinetic energy of a noninteracting electron cloud, $\mathrm{E_{coul}}$ is the Coulombic energy of the interacting electron cloud, $\mathrm{E_{ext}}$ is the interaction energy between an external

potential and the electron cloud, and E_{xc} is the exchange-correlation energy which typically also includes the kinetic energy difference between an interacting and noninteracting electron cloud.

$$E_{coul}(n(r)) = 1/2\iint n(r)n(r')/|r-r'|\, drdr' \quad (2.1.7)$$

$$E_{ext}(n(r)) = \int v_{ext}(r)n(r)\, dr \quad (2.1.8)$$

Of the four terms, E_{xc} is unknown and it may be a function of n(r) (the local density approximation) or both n(r) and the gradient of n(r) which is termed the generalized gradient approximation (GGA):

$$E_{xc}^{GGA} = \int \varepsilon_{xc}(n(r),\nabla n(r))\, dr \quad (2.1.9)$$

As this term possesses the bulk of assumptions, it must be carefully selected based upon the properties most important to the study.

2.2 Classical Force Fields

While first-principles methods provide chemical resolution necessary for describing bond breaking/forming in chemical reactions, polarization effects, and charge transfer processes where the electrons are explicitly involved, this resolution comes with a large simulation cost despite the simplifications made by methods such as DFT. For nonreactive systems, simplification may allow access to larger size- and time-scales with only minor sacrifice to accuracy through describing inter- and intra-molecular interactions through equation-based potentials where the total potential (U_{tot}) is given by:

$$U_{tot} = U_{bond} + U_{ang} + U_{dih} + U_{imp} + U_{vdw} + U_{coul} \quad (2.2.1)$$

where U_{bond}, U_{angle}, U_{dih}, and U_{imp} govern 2-, 3-, and 4-body interactions between atoms in a molecules which are connected by bonds as shown in Figure 2.1.

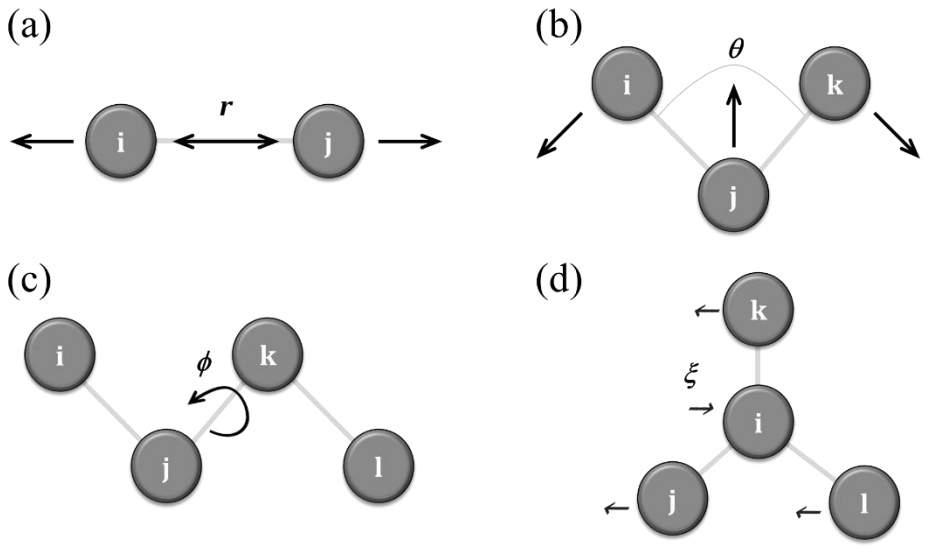

Figure 2.1. Diagram of particle interactions governed by the bond length *r* between atoms i and j (a), by the angle θ between atoms i, j, and k where i and k are separate by two bonds (b), by the proper dihedral angle ϕ between atoms i, j, k, and l where atoms i and l are separated by three bonds (c), and by the improper dihedral angle ξ between atoms i, j, k, and l where atoms j, k, and l are each bonded to atom i (d).

Popular force fields such as the generalized Amber force field (GAFF)[54] and the optimized potentials for liquid simulations (OPLS)[55], utilize a ball and spring model where a bond between two atoms is represented by a harmonic potential function of the bond distance (r) with a spring constant k_{bond} centered at the equilibrium bond length (r_0):

$$U_{bond} = 1/2 k_{bond} (r\text{-}r_0)^2 \qquad (2.2.2)$$

Similarly, 3-body interactions between atoms separated by two bonds are described by a harmonic potential function of the angle (θ) with a spring constant k_{angle} centered at the equilibrium angle (θ_0):

$$U_{angle}=1/2k_{angle}(\theta-\theta_0)^2 \quad (2.2.3)$$

Proper and improper dihedral potentials for 4-body interactions vary more considerably across different force fields. In this dissertation, the all-atom OPLS (OPLS-AA) is used which has U_{dih} and U_{imp} potentials:

$$U_{dih}=1/2[\sum F_n(1+\cos(n\phi)] \quad (2.2.4)$$

$$U_{imp}=1/2k_{imp}(\xi-\xi_0)^2 \quad (2.2.5)$$

where $\sum$ indicates summation from n = 1 to 5, F_n are force constants, k_{imp} is the spring constant for the harmonic improper function, and ξ_0 is the equilibrium improper angle. Nonbonded interactions between atoms separated by a distance r are divided into van der Waals interactions which are described by the Lennard Jones potential:

$$U_{vdw} = 4\varepsilon[(\sigma/r)^{12} - (\sigma/r)^6] \quad (2.2.6)$$

where σ and ε are distance and energy constants, and electrostatic interactions which are described by the Coulombic potential:

$$U_{coul} = q_iq_j/4\pi\varepsilon_0 r \quad (2.2.7)$$

where q_i and q_j are the partial atomic charges of atoms i and j. For classical force fields, parameters may be derived from a top-down approach where constants are chosen such that experimental data may be reproduced by the model, by a bottom-up approach where

constants are fit to data from quantum mechanical simulation data, or by some mix of the two approaches.

2.3 Molecular Dynamics

For both quantum mechanical and classical methods, the interaction potential acting upon an atom is related to the force on the atom by the negative of its spatial derivative. For quantum mechanical approaches, this manifests as the expectation value of the gradient of the ground-state electronic Hamiltonian.[56] For classical force fields, all the potentials are functions of distance (or angles which are themselves functions of distance) and can therefore have easily obtained analytical derivatives with respect to position. These positions can then be propagated over time according to Newton's second law of motion:

$$F = ma = md^2r/dt^2 \tag{2.3.1}$$

where the force (F) is equal to the mass (*m*) multiplied by the acceleration which is equivalent to the second derivative of position (r) with time (t). For a many-body system, this problem may be numerically solved to propagate the molecular trajectory through time by finite increments referred to as timesteps (dt) using the Verlet algorithm[57] which originates from a Taylor series expansion of Equation 2.3.1 around t + dt and t - dt:

$$r(t+dt) = r(t) + dt\, r'(t) + dt^2/2\, r''(t) + dt^3/3\, r'''(t) + O(dt^4) \tag{2.3.2}$$

$$r(t-dt) = r(t) - dt\, r'(t) + dt^2/2\, r''(t) - dt^3/3\, r'''(t) + O(dt^4) \tag{2.3.3}$$

if these two equations are added together and fourth order terms and higher are discarded, a simple equation for position at t + dt it is a function of the position at the current and previous timestep and the force at the current timestep:

$$r(t+dt) = 2r(t) - r(t-dt) + F(t)/m \quad (2.3.4)$$

As stated previously, forces may be determined for any geometry based upon atomic positions. By a similar Taylor series expansion the atomic velocities (v) at t + dt are given by:

$$v(t+dt) = v(t) + dt\,[F(t+dt) + F(t)]/2m \quad (2.3.5)$$

such that this algorithm may be propagated through time as quickly as forces may be calculated.

If all interactions are pairwise and elastic, total energy and momentum will be conserved and the simulation will sample within the microcanonical (NVE) ensemble. However, to model realistic systems, it is more useful to control temperature than total energy, and therefore, sample the canonical (NVT) ensemble. This can be achieved through assuming the simulation box is coupled with an external heat bath referred to as a thermostat. As heat is exchanged between molecules and the bath, velocities change such that the kinetic energy remains constant. However, the velocities may be changed by a variety of algorithms. The simplest is to rescale velocities uniformly, however, this does not allow for continuous dynamics. Instead to maintain continuous dynamics, the Nosé-Hoover thermostat[58–60] utilizes a fictitious friction term which is proportional to the kinetic energy to ensure it remains constant and that the canonical ensemble is sampled.

2.4 Metadynamics

While molecular dynamics simulations are a powerful simulation tool, they face limitations which limit their application to systems with fairly flat energy landscapes where the phenomena of interest can be adequately sampled within the limited timescales feasible. For systems where adequate statistical sampling can be achieved, the Helmhotz free energy (*A*) profile along a collective variable (CV), s, may be approximated by the potential of mean force (PMF)[61,62]:

$$A(s) = A(s^*) - k_B T \ln(\langle \rho(s) \rangle / \langle \rho(s^*) \rangle) \quad (2.4.1)$$

Where $A(s^*)$ and s^* are arbitrary functions, k_B is the Boltzmann constant, T is temperature, and $\langle \rho(s) \rangle$ is the average distribution function. However for systems with energy landscapes containing multiple minima, especially those separated by significant kinetic barriers, it may not be possible to produce $\langle \rho(s) \rangle$ due to sampling constraints. Furthermore, the error in $A(s)$ would be inversely proportional to $\langle \rho(s) \rangle$ resulting in large errors for low probability states, such as transition states. One approach to overcoming sampling issues is the imposition of an external bias which may serve to flatten the energy landscape allowing for better sampling.[62,63]

One such bias method is the metadynamics algorithm[64] which dynamically alters the bias potential, $V(s,t)$, based on the residence time of the simulation along the CV space through the deposition of Gaussian hills at discrete time intervals and is given by:

$$V(s,t) = \sum W \exp(-|s-s(t')|^2/2\sigma^2) \quad (2.4.1)$$

where W is the Gaussian hill height, σ is the width, s(t′) is position along the CV space at the time of hill deposition, and $\sum$ indicates summation over the time history of hill deposition. For a simulation where a minimum occurs along s such that it is repeatedly sampled, energy will be added to the bias potential at the sampled position until energy landscape is flattened sufficiently for the state to be escaped and a new minimum sampled. At long enough simulation time, the free energy landscape will become entirely flat such that the simulation becomes ergodic in the CV space. Here A(s) may be found by the inversion of the bias potential:

$$V(s) = -A(s) \tag{2.4.2}$$

however, as hills will continue to be deposited, A(s) will continue to fluctuate around the converged profile. An alternative version of metadynamics is the so-called well-tempered scheme[65] where the Gaussian hill height is decayed over the course of the simulation such that V(s) smoothly converges. The exact form of the bias potential here is given by:

$$V(s,t) = \sum W \exp(-V(s,t')/\Delta T) \exp(-|s-s(t')|^2/2\sigma^2) \tag{2.4.3}$$

where W is the initial hill height, V(s,t′) is the value of the bias potential at the time of hill deposition, and ΔT is a differential temperature which controls the rate of hill decay. For very long simulation time, the bias potential is related to A(s) by:

$$V(s,t\rightarrow\infty) = -\Delta T\, A(s)/(T+\Delta T) \tag{2.4.4}$$

and has been shown to asymptotically converge[66].

Chapter 3 : Electrolyte Structure near Graphite Electrodes prior to Solid Electrolyte Interphase Formation

3.1 INTRODUCTION

Unlike lithium metal batteries, both electrodes in lithium ion batteries (LIBs) are initially stable during cell assembly.[2,5] As $LiCoO_2$ (or another Li-containing metal oxide) serves as the Li-source, the cell is assembled in the discharged state and the graphite anode is unreactive prior to charging. However, as the anode is polarized to more negative potentials its reactivity increases eventually leading to the reduction of the electrolyte prior to Li^+ intercalation into the graphite (if it occurs) for a range of electrolytes based on aprotic polar organic solvents.[15,16,31,67,68] Despite their similar molecular structures, propylene carbonate (PC) and ethylene carbonate (EC) have been shown to differ immensely in their performance as solvents in LIBs.[8,23] While Li^+ intercalation is only observed for PC-based electrolytes with high salt concentrations[39,69], additives[70], or when the anode is precycled in a different electrolyte[71], EC-based electrolytes allow for Li^+ intercalation after some initial irreversible capacity loss[15,16]. For mixtures of EC and PC, it was observed that after some initial reduction of the electrolyte where gas is evolved that Li^+ intercalation may eventually occur when the gas evolution ceases.[72]

Work in this chapter was published in Boyer, M. J.; Vilčiauskas, L.; Hwang, G. S. *Phys. Chem. Chem. Phys.* **2016**, *18* (40), 27868–27876. L.V. and G.S.H. contributed in part to the planning of the study and writing of the manuscript.

These observations indicate that while PC-based electrolytes may be continuously reduced, minor alteration of the molecular structure to EC allows for the formation of a stable passivating layer which allows for lithiation of the graphite electrode, and thusly charging of the LIB. A similar layer is formed on the surface of lithium metal electrodes due to its reactivity with organic solvents and is referred to as the solid electrolyte interphase (SEI).[17] Despite its tendency to form a stable interface, EC is a solid at room temperature[73] which has since led to its used with an acyclic carbonate cosolvent such as dimethyl carbonate (DMC) which is miscible with EC in any proportion[74,75]. Such mixed carbonate electrolytes were shown to produce a stable SEI allowing for lithiation of the graphite anode[31,67] and have since become the standard for LIBs[2–8].

The lack of such a stable, reliable SEI continues to limit the use of higher energy density anode materials such as Si[76] and Li metal[77], yet a detailed description of its formation in commercial LIBs remains elusive despite decades of study. In order to enable next-generation anodes, improved fundamental understanding of the underlying processes of SEI formation is critical. In order to build up such an understanding, computational tools may be leveraged for the study of the interfacial stucture[78–81] during electrode polarization before the initial charge transfer reactions occur. As these reactions have been proposed to occur by outer shell electron transfer,[82,83] the electrolyte species nearest the anode would be reduced at the highest rates[84]. Furthermore, highly oriented pyrolytic graphite (HOPG) has been shown to exhibit several orders of magnitude faster electron transfer kinetics at

edge surfaces when compared to the basal surface for outer shell reactions.[85] Therefore, in order to adequately describe the initial reduction process for SEI formation, the interface between the edge plane of a polarized graphite electrode and the EC/DMC electrolyte is necessary.

In this chapter, the graphite electrode/electrolyte interface is examined for a range of charge states of the electrode using classical molecular dynamics simulations. Electrolyte restructuring due to the electric field induced by excess charge at the interface is investigated in detail and a correlation between excess surface charge density and applied potential is established. The effect of the electric field as well as electrolyte reorganization on Li^+ transport properties near the interface are also examined here. The fundamental findings illustrate the relationship between local structure and transport phenomena critical to both the SEI formation process as well as Li^+ shuttling during charge/discharge cycles.

3.2 METHODOLOGY

In this work, classical molecular dynamics simulations were carried out using the OPLS-AA force field[86–88] and the GROMACS simulation package (version 4.6.7)[89]. Systems were constucted with a model graphite anode composed of 10 graphene nanoribbons with H-terminated zigzag edges arranged in an ABAB stacking structure. The graphite electrode was placed in a periodic rectangular simulation box such that the graphene sheets are stacked along the *y*-axis and the *sp2* carbon bonding spans across the periodic boundary along the *x*-axis; the zigzag edge surface is parallel to the *z*-axis. The *x*-

and *y*-axes of the simulation box are set to the dimension of the graphite stack (35 Å × 34 Å) and the remainder of the box in the *z*-dimension is filled with a model electrolyte consisting of 57 Li^+/PF_6^- ion pairs, 375 EC molecules, and 375 DMC molecules (1M $LiPF_6$ in 50/50 EC/DMC electrolyte). This half-cell configuration is shown in Figure 3.1.

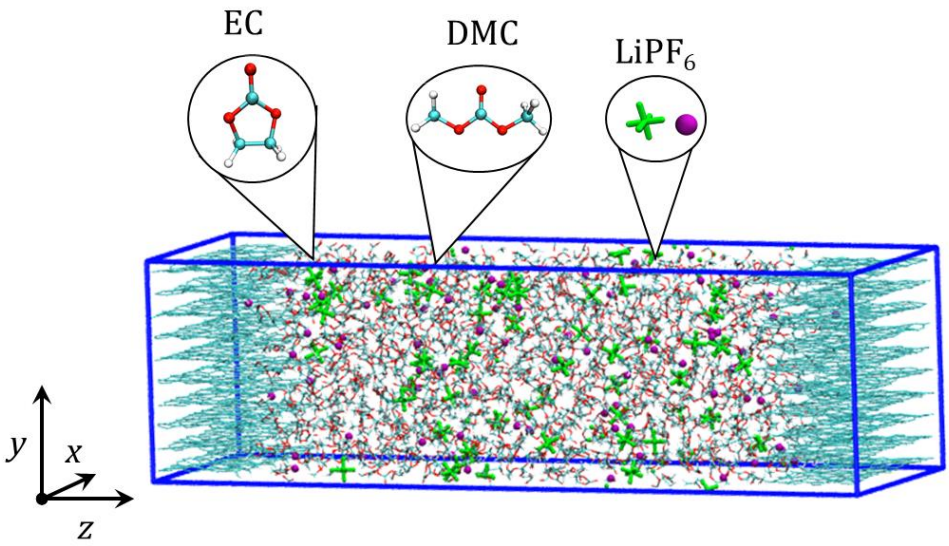

Figure 3.1. Illustration of the half-cell configuration simulation cell where the electrolyte consisting of EC, DMC, and $LiPF_6$ is sandwiched along the z-axis between stacks of graphene nanoribbons ordered in the ABAB configuration along the *y*-axis. C, O, H, and Li atoms are represented by cyan, red, white, and purple spheres, respectively, and PF_6^- anions are represented as green octahedrons.

For all simulations, a timestep of 1 fs was used for time integration. A spherical cutoff of 12 Å was applied to short-range nonbonded interactions and long-range electrostatic interactions were considered through the 3D particle mesh Ewald (PME) summation method. The electrode/electrolyte system density was equilibrated through MD simulations conducted within the NPT ensemble[90,91] prior to annealing at 700K within the NVT ensemble for at least 1 ns prior to quenching to 300K for at lease 0.5 ns before

production runs (all at 300K) were carried out. During all simulations, several C atoms within near the center of each graphene sheet were restrained through the application of a harmonic potential centered around each atom's initial *z*-position to prevent slipping due to the limited system size and weak van der Waals interactions between graphene sheets; this results in the maintenance of an ordered corrugated surface in contact with the liquid electrolyte. Simulations for obtaining interfacial structures were carried out for 10 ns.

Metadynamics simulations were carried out using the well-tempered algorithm as implemented in the PLUMED plugin[92]. For each simulation, the *z* position of a Li^+ cation chosen at random was biased for at least 70 ns of simulation time. To ensure adequate sampling within this time and to prevent Li^+ from moving into the graphite stack, harmonic walls were used to place upper and lower bounds on the *z*-position of the biased Li^+ limiting it to a 3 nm window. Gaussian hills with initial heights of 0.1 eV and widths of 0.5 Å were deposited every 0.1 ps; hill height was decayed by the well-tempered approach based on a ΔT of 7200K.

3.3 Results and Discussion

Reductive decomposition of the electrolyte on graphite electrodes occurs prior to the Li intercalation potential of ~0.2 V *vs*. Li/Li^+ when the Fermi level of graphite is raised above the lowest unoccupied molecular orbital (LUMO) energy of one or more of the electrolyte components.[4,31] As the rate of electron transfer decays exponentially with the molecule's distance from the electrode,[82,84] the interfacial structure would also effect the

electrolyte reduction. The following sections describe the interfacial structure of a graphite electrode immersed in a 1M $LiPF_6$ in 50/50 EC/DMC electrolyte at various applied potentials and the importance of structural changes due to potential.

3.3.1 Electrolyte Distribution near Graphite Electrodes

Figure 3.2 shows the number density (ρ_n) profiles for the electrolyte components (based on each molecule's center of mass) along the direction perpendicular to the graphite edge plane (z); the electrode is initially treated as net neutral in charge. At the interface, EC and DMC are shown to pack more densely by 2 and 3 times their bulk values, respectively. This appears to be the result of the van der Waals (vdW) interactions between the molecules and the H-terminated graphite edge. The observed preference towards the DMC can then be attributed to the stronger vdW interactions between its bulky methyl groups and the electrode. While oscillatory near the interface, ρ_n flattens beyond z = 20 Å becoming bulk-like in nature.

The first Li^+ peak appears at $z \approx 7$ Å where the ρ_n of EC and DMC exhibit minima; unlike the solvent molecules, the first Li^+ peak is markedly beneath the bulk-like density. The depletion of Li^+ cations near the interface implies the packing of solvent molecules near the electrode results in the incursion of an energy penalty for the rearrangement around Li^+ in a solvation shell; in bulk solution Li^+ tends to be surrounded by four carbonate species, in particular their carbonyl O (O_C) atoms, and one PF_6^- anion, as illustrated in the inset of Figure 3.2. The slight second maximum of the first EC/DMC peaks at z = 5.5 Å

may be attributed to ordering around the Li^+ as well as the corrugation of the graphite surface, while the second peak at z = 8.2 Å results from the interplay between solvation of Li^+ and vdW and Coulombic interactions with the first layer of solvent molecules. The ρ_n of Li^+ and PF_6^- exhibit pronounced alternating cation/anion layers similar to what is seen in ionic liquids[93] due to their electrostatic attraction.

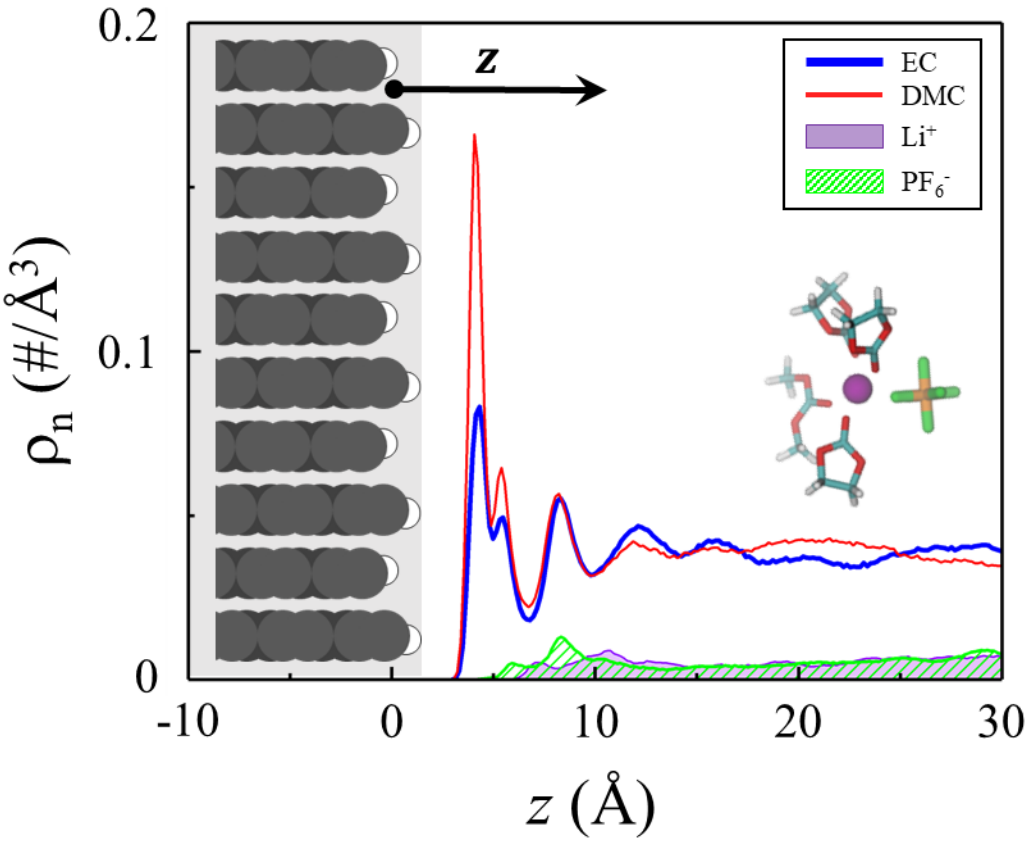

Figure 3.2. Number density (ρ_n) profiles of EC (blue), DMC (red), Li^+ (purple), and PF_6^- (green) based upon each molecule's center of mass position along the z-axis perpendicular to the graphite electrode surface as indicated by the schematic. A representative Li^+ solvation sheath structure from the bulk electrolyte is shown in the inset.

The Fermi level of the electrode may be shifted by the application of a potential by an external voltage source resulting in an excess or depletion of electrons relative to the open

circuit state; density functional theory (DFT) has shown that the excess/depletion of charge primarily localizes at the metallic edges of graphite[94]. This charge injection effect may be imitated by the assignment of excess charge to the electrolyte-adjacent carbon atoms resulting in an excess surface charge density (σ). The state wherein $\sigma = 0$ $\mu C/cm^2$ is referred to as the potential of zero charge (PZC, ϕ_Z) which is known to be approximately 3 V *vs.* Li/Li^+ (or 0 V *vs.* standard hydrogen electrode)[95,96]. In order to investigate the interfacial structure at potentials relevant to LIB chemistry, σ was varied between 0 and -16.4 $\mu C/cm^2$. The additional negative charge may be compensated by the addition of Li^+ cations to the bulk electrolyte; excess Li^+ cation can be assumed to originate from the cathode in a LIB full cell.).

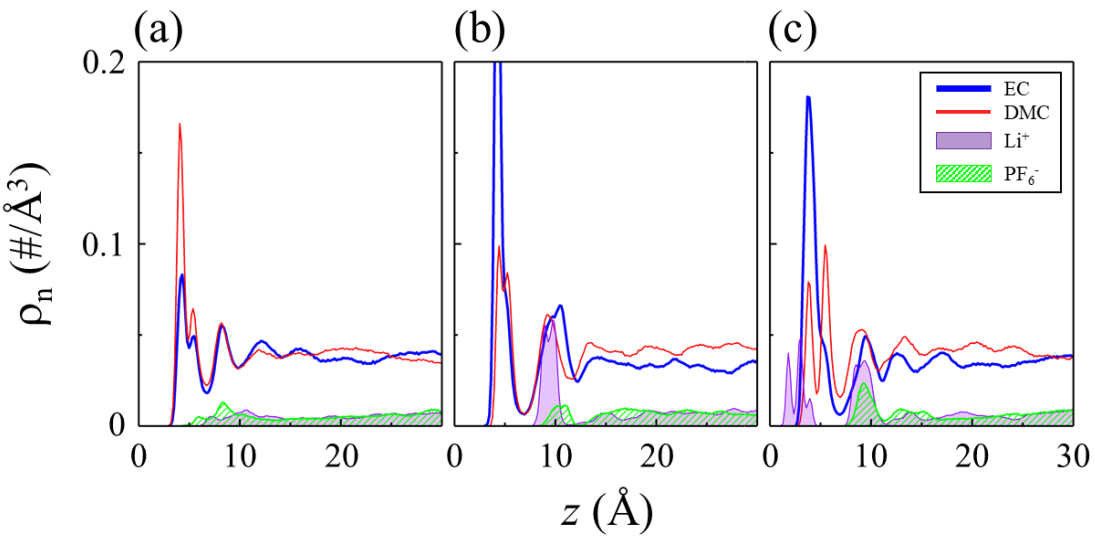

Figure 3.3. Number density (ρ_n) profiles of EC (blue), DMC (red), Li^+ (purple), and PF_6^- (green) along the direction normal to the electrode surface (z) for graphite electrodes with surface charge densities for $\sigma = 0$ $\mu C/cm^2$ (a), -11.6 $\mu C/cm^2$ (b), and -16.4 $\mu C/cm^2$ (c).

The injection of excess charge at the interface induces an electric field, which causes the electrolyte molecules to rearrange near the electrode such that they may screen the field lowering the energy of the system. Representative ρ_n profiles for $\sigma = 0$ $\mu C/cm^2$ [(a)], -11.6 $\mu C/cm^2$ [(b)], and -16.4 $\mu C/cm^2$ [(c)] are shown in Figure 3.3; those of intermediate σ values may be found in the Supporting Information of ref 80 for a more detailed description. When σ = -11.6 $\mu C/cm^2$ [(b)], the first peaks in ρ_n for EC and DMC shift towards lower *z* values (closer to the electrode) which may be attributed to greater ordering at the interface. The magnitudes of the first peak of EC and DMC at z = 4.3 Å are increased four-fold and halved relative to [(a)], respectively. The electric field emanating from the electrode causes the reorganization of the electrolyte at the interface wherein DMC molecules are replaced by EC, which has a significantly larger dipole moment[97,98] and a smaller molar volume allowing it to pack more densely at the interface to efficiently screen the field. Figure 3.4 shows the ρ_n profiles of the O_C atom and the ethylene group of EC; the overlapping first peaks in [(a)] illustrate the lack of orientational preference of EC near the neutral electrode while the segregation of peaks in [(b)] indicates a uniform ordering of O_C atoms away from the negatively charged electrode. This ordering of EC molecules in the first layer results in the accumulation of Li^+ cations from z = 9 - 10 Å resulting in ρ_n approximately 10 times the bulk value; the ordering of Li^+ results in a pronounced Li^+/PF_6^- cation/anion layering.

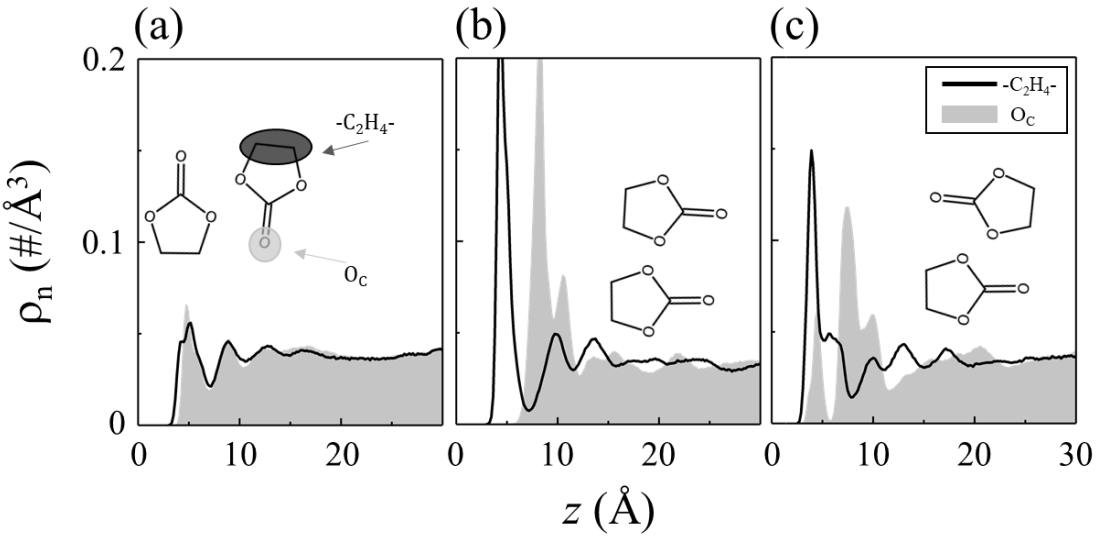

Figure 3.4. Decomposed number density (ρ_n) profiles of EC along the direction normal to the electrode surface (z) for graphite electrodes with surface charge densities for σ = 0 $\mu C/cm^2$ (a), -11.6 $\mu C/cm^2$ (b), and -16.4 $\mu C/cm^2$ (c) for the C_2H_4 group (black) and the carbonyl O atom (grey). Schematic representations of the EC molecules orientations are shown in each inset.

At more negative charge states such as σ = -16.4 $\mu C/cm^2$ [(c)], Li^+ cations can be observed at the graphite edges once the electric field can no longer be screened by the solvent molecules. This can be seen in the ρ_n peak from z = 1.9 - 4 Å not present in [(a)] or [(b)]. This peak exhibits three maxima which may be attributed to the corrugation of the graphite edge and the H terminations which allow for multiple stable sites for Li^+ depending on its solvation structure. The peak characteristic of Li^+ accumulation due to O_C ordering can be found closer to the electrode at z = 8.5 - 9.5 Å. Figure 3.4(c) exhibits two peaks for the O_C atom indicating the presence of Li^+ at the graphite edge disrupts the ordering of EC molecules at the interface as the Li^+ cations must still be partially solvated by EC (or DMC); the shift of the second Li^+ peak towards the electrode may be the result

of this disruption of the ordered EC layer. It should also be noted that the accumulation of Li^+ on the electrode also reduces the ρ_n of EC while increasing that of DMC in the first layer. Previous work performed with DFT has shown that the orientation of EC may be related the favorability of its decomposition[99] indicating this structural transition could potentially effect the solvent decomposition during SEI formation.

The field-induced reorganization of the electrolyte near a graphite electrode may be more generally described by the relative surface population of electropositive groups/atoms, namely the ethylene group of EC, the methyl groups of DMC, and the Li^+ cations. Integration of ρ_n yields the areal density which is shown in Figure 3.5 as a function of σ for the electropositive species. At neutral of near-neutral electrode charge states, DMC methyl groups are shown to be dominant, but as the electrode is charged further the EC ethylene groups become more populous at the interface. A similar effect was observed near graphene basal surfaces by Vatamanu *et al.* [100] where EC concentration was shown to monotonically increase with negative potential. However, beyond a critical σ the EC packing density reaches a maximum and begins to decrease as Li^+ cations begin to accumulate at the interface and EC ethylene groups are again replaced with DMC methyl groups. Atomistic level understanding of the electrode/electrolyte interfacial structure for different electrolyte compositions and operating conditions may provide valuable insights to the early stages of SEI formation.

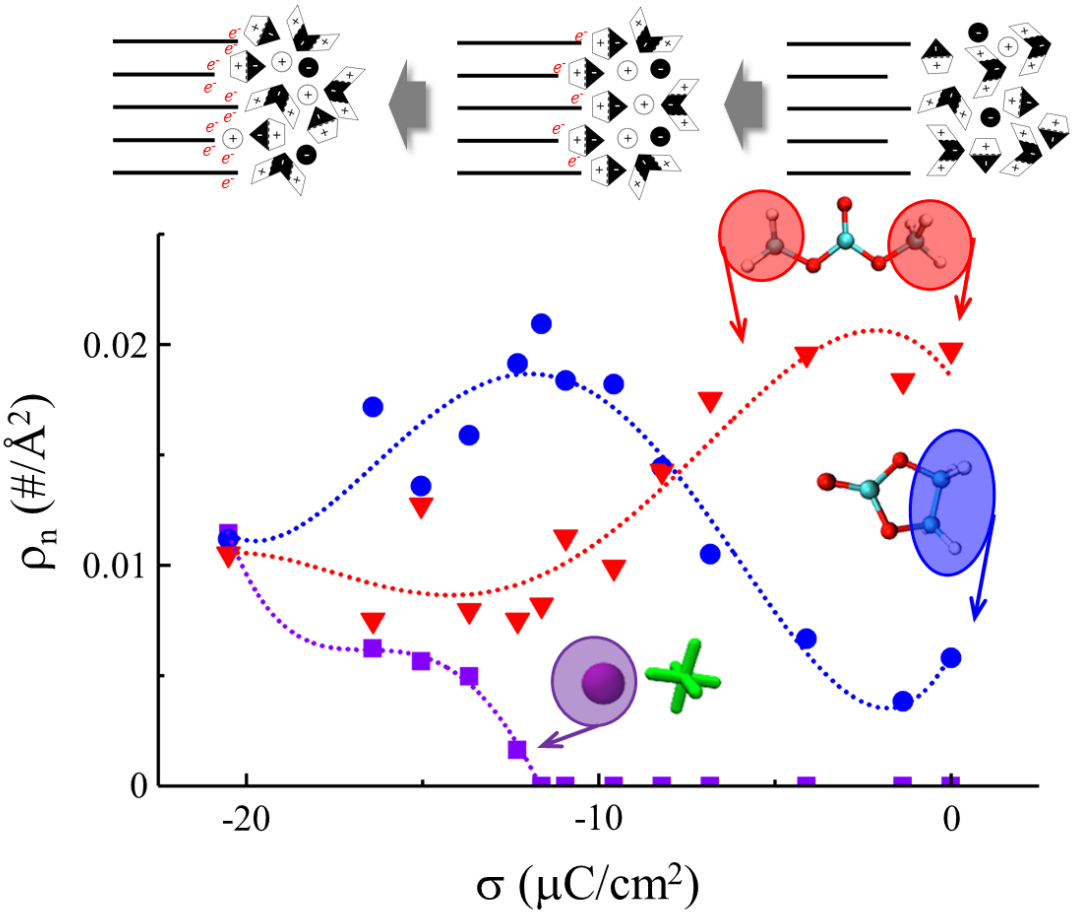

Figure 3.5. Variation in the number density (ρ_n) of functionalities bearing positive charge in the first interfacial layer near graphite electrodes with varying surface charge density (σ). The C_2H_4 group of EC, CH_4 group of DMC, and Li^+ cations are represented as blue circles, red triangles, and purple squares, respectively, with the dotted lines in the corresponding colors illustrating the trend of the data as given by a polynomial fit. The illustration above the graph illustrates the structural transition of the interface as the electrode is charged to more negative values of σ from right to left with EC and DMC being represented as pentagons and chevrons, respectively, and Li^+ and PF_6^- as circles contained + and – signs, respectively.

3.3.2 Potential Difference across the Electrode/Electrolyte Interface

From the interfacial structures presented in Chapter 3.3.1, the variation in the potential drop (ϕ) from the metallic electrode to the bulk electrolyte may be estimated by the one dimensional solution of Poisson's equation:

$$\nabla^2\phi = -\rho/\varepsilon_0 \tag{3.3.1}$$

where ρ is the charge density and ε_0 is the vacuum permittivity; ρ is obtained by the sum of each atomic ρ_n weighted by its atomic charge, as defined by the force field parameterization and can be seen for σ = 0, -11.6, and -16.4 $\mu C/cm^2$ in Figure 3.6(a). Application of ϕ = 0 V and $\nabla\phi$ = 0 in the bulk region of the electrolyte as boundary conditions allows for simple solution yielding $\phi(z)$, which is shown for σ = 0, -11.6, and -16.4 $\mu C/cm^2$ in Figure 3.6(b). In the case of σ = 0 $\mu C/cm^2$, ϕ is found to be approximately -0.10 V; as mentioned in Chapter 3.3.1, this may be used as a reference point as ϕ_Z is known. The nonzero nature of ϕ_Z arises from the stronger vdW interactions between the electrode and solvent functionalities baring a positive charge. This has similarly been predicted by molecular simulation for 1M $LiPF_6$ in pure EC near a flat graphite edge-plane wherein the ϕ_Z was found to be approximately -0.14 V .[79]

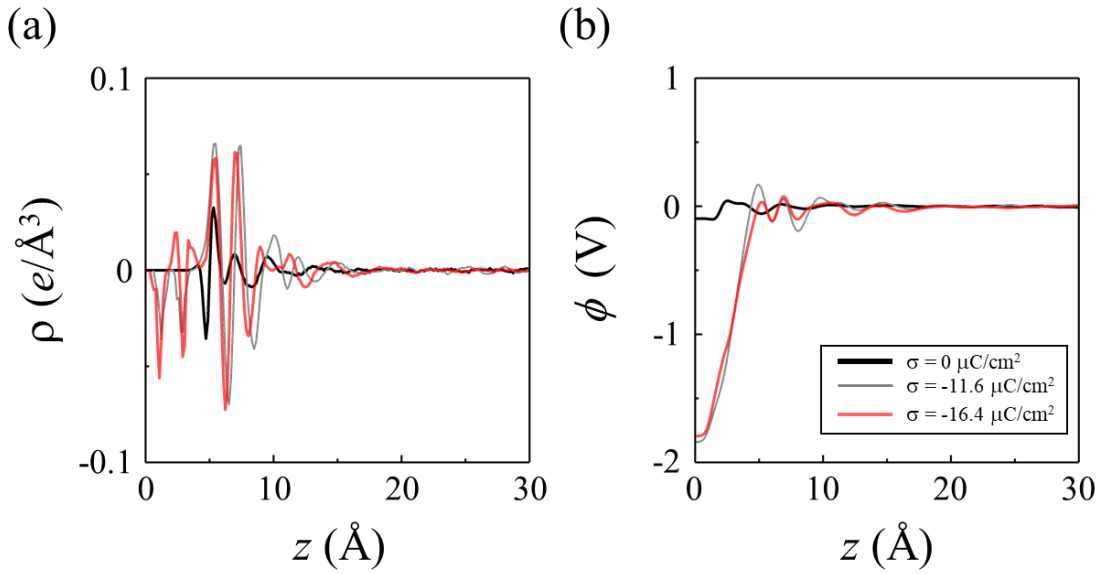

Figure 3.6. The charge density (ρ) profile along the axis perpendicular to the electrode surface (*z*) as determined by the sum of each atomic number density profile (ρ_n) weighted by the point charge assigned to the atom by the force field for electrodes with surface charge densities σ = 0, -11.6, and -16.4 μC/cm^2 (a). The Poisson potential (ϕ) as a function of *z* yielded by the solution of Equation 3.3.1 from ρ (b).

For all values of σ considered, the potential difference ($[\phi - \phi_Z]$) was predicted and is shown in Figure 3.7. As σ becomes increasingly negative, the magnitude of $[\phi - \phi_Z]$ monotonically increases until σ ≈ -12 μC/cm^2 then levels off after. The break in trend may be attributed to the precipitation of Li^+ cations onto the electrode surface, which in addition to the corrugated surface, causes the 1D description of potential to become insufficient as the ions in the same *z* plane as the edge carbons results in the cancelation of charge within ρ. However, prior to the dissolution of Li^+, the $[\phi - \phi_Z]$ appears to be nearly linear with respect to σ. Within the linear region, the differential capacitance of the electrical double layer capacitance (C_{DL}) may be calculated by:

$$C_{DL} = d\sigma/d[\phi - \phi_Z] \quad (3.3.2)$$

From this, C_{DL} is found to be approximately 6.8 μF/cm^2; for comparison, the C_{DL} was reported to be 4-5 μF/cm^2 for a similar electrolyte at a graphene basal surface[100].

The applied voltage (ϕ_a) may be approximated (with respect to the potential of the bulk electrolyte) by the sum of $[\phi - \phi_Z]$ and the electrode potential (ϕ_E):

$$\phi_a = \phi - \phi_Z + \phi_E \quad (3.3.3)$$

as was previously shown in the study of supercapacitors[93,94,101,102]. From Ref 6, ϕ_E may be considered to be approximately -0.45 V and -0.55 V for H-terminated graphene edges with $\sigma \approx$ -12 and -16 μC/cm^2, respectively. From Equation 3.3.3 and Figure 3.7, a relevant approximation of the potential of the model graphite electrodes may be obtained; for example, a $[\phi - \phi_Z]$ = -1.75 V at $\sigma \approx$ -12 μC/cm^2 corresponds to -2.2 V *vs.* the PZC of graphite (or 0.8 V *vs* Li/Li$^+$). This indicates that the regime where Li$^+$ ions exist at the graphite edges and $[\phi - \phi_Z]$ cannot be reliably approximated exists well below the reduction potential of EC-based electrolytes[4,31] of approximately 1.2 V *vs*. Li/Li$^+$ which occurs around $\sigma \approx$ -9.5 μC/cm^2. While this model allows for improvement (such as through the inclusion of polarization effects[102]), it provides a valuable benchmark for the study of the electrode/electrolyte interfacial structure prior to the reduction of solvent during the SEI formation process. Although decomposition may begin at $\sigma \approx$ -9.5 μC/cm^2, the SEI is not formed instantaneously or at a single potential as evidenced by the dependence of ramp rate on the process[103,104]. This suggests quantifying the interfacial structure over a range of potentials at which reduction occurs may provide useful insight into the formation process.

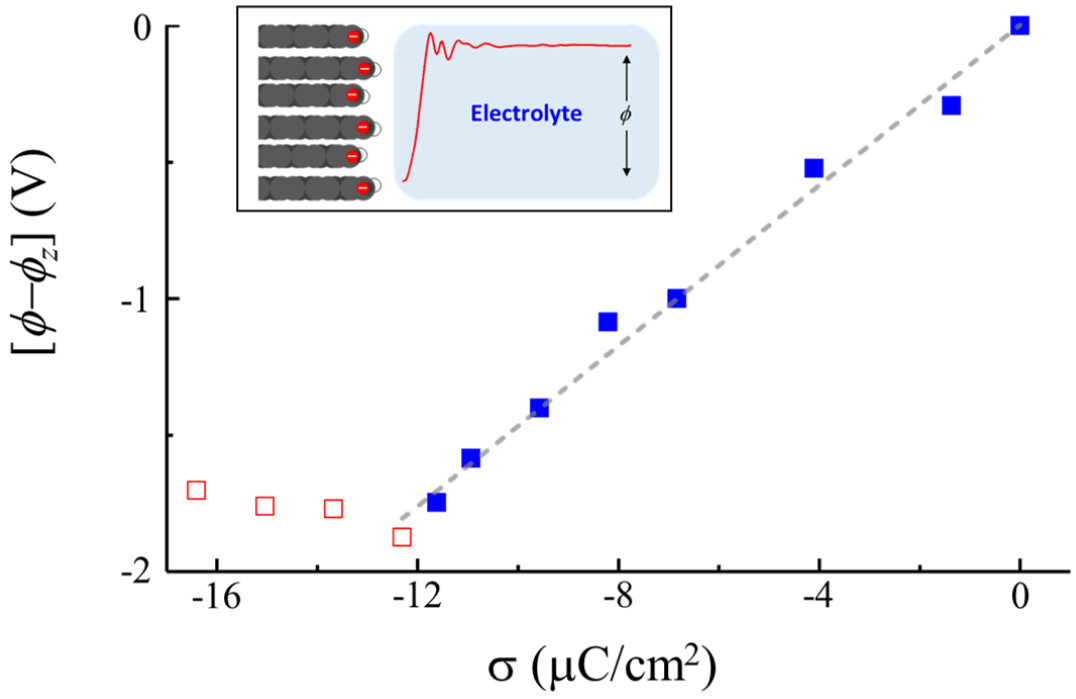

Figure 3.7. Variations in the potential difference between the electrode surface and the bulk electrolyte relative to the potential of zero charge ($[\phi - \phi_Z]$) as a function of the electrode surface charge density (σ) when no Li^+ cations are found at the interface (solid blue squares) and when Li^+ dissolution occurs (open red squares). The schematic in the inset illustrates the definition of ϕ and the dashed grey line represents a linear fit through the solid blue squares used to predict the double layer capacitance by Equation 3.3.2.

3.3.3 Evaluation of Li^+ Cation Transport near the Electrode/Electrolyte Interface

Reactions occurring at solid/liquid interfaces are not only influenced by the kinetics of the reactions themselves, but also the diffusion behavior of reactants, intermediates, and products. In bulk electrolyte, chemical species may undergo thermally activated random-walk migration; this diffusion behavior can be easily characterized by computing the mean-squared displacement or the velocity autocorrelation function. Near an interface, however, the electric field-induced rearrangement of the electrolyte would render this model

insufficient. Hence, alternative techniques must be applied to study the diffusion processes which contribute to SEI formation. Here, a free energy approach is used to evaluate the transport rate of Li^+ near the interface.

Li^+ diffusion through the interfacial layer would depend on the free energy penalties associated with its moving through intermediate states between the bulk region and the electrode/electrolyte interface. The relative free energy (ΔA) profile may be produced through the application of well-tempered metadynamics. Figure 3.8 shows ΔA as a function of the Li^+ position along the same z as in Figure 3.3 for electrodes with $\sigma = 0$ $\mu C/cm^2$ [(a)], -11.6 $\mu C/cm^2$ [(b)], and -16.4 $\mu C/cm^2$ [(c)]; the Li^+ coordination number (CN) is plotted along a second y-axis such that its solvation state may be considered.

When $\sigma = 0$ $\mu C/cm^2$ [(a)], ΔA gradually increases as Li^+ moves from the bulk-like region at $z > 25$ Å towards the electrode until it reaches a maximum around $z = 10$ Å, after which it drops into a slight minimum at $z \approx 8$ Å before a final steep increase. Along this path, the CN changes minimally between $z = 25$ Å and $z = 10$ Å indicating that the Li^+ likely remains fully solvated while diffusing in this region; the absence of oscillations suggests Li^+ is not passed over the O_C atoms of EC (and DMC) by a ratcheting mechanism, but rather maintains at least part of its solvation sheath intact as it moves. Consequently, the increase in ΔA can then be attributed to energy penalties associate with rearrangement of the molecules in the primary and secondary Li^+ solvation layers as the surrounding electrolyte becomes increasingly ordered as indicated in Figure 3.3(a). The maximum in ΔA at $z = 10$ Å can be seen to coincide with a minimum in EC/DMC ρ_n in Figure 3.3(a)

while the minimum in ΔA at z = 8 Å can be matched with a maximum in EC/DMC ρ_n. Furthermore, PF_6^- anions tend to accumulate around z = 8 Å which may also lower ΔA. The steep increase in ΔA after z = 8 Å can in great part be attribute to the inability of solvent molecules to arrange around the Li^+ cation and the lack of favorable interaction between Li^+ and the graphite electrode rendering a large energy penalty due to desolvation. It should be noted that this may be overestimated due to the non-polarizable nature of the force field used.

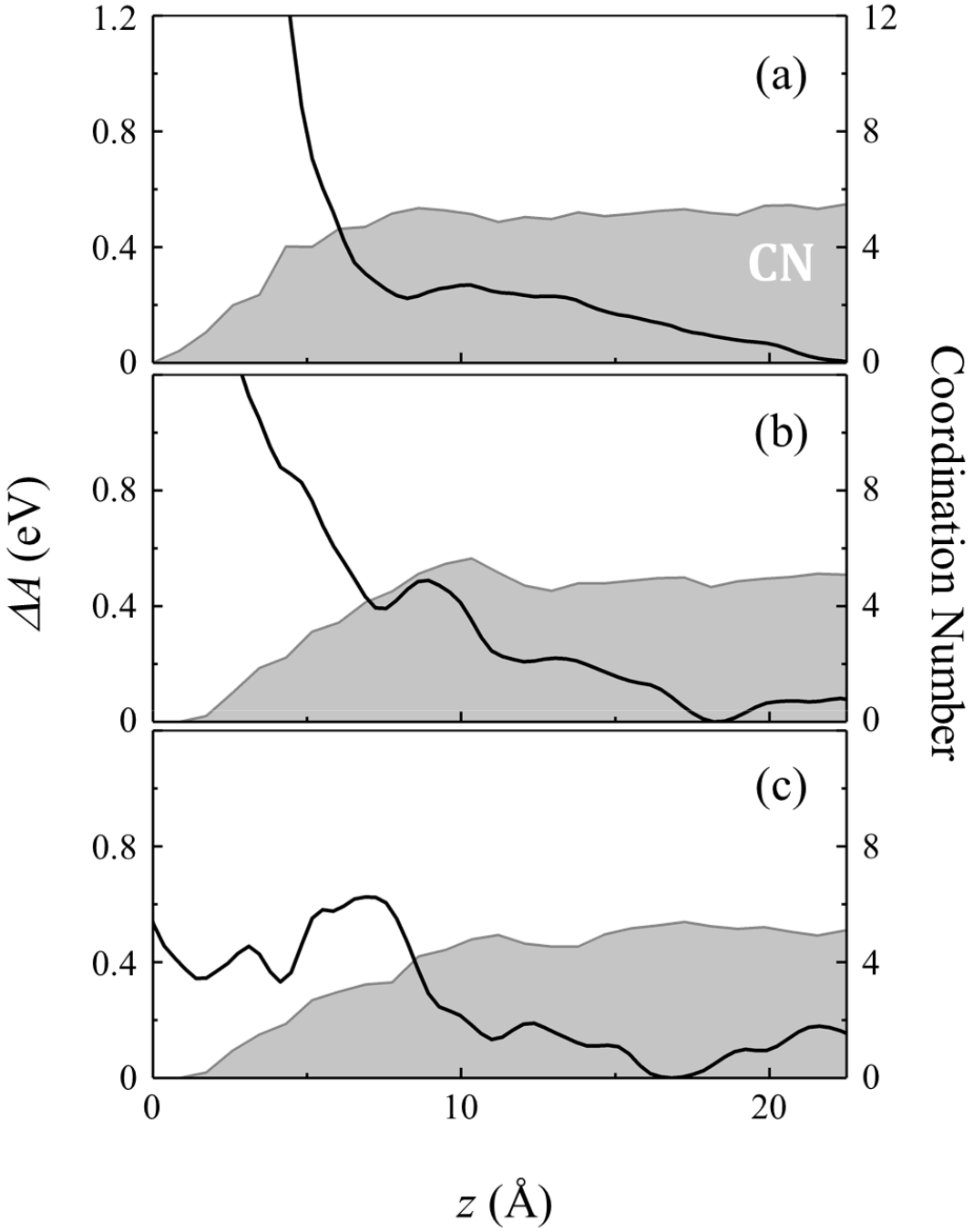

Figure 3.8. Relative Helmhotz free energy (ΔA) profiles (black) for Li^+ along the axis perpendicular to the electrode surface (z) for graphite electrodes with surface charge densities of σ = 0 (a), -11.6 (b), and -16.4 $\mu C/cm^2$ (c) and the average Li^+ coordination number by EC and DMC at that z position (grey area).

For the two charged electrode cases, the CN follows a similar pattern to [(a)] from z = 25 Å to z = 10 Å indicating that again Li^+ is able to remain fully solvate as it diffuses towards the electrode. However, the ΔA profiles do not steadily increase, but fluctuate along the z direction; this effect is more pronounced in [(c)] than [(b)]. These fluctuations may be attributed to the heterogeneity of the spatial distribution of the electrolyte components, which can be clearly seen in 2D density maps in Figure 3.9. In [(b)], a pronounced maximum can be seen at $z \approx 9$ Å; this appears to result from excess in EC/DMC/PF_6^- ρ_n from z = 8 Å to 11 Å and the accumulation of Li^+ cations. The local maximum in CN indicates within this region, Li^+ cations become overcoordinated to reduce unfavorable electrostatic repulsion between each other. Because of this, transport through the tightly pack interfacial structure would be severely hindered. For similar reasons, the ΔA profile appears to exhibit a shoulder near z = 10 Å in case [(c)]. At $z < 8$ Å, the CN of Li^+ is shown to decrease monotonically in [(b)] and [(c)]. This suggests that as the Li^+ moves within the dense solid-like layer at the interface it becomes partially solvated as the solvent molecules are unable to rearrange to maintain the fully solvation shell. Only in [(c)] is there a minimum corresponding to partially desolvated Li^+ at the electrode interface ($z <$ 5 Å) which coincides with the Li^+ ρ_n profiles in Figure 3.3; due to the electric field there is some evidence of a metastable state in [(b)] and in general the ΔA penalty is not as large as in [(a)]. However, it is difficult to separate the direct effects from the field from the effect of the field-induced reorganization of the electrolyte. Furthermore, although these

simulations do not account for the formation of an SEI, the ΔA of moving a Li^+ from the bulk to the interface in both [(b)] 85 kJ/mol and [(c)] 60 kJ/mol are consistent with previous experimental and theoretical studies,[26,48,105,106] despite different interfacial and operating conditions.

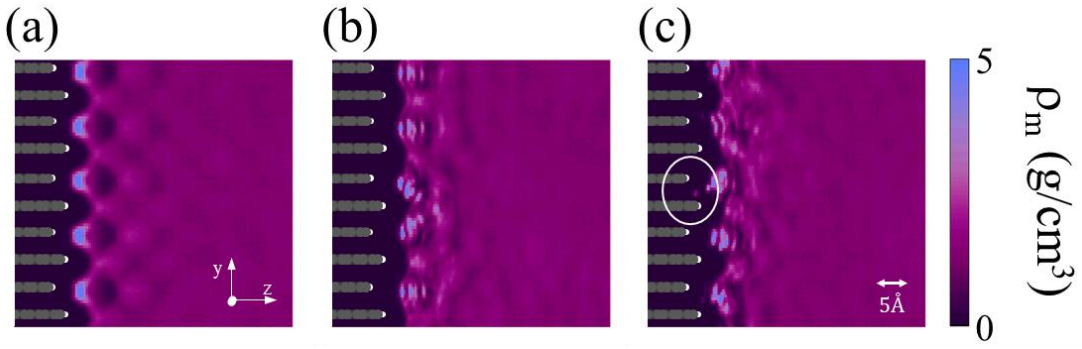

Figure 3.9. Mass density (ρ_m) maps along the directions perpendicular to the graphene basal surface (y) and perpendicular to the electrode surface (z) averaged over the remaining dimension for graphite electrodes with surface charge densities of σ = 0 (a), -11.6 (b), and -16.4 $\mu C/cm^2$ (c).

3.4 SUMMARY

The interfacial structure between a mixed carbonate electrolyte and a graphite edge surface was evaluated through classical molecular dynamics simulations over a range of electrode charge states corresponding to polarization states induced by the application of an external voltage source prior to the formation of the solid electrolyte interphase or Li intercalation. While classical molecular dynamics is unable to describe charge transfer or bond breaking, the decoupling of chemical and structural phenomena allows for detailed study of solvent and salt reorganization near an electrode surface due to an electric field. While the unoccupied orbital energies of the electrolyte molecules are critical in

determining the thermodynamic cathodic stability, however, as the interface serves as the source of electrons, the distribution of electrolyte components at the interface is critical to understanding the kinetics of reductive decomposition. While it may seem reasonable to expect that electrolyte components would distribute at the interface at the same proportions they exist in the bulk, molecular simulations show that a complex interplay between electrode-electrolyte and electrolyte-electrolyte interactions governs the interfacial structure.

For the case of a charge neutral H-terminated graphite edge surface, both EC and DMC are found to pack at the interface at higher local densities than the bulk electrolyte forming a solid-like layer extending about 20 Å from the interface. However, the first organized solvent layer contains more DMC than EC despite their parity in the bulk. This is the result of van der Waals (vdW) interactions between the H-terminated zigzag edges of the graphite and the solvent representing the dominant (and only) electrode-electrolyte interaction, which selects for DMC due to its bulkier methyl groups when compared to the ethylene group of EC. For this same reason, the salt (Li^+ and PF_6^-) is excluded from the interface entirely and is not found within the first 5 Å of the surface; due to their nonzero net charge, ions are more strongly governed by electrostatic interactions than the solvent molecules. The charge neutral case corresponds to what is known as the potential of zero charge which is a known value for graphite and is well above the reduction potential of the electrolyte.

Under simulation conditions representative of more negative applied potentials, the electrolyte components reorganize at the interface due to the increasingly electrostatic nature of the electrode-electrolyte interaction. Furthermore, the organization of the electrolyte at the interface to minimize electrostatic interaction energy at the interface results in significant charge layering which enhances the electrostatic component of electrolyte-electrolyte interactions near the interface. These effects manifest as the selective organization of EC molecules in the first solvent layer as the electrode becomes more negatively charged due to its large dipole and the accumulation of the Li^+ cations at around 10 Å from the interface due to uniform orientation of EC carbonyl O atoms away from the electrode. The interfacial structure can then be used quantify the applied potential through calculation of the potential drop across the interface by the solution of the 1D Poisson Equation; this potential drop can be added to the potential drop across the electrode estimated by density functional theory and compared to the potential of zero charge as a reference to estimate the applied potential.

The reorganization of the electrolyte due to the electric field emanating from the electrode may also effect near-interface transport phenomena. Due to the spatial heterogeneity of the interfacial structure, conventional methods for quantifying transport properties are invalid near the electrode. Instead, free energy methods such as metadynamics may be used to construct a spatial free energy profile which can indicate the probability of the target species (Li^+ cations) remaining at a given position or moving to another. By simultaneously tracking the coordination state of Li^+ during a metadynamics

simulation, the energy penalties associated with shedding a portion of its solvation shell and moving to the interface can be compared at different electrode charge states. It was shown that the electrostatic interactions between the electrode and Li^+ coupled with perturbation of the interfacial structure caused by the precipitation of Li^+ cations onto the graphite surface can significantly reduce the free energy penalty associated with moving Li^+ from the bulk to the interface.

Fundamental insights gained on the interfacial structure prior to electrochemical decomposition of the electrolyte can assist in better understanding the subsequent steps of the SEI formation process. The tendency of EC to selectively populate the first interfacial layer at applied potentials near the reduction potential of the electrolyte explains the critical role of EC as the SEI-forming component, even when used as the minority solvent. Metadynamics has been demonstrated to be a powerful tool in evaluating ion transport behavior near charged electrodes and the interplay between electrode-electrolyte and electrolyte-electrolyte interactions is crucial to understanding such transport behavior. The same computational may be applied to the study of other phenomena such as reduction intermediate and product transport during various stages of the SEI formation process.

Chapter 4 : Reductive Decomposition of Ethylene Carbonate

4.1 INTRODUCTION

The reductive decomposition of the electrolyte by the graphite anode is the central process in solid electrolyte interphase (SEI) formation and has been studied to a great extent through both theory[83,99,107–110] and experiments[19,21,38,46–48,111,112]. Despite the common practice of mixing ethylene carbonate (EC) with dimethyl carbonate (DMC),[23,75] it has been widely reported that the SEI contains primarily EC-derived species[38,46–48]. In Chapter 3, it was demonstrated that the electric field emanating from a graphite electrode polarized to negative potentials causes the reorganization of the electrolyte such that EC is the prevalent species at the interface. This may in part explain its role in SEI formation, however, a detailed mechanistic description of the process by which the SEI products are formed remains elusive. The reduction of EC by electron transfer from the negative electrode produces a radical anion species (c-EC^{-}) which may then undergo homolytic ring-opening to form o-EC^{-}.[20,42,83,108,113] This species is then further reduced to produce carbonate (CO_3^{2-}) and ethylene (C_2H_4) or, through a radical combination reaction with another o-EC^{-}, produces ethylene dicarbonate (EDC^{2-}) and C_2H_4.[20,114,115]

Work in this chapter was published in Boyer, M. J.; Hwang, G. S. Theoretical Prediction of the Strong Solvent Effect on Reduced Ethylene Carbonate Ring-Opening and Its Impact on Solid Electrolyte Interphase Evolution. *J. Phys. Chem. C.* **2019**, *123* (29), 17695–17702. G.S.H. contributed in part to the planning of the study and writing of the manuscript.

Previous theoretical studies utilizing a variety of density functional theory (DFT) and DFT-based methods have predicted significant ring-opening barriers for c-EC^- and that it would persist for times on the order of ms.[107–109] Simulations where two electrons are consecutively added to simulation boxes containing liquid EC with and without Li^+ have shown that if the second electron is added prior to c-EC^- ring-opening, the second electron will localize on c-EC^- and ultimately lead to the production of CO and a glycoxide dianion species[99,116] which was then later predicted to be the predominant EC reduction pathway based on analysis of reaction rates[83]. While glycoxide may react with CO_2 to form EDC^{2-}, the direct combination reaction of two o-EC^- can better directly explain the observation of alkyl carbonates of the predominant SEI component as previously reported[37,117–120]. Furthermore, minimal CO evolution is observed when compared to C_2H_4 which has been proposed originate from the 2-electron reduction of DMC.[121] The competing reaction pathways are summarized in Figure 4.1.

In this chapter, the reductive decomposition of EC is evaluated through DFT simulations. The reduction of EC and DMC are compared and the effect of Li^+ cations is examined to determine their relative thermodynamic stability near polarized graphite electrodes. The energetics of the c-EC^- ring-opening reaction is discussed in detail and the energetics are compared between a range of implicit and explicit solvents. More detailed analysis on the effect of intermolecular interactions in explicit solvent is provided to illustrate the significance of such interactions.

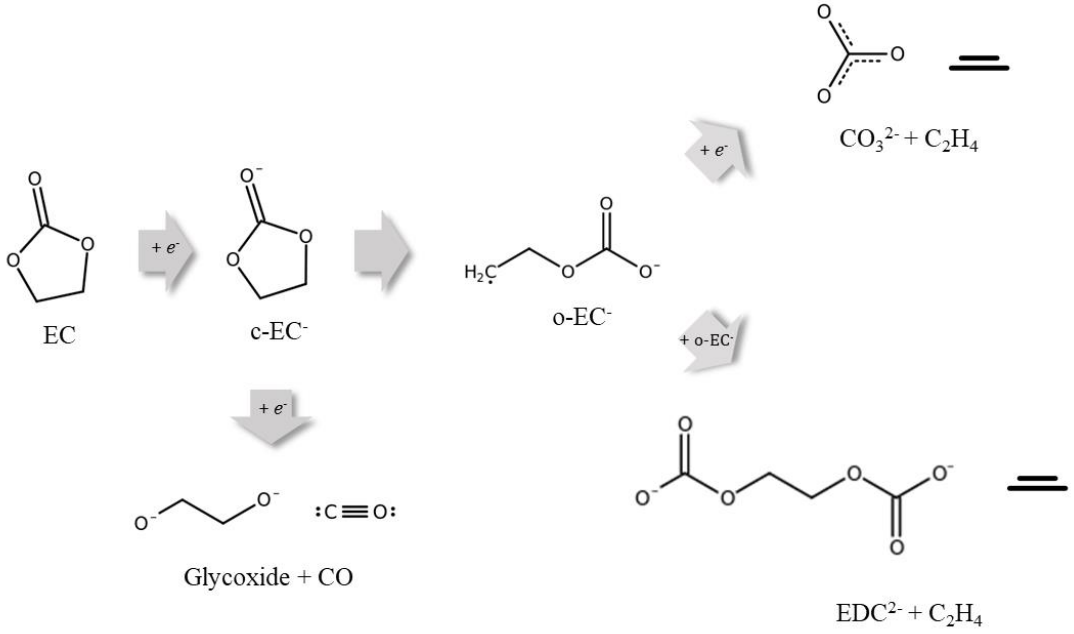

Figure 4.1. Schematic of possible reductive decomposition pathways for EC where an empty arrow indicates a thermal decomposition reaction and arrows containing a + symbol indicate the addition of either an electron or a bimolecular reaction, depending on the species within the arrow.

4.2 METHODOLOGY

Static quantum mechanical calculations were performed using hybrid Becke 3-Lee–Yang–Parr (B3LYP)[122,123] and Perdew, Berke, and Ernzerhof (PBE)[124] exchange-correlation functionals and the 6-311++g(d,p) basis set within the Gaussian 16 suite of programs[125]. Ground and transition states found through geometric optimization were verified through vibrational frequency analysis and zero point energy (ZPE) corrections were made. Solvent interactions were represented by the polarizable continuum model (PCM)[126] and partial atomic charges were predicted based upon the restrained electrostatic potential (RESP) fitting method[127].

Ab initio molecular dynamics simulations were performed based on DFT using the PBE exchange-correlation functional within the Car-Parrinello framework[128] as implemented in the CPMD (ver 3.15.1) simulation package[129]. Orthorhombic simulation boxes with side lengths of 11.3 and 12.1 Å were filled with 12 EC and 7 EC /7 DMC molecules, respectively. The simulation cell was briefly annealed at 700K using a classical force field before a Li^+ cation was added and a neighboring EC molecule was alchemically converted to EC^- by reassigning the force field parameters. The system was again annealed for 750 ps and then quenched to 300K for another 750 ps. The output configurations from this preprocess were then relaxed by CPMD for 20 ps at 300K. During time integration, a timestep of 0.17 fs was used; to enable use of a large timestep while maintaining adiabaticity, the Deuterium mass was used for H in conjunction with a fictitious electron mass of 700 m_e, where m_e is the electron rest mass. A Nosé-Hoover thermostat was utilized to maintain the target simulation temperature of 300K. A planewave basis set cutoff of 340 eV was used and interactions between valence and core electrons were described using Goedecker[130] and Martins-Troullier[131] pseudopotentials for Li and H/C/O atoms, respectively. Due to the need to describe unpaired spins in radicals such as EC^-, the local spin density (LSD) approximation was applied in all simulations.

Production runs were carried out for an additional 20 ps to generate structural data without the application of constraints. Metadynamics simulations were performed in excess of 135 ps to construct free energy profiles; the algorithm was used as implemented

within the Plumed plugin[132]. Gaussian hills with fixed height were deposited every 200 timesteps during the simulation; each hill had a height of 0.0435 eV and a width of 0.13 Å.

4.3 Results and Discussion

While experimental studies have identified EC as the predominant SEI-forming component of the LIB electrolyte,[38,46–48] the size- and time-scales at which the processes which contribute to SEI formation occur have hindered advancement of their description. In order to bridge the gap in understanding between factors which may be controlled such as electrolyte composition, temperature during SEI formation, cutoff voltage, and voltage ramp rate on the resulting SEI structure and properties, a detailed understanding of all relevant reactions and intermediates is required. The following sections describe the evaluation of the EC reduction reaction and the subsequent ring-opening reaction through DFT simulations with implicit and explicit solvent.

4.3.1 Selective EC Reduction

Prior to the initial insertion of Li^+ into the graphite electrode, the Fermi level is raised by an external voltage source above the lowest unoccupied molecular orbital (LUMO) energy of the solvent molecules in the electrolyte. Beyond this potential, it is thermodynamically favorable for electrons to flow from the graphite into the unoccupied orbitals of the solvent molecules thereby reducing them and ultimately resulting in the formation of the SEI for EC-based electrolytes. Because of this, LUMO energies may be used to evaluate the relative reductive stability of molecules or clusters of molecules.

In EC/DMC mixed solvent electrolytes, the relative LUMO levels may provide insight to which solvent species can be reduced first as the potential is shifted to more negative values. An additional factor which must be considered is the addition of salt (Li^+/PF_6^-) into the solvent which may add a further layer of complexity due to strong electrostatic interactions between carbonate solvents and Li^+; extensive study of the Li^+ solvation structure in carbonate mixtures has shown it to favor tetrahedral coordination by the carbonyl oxygen (O_C) atoms[107,133,134].

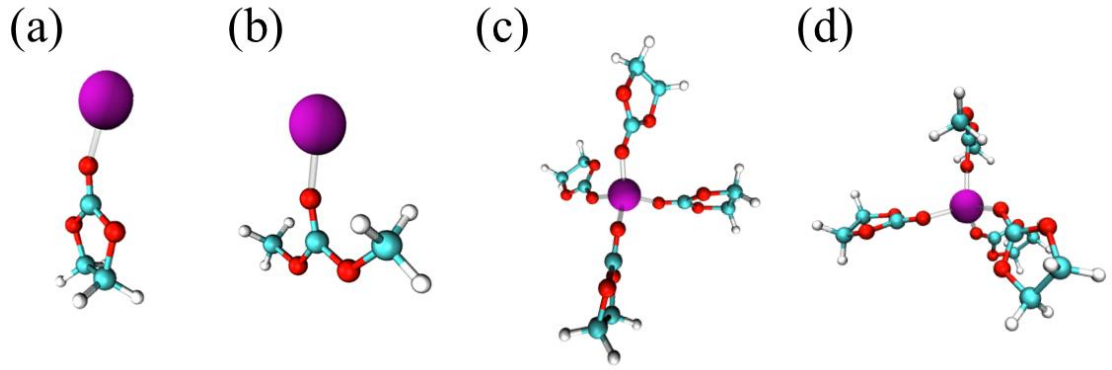

Figure 4.2. Optimized structures of $(ECLi)^+$, $(DMCLi)^+$, $(EC_4Li)^+$, and $(EC_3DMCLi)^+$ clusters (a-d), respectively, considered in calculation of lowest unoccupied molecular orbital (LUMO) energies and free energies of reduction.

LUMO energies for isolated and Li^+-solvating EC and DMC molecules were predicted by quantum mechanical calculations using the polarizable continuum model (PCM-DFT) as described in Section 4.2.1. Clusters with compositions of $(ECLi)^+$, $(DMCLi)^+$, $(EC_4Li)^+$, and $(EC_3DMCLi)^+$ and are shown in Figure 4.2. Shifts in predicted LUMO energy relative to EC for DMC and the clusters are shown in Table 4.1 in addition to the predicted atomic charges of Li. The LUMO orbitals of isolated EC and $(ECLi)^+$ are

shown in Figure 4.3 where it can be seen that the orbital shapes are considerably different with and without the inclusion of Li^+; the lowering in the LUMO energy for $(ECLi)^+$ appears to be the result in polarization which may be visualized by the charge density difference plot shown in Figure 4.3(c). The degree of polarization may be predicted by the projection of electron density onto atomic nuclei to derive partial atomic charges using the RESP method. This approach predict that the Li atom bares a partial charge of +0.98 demonstrating that its 2*s* orbital is almost fully depopulated. A similar effect is observed for both the $(EC_4Li)^+$ and $(EC_3DMCLi)^+$ where one of the lone pairs on each O_C atom interacts with an empty sp^3 orbital on Li^+; the donation of electron density from the lone pairs results in Li baring atomic charges of +0.83 and +0.90 in $(EC_4Li)^+$ and $(EC_3DMCLi)^+$, respectively. Here, the LUMO energy is lowered slightly more than the $(ECLi)^+$. It should also be noted that for $(EC_3DMCLi)^+$ the LUMO is primarily localized on the EC molecules, which is consistent with the side-by-side comparison of $(ECLi)^+$ to $(DMCLi)^+$ wherein EC has a lower LUMO level in the presence of Li^+.

	EC	**DMC**	**$(ECLi)^+$**	**$(DMCLi)^+$**	**$(EC_4Li)^+$**	**$(EC_3DMCLi)^+$**
ΔE_{LUMO} (eV)	0	+0.01	-0.37	-0.33	-0.50	-0.49
Li charge	--	--	+0.98	+0.97	+0.83	+0.90

Table 4.1**.** Relative lowest unoccupied molecular orbital (LUMO) energies (ΔE_{LUMO}) with respect to EC obtained from PCM-DFT and Li atomic charges as predicted by the RESP method. The model clusters containing EC, DMC, and Li^+ are shown in Figure 4.2.

Although LUMO level is a convenient approach to evaluating reduction reactions, the stabilization of a charged molecule through structural rearrangement would also contribute to reduction potential. The potential at which an electrochemical reaction may begin to occur (E_{rxn}) is related to the Gibbs free energy of reaction (ΔG_{rxn}) by the equation:

$$\Delta G_{rxn} = -nFE_{rxn} \tag{4.3.1}$$

where F is the Faraday constant and n is the number of charge carrying particles transferred per reaction. The Gibbs free energy of a reduction reaction (ΔG_{red}) for a species M relative to an electron at rest in vacuum is given by the equation:

$$\Delta G_{red} = -[G_g(M^-) - G_g(M) + \Delta G_{solv}(M^-) - \Delta G_{solv}(M)] \tag{4.3.2}$$

where $G_g(M)$ and $G_g(M^-)$ are the gas-phase free energies of the neutral and reduced species, respectively, and ΔG_{solv} refers to the free energy difference of solvation. The combination of Equations 4.3.1 and 4.3.2 yield the absolute reduction potential relative to an electron at rest in vacuum. However, for relative comparisons between species, the reference potential is unimportant and therefore reduction potentials shifts (ΔE_{Red}) relative to EC are reported in Table 4.2. Following the trend of the LUMO energies, the addition of Li^+ shifts the reduction potential of EC to more positive values (meaning it would be reduced sooner) for $(ECLi)^+$, $(EC_4Li)^+$, and $(EC_3DMCLi)^+$ with the shift being larger in the case of $(ECLi)^+$ which is less constrained to rearrange. However, $(DMCLi)^+$ exhibits a shift in ΔE_{Red} to more negative potential than DMC. Relaxation of the reduced form of the $(EC_3DMCLi)^+$ cluster results in the buckling of the carbonate group of a single EC

molecule as with an isolated EC molecule which further evidences the selectivity towards EC reduction.

	EC	**DMC**	**$(ECLi)^+$**	**$(DMCLi)^+$**	**$(EC_4Li)^+$**	**$(EC_3DMCLi)^+$**
ΔE_{Red} (V)	0	-0.06	+0.62	-0.43	+0.37	+0.32

Table 4.2**.** Reduction potentials shifts (ΔE_{Red}) relative to EC for clusters shown in Figure 4.2 as predicted by PCM-DFT.

The results highlighted in this section indicate that in addition to the kinetic contributions to selective EC reduction, polarization due to Li^+ ions may also contribute to thermodynamic selectivity towards the reduction of EC before DMC. Furthermore, the observed favorability of the reduction EC molecules solvating Li^+ over those which remain free in solution indicates that Li^+ should be considered in the simulation of all subsequent decomposition reactions as it was for the remainder of the results presented in this chapter. However, the nonequilibrium nature of SEI formation could allow for reductive decomposition of DMC either at a slower rate or at more negative potentials upon consumption of EC at the interface (assuming it is not replaced through diffusion). Furthermore, the dependence of the reduction thermodynamics on the interaction with Li^+ cations suggests that high throughput screening studies[135–137] should consider such interactions when trying to evaluate potential additives based on reduction potential; the polarization effect of Li^+ on reduction potential in addition to the field-induced reorganization of solvent at the electrode/electrolyte interface may suggest that such

screening studies cannot adequately account for relevant factors to describe electrochemical decomposition in LIBs.

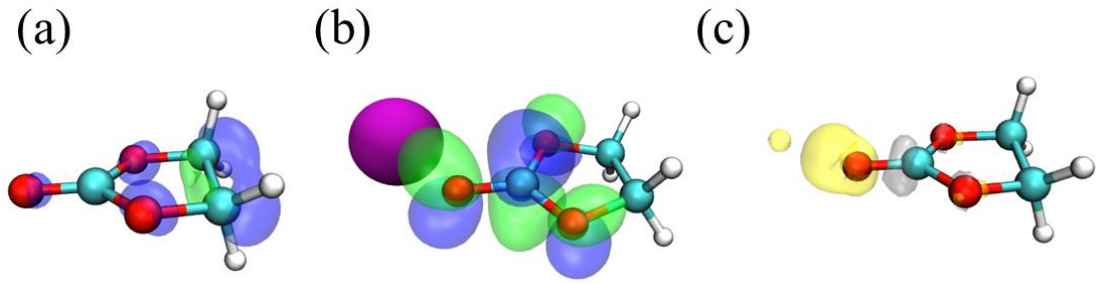

Figure 4.3. The isosurface of the lowest unoccupied molecular orbital (LUMO) for isolated EC (a) and $(ECLi)^+$ (b) where blue and green correspond to positive and negative isodensities, respectively. The charge density difference plot between EC and $(ECLi)^+$ (c) where yellow indicates more negative charge in $(ECLi)^+$ and silver indicates more negative charge in EC.

4.3.2 Reduced EC Ring-Opening Reaction

Upon the reduction of EC to produce c-EC^-, it may thermally decompose by homolytic ring-opening to produce o-EC^- by scission of the bond between the ether oxygen (O_E) and ethylene carbon (C_E) atoms as shown in Figure 4.4. The barrier for this reaction, as predicted by DFT calculations in implicit solvent, has been reported to be between 0.3-0.6 eV, depending on the selected exchange-correlation functional and basis set. As previous work did not place a large emphasis on the effect of solvent, free energy barriers ($\Delta G^{\ddagger}$) and the reaction energies (ΔG) for the ring-opening of c-EC^- were calculated through DFT calculations with particular attention to the exchange-correlation functional and implicit solvent dielectric constant (ε). The optimized structures of c-EC^-, o-EC^-, and the transition state are shown in Figure 4.4 and the results of these calculations are summarized

in Table 4.3 for c-EC$^-$ bound to Li$^+$. For an implicit solvent with ε = 21 (similar to a 50/50 mixture of EC/DMC), ΔG and $\Delta G^{\ddagger}$ are found to be 0.41 eV and -1.34 eV, respectively, for the B3LYP exchange-correlation functional, while they were predicted to be only 0.25 eV and -1.22 eV, respectively, when for PBE. While both $\Delta G^{\ddagger}$ and ΔG are very sensitive to the exchange-correlation functional, neither are shown to be sensitive to the choice of implicit solvent whatsoever.

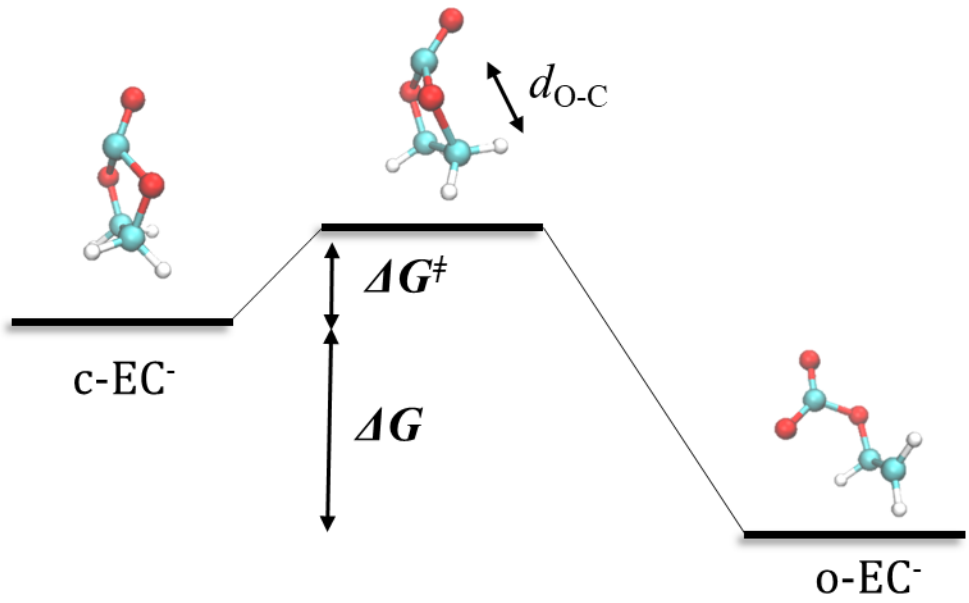

Figure 4.4. Optimized structures of c-EC$^-$, o-EC$^-$, and the transition state obtained by DFT-PCM calculations as well as schematic diagram of the reaction coordinate used to obtain the free energy barriers ($\Delta G^{\ddagger}$) and the reaction energies (ΔG).

In contrast with the significant barriers predicted by static quantum chemical calculations, prior studies conducted using *ab initio* molecular dynamics (AIMD) simulations with PBE demonstrated anomalously fast c-EC$^-$ ring-opening in explicit EC[99]; this phenomenon may in part be explained by the intermolecular interactions between c-

EC^- and the solvent and/or by insufficient description of self-interaction of electrons by PBE. To examine the effect of explicit solvent molecules on this reaction detail, simulations were conducted within the Car-Parrinello MD (CPMD) framework and the c-EC^-→o-EC^- reaction pathway was sampled through the use of the metadynamics algorithm. Simulation boxes with side length of 11.3 (12.1) Å containing Li^+/ EC^- pair and 12 EC (or 7 EC and 7 DMC) molecules were used to represent the reaction in pure EC (50/50 EC/DMC). The distance between O_E and C_E ($d_{O\text{-}C}$), shown in Figure 4.4, was used as the collective variable (CV) used within the metadynamics simulations and the resulting Helmhotz free energy (ΔA) profiles along the CV are shown in Figure 4.5.

	Water	**Dimethyl Sulfoxide**	**Acetonitrile**	**Acetone**	**2-Pentanone**	**2-Heptanone**
ε	80	47	37	21	15	12
B3LYP $\Delta G^{\ddagger}$ (eV)	0.42	0.41	0.41	0.41	0.41	0.42
B3LYP ΔG (eV)	-1.32	-1.32	-1.33	-1.34	-1.34	-1.35
PBE $\Delta G^{\ddagger}$ (eV)	0.24	0.24	0.24	0.25	0.26	0.26
PBE ΔG (eV)	-1.19	-1.19	-1.19	-1.22	-1.20	-1.25

Table 4.3. Reaction barriers ($\Delta G^{\ddagger}$) and energies (ΔG) predicted by PCM-DFT simulations using B3LYP and PBE exchange-correlation functionals and a variety of implicit solvents with dielectric constants (ε).

In both pure EC and EC/DMC, ΔA exhibits a distinct minimum at $d_{O\text{-}C} \approx 1.45$ Å which corresponds to the ring-like c-EC^- configuration. The second minimum is extremely broad, relative to the first, spanning from $d_{O\text{-}C} \approx 2.5$ to 4.3 Å; this corresponds to the flexible

chain-like o-EC^- which has many stable configurations separated by only a few meV in the explicit solvent systems. The two states are separated by a maximum at $d_{O\text{-}C} \approx 1.7$ Å which corresponds to the transition state. However, the c-EC^- minimum is notably deeper in pure EC than in EC/DMC, while the plateau associated with o-EC^- is deeper but less broad in EC/DMC than pure EC. This suggests that c-EC^- is relatively less stable in EC/DMC and perhaps that o-EC^- is more stable.

In comparison to static quantum mechanical calculations, the free energy barrier ($\Delta A^{\ddagger}$) for ring-opening is smaller in both pure EC (0.23 eV) and EC/DMC (0.09 eV), though far more so in the latter. While $\Delta A^{\ddagger}$ is of primary importance in evaluation of the reaction kinetics, the difference in ΔA between c-EC^- and o-EC^- in the two solvent systems (1.5 eV in EC/DMC and 0.6 eV in pure EC) may provide some explanation as to the origin of the solvent effect due to the opposite trend behavior. This suggests that ring-like c-EC^- is relatively more favorable in the pure EC which contains only ring-like molecules, while the o-EC^- is relatively more favorable in EC/DMC which contains both ring-like and acyclic molecules. While it is known that EC is more viscous in nature than EC/DMC mixtures[74,75] which could result in sluggish reorganization of surrounding solvent molecules in pure EC, this behavior may also in part result from solubility differences due to geometric compatibility.

It is important to note that constraints imposed by intermolecular reactions between the reactive species and the surrounding molecules, and therefore configurational entropy are not accounted for in static quantum mechanical calculations utilizing implicit solvents;

in addition to free energy changes due to bond scission, these interactions could also significantly alter the free energy difference between states. If indeed the pure EC system can better accommodate c-EC^- through the formation of some sort of ring-stacking structure like that which causes EC to solidify at room-temperature[73], then perhaps the addition of DMC to the system may perturb this order and reduce the stability of c-EC^-. This same perturbation of order may also result in enhanced stability of the o-EC^- which can be readily solvated by the more flexible environment.

While it is widely known that the addition of DMC to EC is important for promoting ionic conductivity[138] and preventing solidification of EC at room temperature[73], this result suggests DMC may also help facilitate thermal reactions involved in the formation of the SEI through lowering of viscosity and/or disrupting the order of the local structure. It is also possible that other factors such as structural changes due to interfaces or anions may also contribute to reducing the stability of c-EC^- assisting in the formation o-EC^-. While previous calculations have predicted long c-EC^- lifetimes, this section has shown that they may be more short lived when accounting for a more realistic depiction of the lithium ion battery environment.

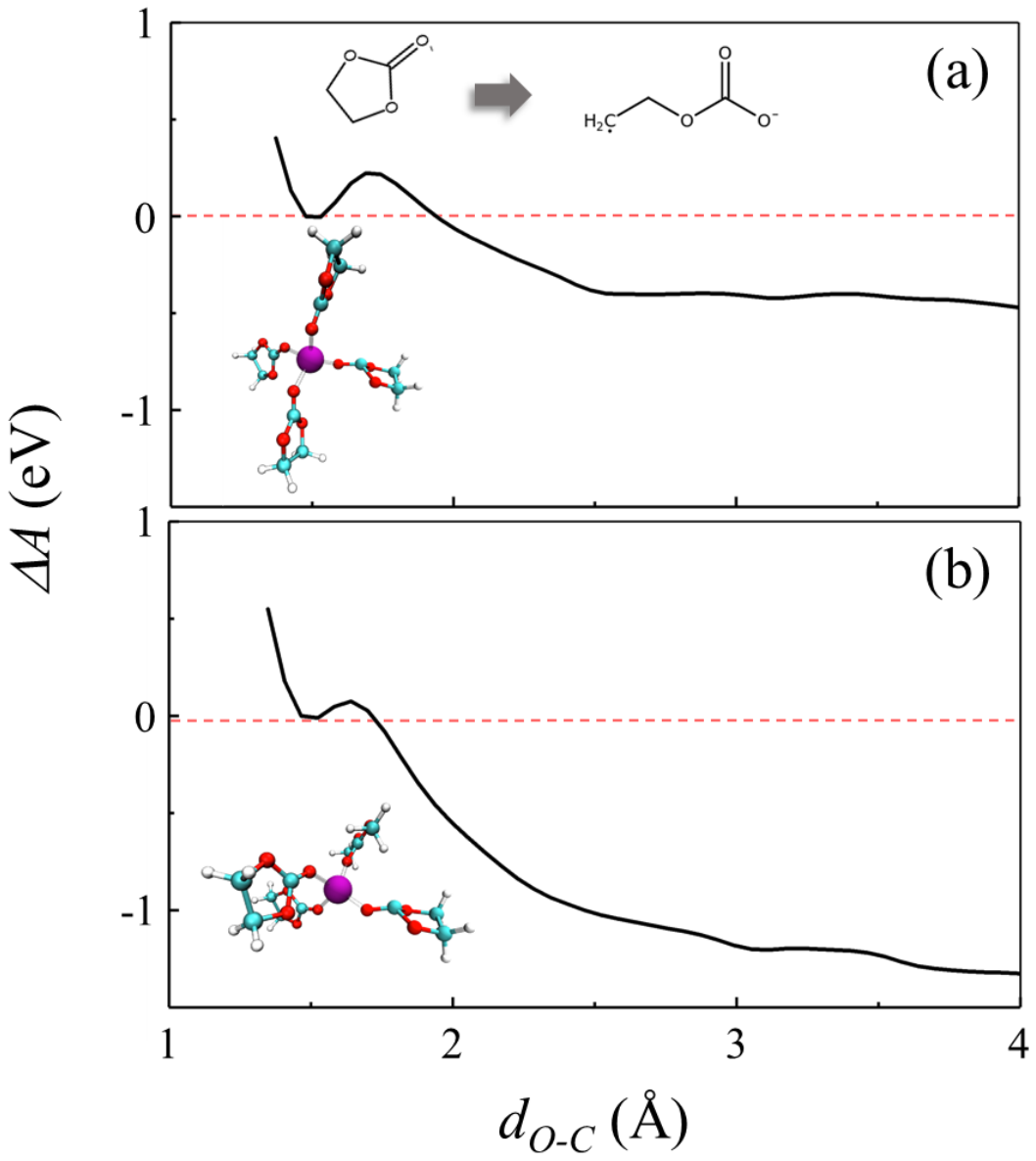

Figure 4.5. Relative Helmhotz free energy (ΔA) profiles along the distance between the ether O and ethylene C atoms ($d_{O\text{-}C}$) which undergo bond scission during c-EC$^-$ ring-opening in pure EC (a) and 50/50 EC/DMC (b). The dotted red lines correspond to the ΔA of the c-EC$^-$ state which is used as the reference and a schematic of the reaction is shown in the inset to indicate ring-opening occurs from left to right along $d_{O\text{-}C}$.

4.3.3 Origin of the Strong Solvent Effect

To further elucidate the origin of the observed solvent effect on $\Delta A^{\ddagger}$ when considering explicit EC and DMC molecules, a detailed structural analysis on the rearrangement of c-EC^- around the Li^+ cation during ring-opening was performed. Figure 4.6 illustrates the interactions between O_C and O_E with Li^+ through the probability density functions (PDFs) of the O_C-Li^+ and O_E-Li^+ pair distances during unconstrained and metadynamics simulation trajectories; note only frames where EC^- exists as c-EC^- or the transition state are included. The PDFs for pure EC [(a)] and EC/DMC [(b)] extracted from metadynamics highlight the rearrangement during the ring-opening reaction, while the unconstrained simulations only sample the thermal fluctuations on the equilibrium structure.

A clear maximum around r = 2.16 Å can be seen in the O_C-Li^+ PDF of pure EC during both unconstrained and metadynamics simulations; this is representative of the solvation of Li^+ by O_C as commonly observed for carbonate solvents as discussed in section 4.3.1. The O_E-Li^+ PDF during metadynamics, however, shows clear deviation from the unconstrained simulation; the distinct peak at r = 3.5 Å in the latter becomes a plateau-like distribution from r = 2 Å to 4.5 Å. From this result, it can be observed that while only O_C participates in Li^+ solvation during the unconstrained simulation and the structure remains fairly ordered, during metadynamics the structure becomes far more fluid as the O_E-Li^+ pair distance spans the interaction range of both direct Li^+ solvation and exclusion from the primary solvation shell.

Contrarily in EC/DMC, the peaks for both O_C-Li^+ and O_E-Li^+ are aligned between the unconstrained and metadynamics simulations with the former centered at r = 2.06 Å and the latter at r = 2.15 Å; the notable difference between the two is the presence of longer tails on the distributions for the metadynamics simulations spanning from r = 2.5 Å to r = 3.5 Å for O_C and from r = 2.5 Å to r = 4.5 Å for O_E. The shift in the O_E of the unconstrained simulation relative to pure EC is the result of its participation in the primary solvation shell of Li^+ as can be seen in the inset of Figure 4.6. Furthermore, the observed broadening of both peaks relative to pure EC suggests the structure is less rigid which may facilitate rearrangement of c-EC^- allowing for the participation of the O_E atom in the solvation shell of Li^+; fluid reorganization of the surrounding molecules may reduce the energy penalties associated with unfavorable interactions which occur during ring-opening, thus reducing the reaction barrier.

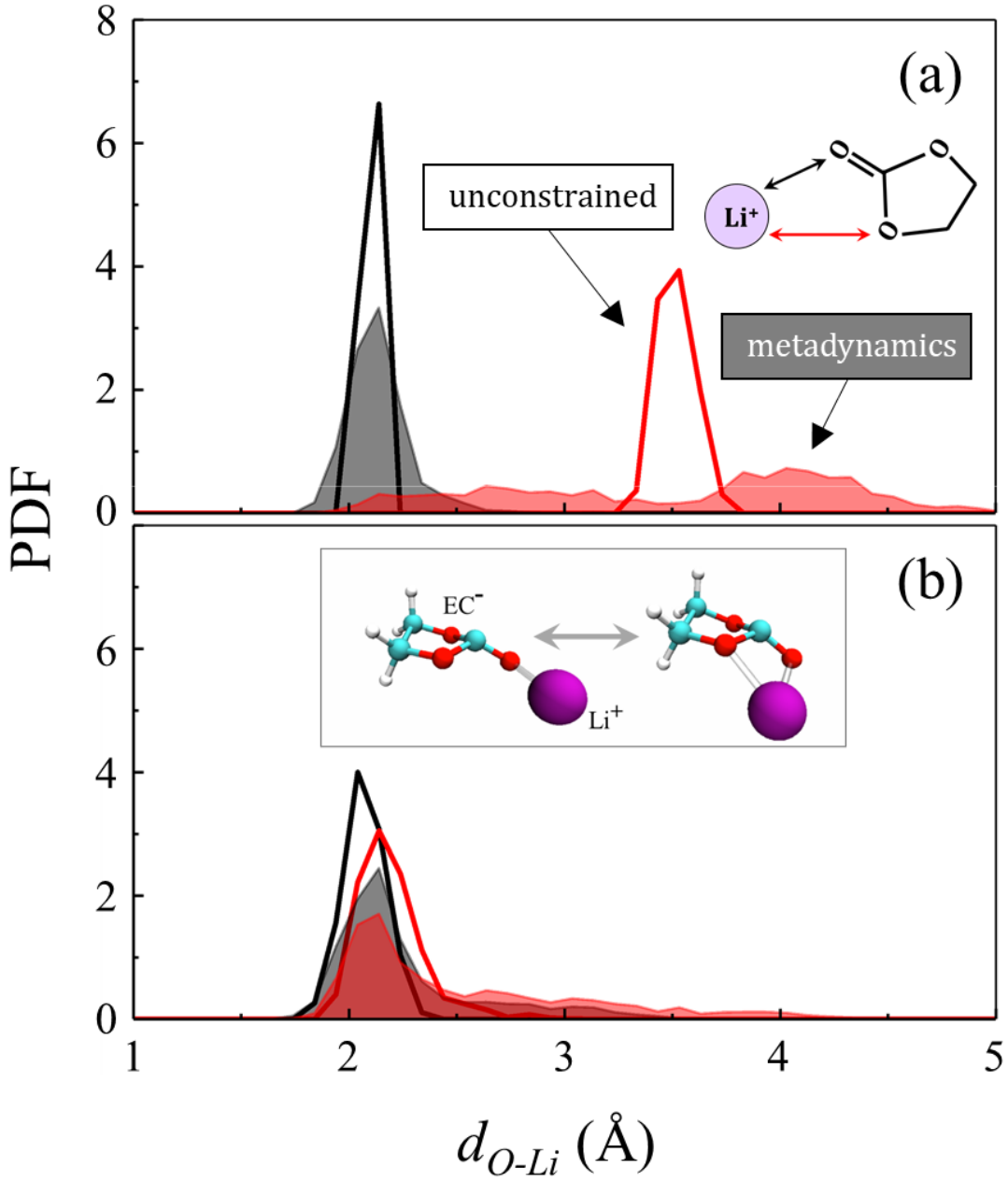

Figure 4.6. Probability density functions (PDFs) of the O-Li^+ pair distances for the carbonyl O (black) and ether O (red) of c-EC^- extracted from unconstrained (line) and metadynamics (area) simulations for c-EC^- in pure EC (a) and 50/50 EC/DMC (b). Snapshots of the two different Li^+ solvation configurations are shown in the inset of (b).

A more detailed investigation of configurations along the reaction coordinate during metadynamics simulations (shown in Figure 4.7) further explains the solvent effect on $\Delta A^{\ddagger}$. While EC^- is in the c-EC^- configuration ($d_{O\text{-}C} \approx 1.45$ Å) the O_E-Li^+ distance is about 3.16 Å, but begins to decrease to 2.62 Å as the O_E-C_E bond elongates and the transition state is approached ($d_{O\text{-}C} \approx 1.69$ Å). A similar effect is also observed in EC/DMC, where the O_E-Li^+ distance is reduced, yet not by as much (0.07 Å) as the O_E-C_E bond elongates to the transition state configuration ($d_{O\text{-}C} \approx 1.64$ Å). In both cases, c-EC^- reorientation about Li^+ is observed as the transition state is traversed, yet this occurs to a far greater degree in pure EC when compared to EC/DMC. The more significant structural changes coupled with the more viscous environment results a more severe energy penalty which consequently increases $\Delta A^{\ddagger}$.

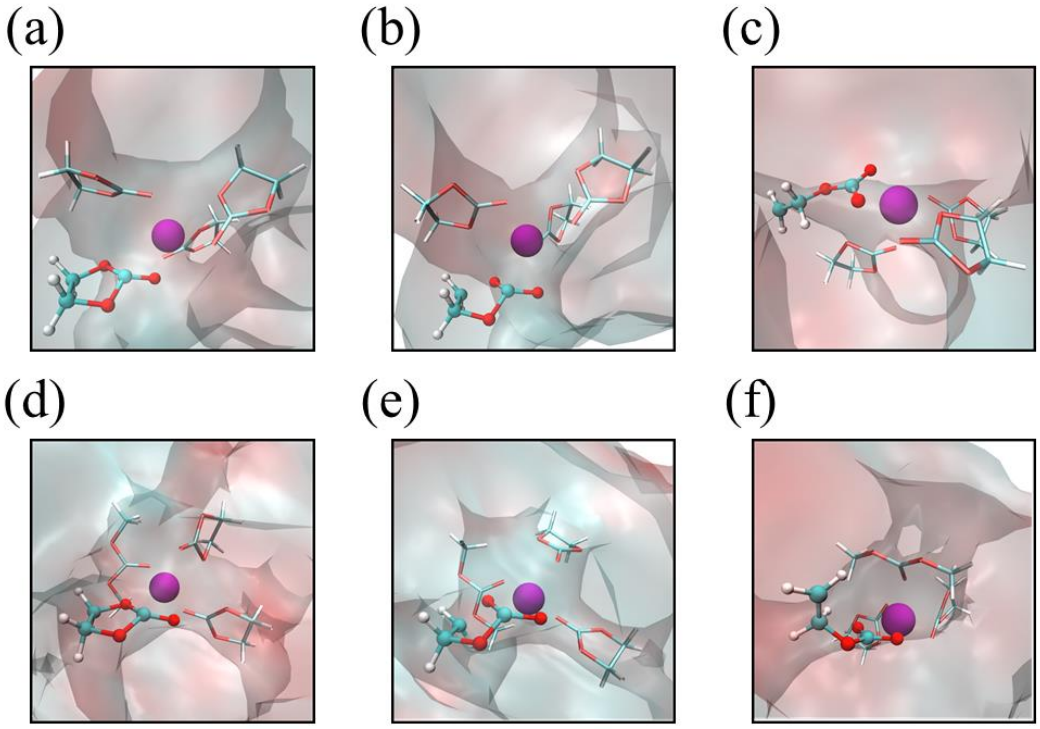

Figure 4.7. Snapshots taken from the metadynamics trajectory of the c-EC^- configuration (a), transition state (b), and o-EC^- configuration (c) in pure EC. The corresponding states are shown in the same order in EC/DMC (d-f).

From this analysis it is apparent that the intermolecular interactions involving molecules within the first and possibly even the second Li^+ solvation shell impact the ring-opening of c-EC^- bound to the cation. While implicit solvent models may be sufficient to describe less complex reactions and/or environments, the intricate chemistry involved in the SEI formation process and the heterogeneous nature of mixed carbonate electrolytes requires more complicated models to adequately capture the salient phenomena. Furthermore, this result highlights the importance of DMC beyond improving the bulk properties of the electrolyte.

4.4 SUMMARY

The reductive decomposition of mixed carbonate electrolytes was studied using density functional theory. The reductive stability of EC and DMC were compared in the presence and absence of Li^+ cations by lowest unoccupied molecular orbital (LUMO) energies and by theoretical reduction potentials derived from reduction free energies both predicted with implicit solvent represented by the polarizable continuum model (PCM). EC molecules which are solvating Li^+ cations were found to be reduced at more positive potentials than those which are surrounded by solvent due to polarization effects. Furthermore, DMC was found to be more reductively stable than EC; while LUMO energies showed only a slight difference, the inclusion of stabilization of the excess electron through structural reorganization widens the gap between the two solvents as EC is better able to accommodate the charge through rearrangement.

Upon reduction, c-EC^- may undergo homolytic ring-opening to form o-EC^-. The reaction energetics were evaluated for c-EC^- solvating a Li^+ cation using pure DFT exchange-correlation and hybrid functionals within the PCM model of implicit solvent. While the addition of exact exchange-correlation energy by the hybrid functional considerably alters the ring-opening barrier and reaction energy, the choice of implicit solvent shows no appreciable effect on either. The barriers predicted by hybrid (0.41 eV) and GGA (0.25 eV) functionals both suggest that c-EC^- would persist for relatively long times: on the scale of ns to ms.

While the PCM model may be sufficient to describe less complex systems, the inclusion of Li^+ with and without its full solvation shell considerably alters the reduction potential of EC due to polarization effects. Similarly, intermolecular interactions should be expected to affect the ring-opening reaction. To observe this, *ab initio* molecular dynamics simulations were performed in the Car-Parrinello framework to study the ring-opening reaction in a fully explicit solvent environment. Pure EC and 50/50 EC/DMC were used as model systems are free energy profiles for the ring-opening reaction were constructed using metadynamics. Using the same GGA functional as in the PCM calculations, both the reaction energy and barrier were shown to change significantly between the two solvent systems: in pure EC the barrier and reaction energy were about 0.23 and 0.6 eV while in EC/DMC they were predicted to be 0.09 and 1.5 eV, respectively.

A detailed analysis of the local environment during the ring-opening reaction indicated that while c-EC^- solvated Li^+ with its carbonyl O similar to EC in the pure EC system, as the transition state was traversed the ether oxygen interacts more with Li^+ resulting in considerable structural rearrangement of the first and second Li^+ solvation shells. Contrarily in EC/DMC, c-EC^- solvates Li^+ with both its carbonyl and ether O atoms and thus little reorganization occurs as the transition state is traversed. This difference in structural rearrangement can explain the significant barrier reduction from 0.23 to 0.09 eV with the addition of DMC. Furthermore, the tendency of c-EC^- to behave as another EC molecule in pure EC may also explain the significant difference in reaction energies as the

ring-stacking symmetry is broken when it becomes o-EC^- which could result in the less favorable reaction energy of only 0.6 eV.

These results show that intermolecular interactions are critical to understanding the reaction energetics within the complex environment within a LIB. Without the inclusion of explicit solvent molecules and the acyclic carbonate cosolvent, simulations predict that reduced EC should exist as c-EC^- for far longer than what is predicted with explicit EC/DMC solvent. The ability of DMC to facilitate ring-opening may be a critical role in the formation of the SEI which has gone unrecognized as it is conventionally regarded as a key component due to its ability to improve bulk ionic conductivity and reduce the melting point of the electrolyte.

Chapter 5 : Reduced Ethylene Carbonate Transport near Graphite Electrodes and its Impact on Solid Electrolyte Interphase Formation

5.1 INTRODUCTION

The electrolyte decomposition in lithium ion batteries must be a self-limiting process through the formation of a solid electrolyte interphase (SEI) to ensure operability of the battery, yet the SEI structure, and therefore properties, largely depends on its growth process. For example, a larger irreversible capacity loss is observed when the SEI is formed at elevated temperature[139]. This phenomenon is evidence that the SEI structure depends upon reaction and/or diffusion kinetics. Indeed, due to the presence of both electrochemical reactions at the interface and thermal reactions in solution, the interplay between reaction/diffusion processes should be expected to alter the decomposition pathways of the electrolyte as well as the precipitation of solid products during the growth of the passivating layer on the graphite electrode surface. The reaction kinetics of the reduced ethylene carbonate (EC) ring-opening reaction ($c\text{-}EC^- \rightarrow o\text{-}EC^-$) were explored in Chapter 4. In the following sections, the diffusion behavior of the $c\text{-}EC^-$ and $o\text{-}EC^-$ intermediate species near charged graphite electrodes and the effects of electrolyte composition and applied potential on $o\text{-}EC^-$ transport are discussed as well as how these factors can alter SEI formation.

Work in this chapter was published in Boyer, M. J.; Hwang, G. S. *J. Phys. Chem. C.* **2019**, *123* (29), 17695–17702. and Boyer, M. J.; Hwang, G. S. *Electrochim. Acta.* **2018**, *266*, 326–331. G.S.H. contributed in part to the planning of the studies and writing of the manuscripts.

5.2 METHODOLOGY

Classical molecular dynamics simulations were carried out following a similar approach to that outlined in Section 3.2; again, the OPLS-AA force field[86–88] was used and simulations were conducted using the GROMACS simulation package (versions 4.6.7 and 5.1.4)[89,140]. The same simulation architecture was used with a graphite electrode consisting of 10 ABAB stacked graphene nanoribbons with H-terminated zigzag edges. Two model electrolytes were used, both containing 592 solvent molecules and 1M $LiPF_6$. EC and DMC were mixed in 25/75 and 50/50 molar proportions and 47 and 45 Li^+/PF_6^- ion pairs were added, respectively. The electrode/electrolyte system was equilibrated by the same procedure, the electrode was contstrained in the same manner, and nonbonded interactions were considered in the same fashion as in Section 3.2.

Free energy profiles were constructed by a composite of five independent well-tempered metadynamics simulations of at least 100 ps in length based on different configurations. The collective variable (CV) was chosen as *z*-position of the carbonyl C atom of the reduced EC molecule. It was determined that five simulations was sufficient to sample the minimum pathway across the *x*-*y* plane at each *z*-position. In all simulations, harmonic walls were used to place upper and lower bounds on the CV limiting it to a 4 nm window. Gaussian hills with initial heights of 0.1 eV and widths of 0.5 Å were deposited every 0.1 ps; hill height was decayed by the well-tempered approach based on a ΔT of 7200K.

5.3 RESULTS AND DISCUSSION

In a theoretical study on the competition between formation pathways of EC-based SEI components, it was demonstrated that the product formed would depend on the relative rates of first and second charge transfer reactions, the c-EC^- ring-opening reaction, and the biomolecular combination reaction of two o-EC^- molecules.[83] However, as the electrode acts as the source of electrons for the reduction reactions, rates of intermediate diffusion of intermediates away from the interface relative to the charge transfer kinetics should also be considered in determining which species would be primarily produced during the early stages of SEI formation.

If diffusion is not considered, then assuming the second electron transfer is faster than the rate of the c-EC^- ring-opening reaction, c-EC^- will predominantly be reduced to form CO and glycoxide. Contrarily if ring-opening is faster but the second electron is faster than bimolecular combination, o-EC^- will be reduced to form CO_3^{2-} and C_2H_4. Lastly if bimolecular combination is faster than the second electron transfer, either butylene dicarbonate or ethylene dicarbonate and C_2H_4 will be predominantly formed. However, the inclusion of diffusion into this schema requires that the second electron transfer also be faster than diffusion of c-EC^-/o-EC^- away from the electrode for the glycoxide/CO_3^{2-} pathways to dominate.

5.3.1 Effect of Ring-Opening Reaction Kinetics on EC^- Transport

While diffusion behavior is important in determination of the final reductive decomposition products, if diffusion is fast relative to all reaction kinetics, it will also greatly affect the overall structure of the SEI and the irreversible capacity loss incurred during its formation. While the kinetics of the c-EC^-→o-EC^- reaction were demonstrated in Chapter 4 to be faster than previously reported due to the strong solvent effect resulting from the addition of dimethyl carbonate (DMC) to EC, the relative rates of ring-opening, c-EC^- reduction, c-EC^- and diffusion from the interface would determine whether or not the species is a short-lived intermediate or a critical component of the SEI formation process. Furthermore, the impact of ring-opening kinetics cannot be fully understood without evaluation of the relative transport rates of c-EC^- and o-EC^-.

From classical molecular dynamics simulations of c-EC^- and o-EC^- in a bulk electrolyte consisting of 1M $LiPF_6$ in 50/50 EC/DMC the self-diffusivity (D) may be predicted by the mean-squared displacement ($[r(t)-r(t_0)]^2$) using the equation:

$$D=\frac{1}{N}\sum_{i=1}^{N}\frac{\langle[r_i(t)-r_i(t_0)]^2\rangle}{6t} \tag{5.3.1}$$

where t is time, N is the number of molecules averaged over in the simulation, and ⟨ ⟩ denotes an ensemble average taken over trajectories of length $t - t_0$. This approach yields diffusivities of 3.2×10^{-7} cm^2/s and 2.7×10^{-7} cm^2/s for c-EC^- and o-EC^-, respectively; for comparison, in the same electrolyte EC and Li^+ have predicted diffusivities of 2.9×10^{-6} cm^2/s and 8.1×10^{-7} cm^2/s, respectively. In bulk solution, both radical anions are shown to

have relatively poor mobility, but to not differ greatly from one another, though c-EC^- appears to be the slightly more mobile species.

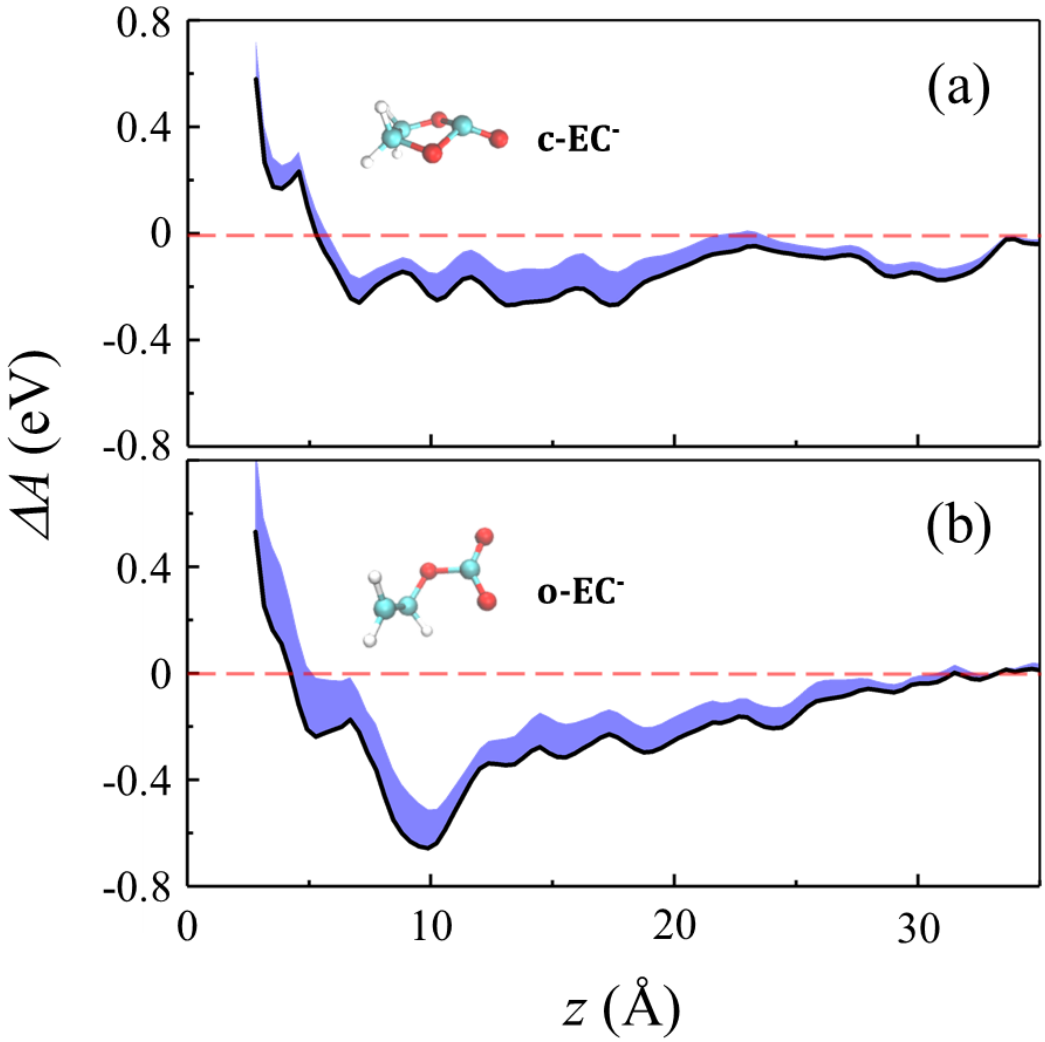

Figure 5.1. Relative Helmhotz free energy (ΔA) profiles (black line) with standard deviation (blue area) from minimum free energy pathway across simulations for the carbonate C atom of EC^- along the axis perpendicular to the electrode surface (z) for EC^- in the ring configuration (a) and the chain configuration (b) when a graphite electrode with surface charge density σ = -9.7 $\mu C/cm^2$ is immersed in a 1M $LiPF_6$ in 50/50 EC/DMC electrolyte.

Diffusion in the bulk, however, is less important than that near the electrode/electrolyte interface as these species are formed by reduction reactions occurring at the interface. To evaluate the diffusion behavior of c-EC^- and o-EC^- near a charged graphite electrode surface, well-tempered metadynamics simulations were performed. From these simulations, the ΔA profile was then used to evaluation migration of c-EC^-/o-EC^- away from the electrode towards the bulk similar to the investigation of Li^+ cation transport in Chapter 3. For the electrode, a surface charge density of σ = -9.7 $\mu C/cm^2$ is assigned by the addition of excess negative charge to the electrolyte adjacent C atom; this σ was chosen as it approximates 1.2 V *vs.* Li/Li^+, as shown in Chapter 3, where the electrolyte tends to be first reduced[4,31]. For the same 50/50 EC/DMC electrolyte as used to study the bulk diffusion, ΔA is shown along the direction perpendicular to the graphite edge plane (z) for [(a)] c-EC^- and [(b)] o-EC in Figure 5.1; positions are taken with respect to the carbonyl C (C_C) of both molecules.

Features along the ΔA profiles are attributed to configurations through analysis of the metadynamics trajectory to contextualize the free energy pathway. In [(a)], the minima at $z \approx 4$ and 7 Å correspond to c-EC^- at the interface with its ring-plane perpendicular and parallel to the graphene layers, respectively. In the latter case, the ethylene group is directed towards the electrode and the carbonyl O (O_C) atom away such that the dipole may screen the electric field emanating from the charged electrode. The series of minima spanning from $z \approx 10$ and 17 Å correspond to fully solvated states where at least one solvent layer exists between c-EC^- and the electrode, yet the electrolyte is bulk-like in its organization.

Beyond $z \approx 32$ Å the electrolyte is bulk-like and ΔA becomes nearly flat with the exception of some minor oscillations. The first minimum at $z \approx 4$ Å is both shallow and a local minimum which suggests that c-EC^- would be unlikely to exist at the interface such that its dipole is perpendicular to the electric field consistent with expectation. The second minimum at $z \approx 7$ Å is, however, stable but is nearly equal in ΔA to the third minimum at $z \approx 10$ Å; with only a maximum of approximately 50 meV separating them, c-EC^- could easily diffuse away from the interface where it would be fully solvated. Furthermore, this maximum is even smaller than the barrier observed in Chapter 4 of 90 meV for ring-opening to o-EC^-. However, if c-EC^- did persist for any appreciable duration, it would only be held at/near the interface by a well of depth $\Delta A \approx 0.2$ eV relative to the bulk-like region.

In contrast, for [(b)] the feature at $z \approx 4$ Å only appears as a shoulder while the minimum, which has shifted towards the electrode, at $z \approx 5$ Å is quite shallow; the shift in location of minimum is likely the result of the chain-like structure arranging itself differently than the ring as the primary dipole now exists along a sing C-O bond. The minimum at $z \approx 10$ Å is far deeper (about 0.5 eV below the first) which indicates there is a large driving force for o-EC^- to diffuse away from the interface to where it can be fully solvated. From this minimum, ΔA increases somewhat gradually until $z > 3$ nm where the electrolyte becomes bulk-like and the profile becomes flat except for some minor oscillations. Unlike in [(a)] where c-EC^- showed no clear preference between the stable surface and solvated states, o-EC^- would likely move to the location of the deep well at $z \approx 10$ Å due to the large driving force relative to the small maximum separating these states;

there it would need to overcome a gain in $\Delta A \approx 0.7$ eV in order to diffuse away from the interface into the bulk-like region of the electrolyte, indicating that o-EC^- is far more likely to remain in proximity to the electrode than c-EC^-.

While the diffusion behavior in the bulk electrolyte differed by less than an order of magnitude as predicted by the self-diffusivity, the considerable difference in the depth of the minimum in the free energy profile near the changed graphite electrode suggests that c-EC^- diffusion towards the bulk would likely be several orders of magnitude higher due to the exponential relationship between energy and rate. Because of this, the ability of DMC to improve c-EC^- ring-opening kinetics shown in Chapter 4 may also serve to prevent irreversible capacity fade due to the migration of the charged intermediate towards the cathode. Furthermore, the interplay between reaction and diffusion kinetics suggests that increasing temperature could to some extent reduce the mobility of EC^- contrary to conventional understanding as the improved ring-opening kinetics would on net reduce the mobility of EC^- due to the kinetic trapping of o-EC^- near the electrode.

5.3.2 Effect of Electrolyte Composition on o-EC^- Transport

It was demonstrated in Chapter 4 that in mixed EC/DMC electrolytes, the local perturbations in the electrolyte may contribute to facile c-EC^- ring-opening, making o-EC^- the predominant intermediate. In the previous section, o-EC^- was shown to favorably diffuse away from the electrode to a distance of about 1 nm from the interface where it would persist for a relatively long time period compared to the initial diffusion event within

an electrolyte consisting of an equimolar mixture of EC and DMC. As discussed previously in this chapter, it would be unlikely given the rate of this diffusion for o-EC^- be reduced to produce CO_3^{2-}, yet previous studies have shown the SEI composition[46] and impedence[26,48,105] to be sensitive to that of the bulk electrolyte. It was proposed the formation of CO_3^{2-} would be more favorable in systems with low EC concentrations[20] which was attributed to the decreased probability of two reduced EC molecules interacting, however, the reduction of o-EC^- would require reasonably large residence times at the interface regardless of electrolyte composition. To evaluate the origin of electrolyte composition dependence on the SEI, o-EC^- diffusion near an electrode was evaluated in a 1M $LiPF_6$ in 25/75 EC/DMC electrolyte to compare with the 50/50 electrolyte from the previous section. ΔA profiles for each system (near a graphite electrode with σ = -9.7 $\mu C/cm^2$) are shown in Figure 5.2.

The features of [(a)] the 50/50 electrolyte were discussed in the previous section; in [(b)] the 25/75 electrolyte, two similar surface features are observed with the first at $z \approx$ 3 Å being unstable and the second, a pronounced minimum from $z \approx$ 5 - 6 Å, indicating that (at least in some regions) o-EC^- may exist favorably at the interface. It should be noted that the larger shaded area above the minimum ΔA profile in [(b)] when compared to [(a)] shows that greater variability in pathways exists in the 25/75 electrolyte, which may result from greater heterogeneity of structure within the *x*-*y* plane. A second minimum in ΔA of equal depth to the stable surface state (similar to what was observed for c-EC^- in a 50/50 mixture) can be seen at $z \approx$ 14 Å. The two wells along the profile are separated by a

maximum of $\Delta A \approx 0.3$ eV, which may allow for some o-EC^- to remain at the interface to be reduced further to form CO_3^{2-}. Beyond the second well, ΔA steadily increases (with some oscillation) by $\Delta A \approx 0.4$ eV where it levels off and becomes flat except for minor oscillations due to the bulk-like nature of the electrolyte when $z > 30$ Å.

Unlike in the previous section, the differences in the free energy profiles cannot be attributed the nature of the diffusing species, rather, they must result from differences in interactions with the surrounding molecules. In order to explain these differences, the interfacial structures of [(a)] and [(b)] were evaluated through the number density (ρ_n) which is shown for the center of mass of each electrolyte component along the z direction in Figure 5.3; the ρ_n profiles for Li^+ and PF_6^- are replotted at a second scale in the inset to highlight fine details.

In both [(a)] and [(b)], peaks corresponding to EC and DMC in the first solvent layer appear at $z \approx 4$ and 4.5 Å, respectively. While the peak in DMC ρ_n is larger in [(b)], the increase is not proportional to that of its bulk composition. Yet the relatively lower concentration in EC is reflected in the Li^+ ρ_n which exhibits a pronounced tail in only [(b)] from about $z = 3.5$ to 5.5 Å on the first peak which occurs at $z \approx 7$ Å in both cases. The significant Li^+ peaks are the result of accumulation due to the orientation of solvent carbonyl O (O_C) atoms away from the negatively charged electrode; as DMC is not as efficient as EC in screening this field, the decrease in EC in [(b)] results in the incorporation of some Li^+ into the first layer to assist in the shielding of the electrode. A secondary effect

of this inclusion in the first layer is the stabilization of o-EC^- at the interface due to the strong electrostatic interactions between the radical anion and the Li^+ cations.

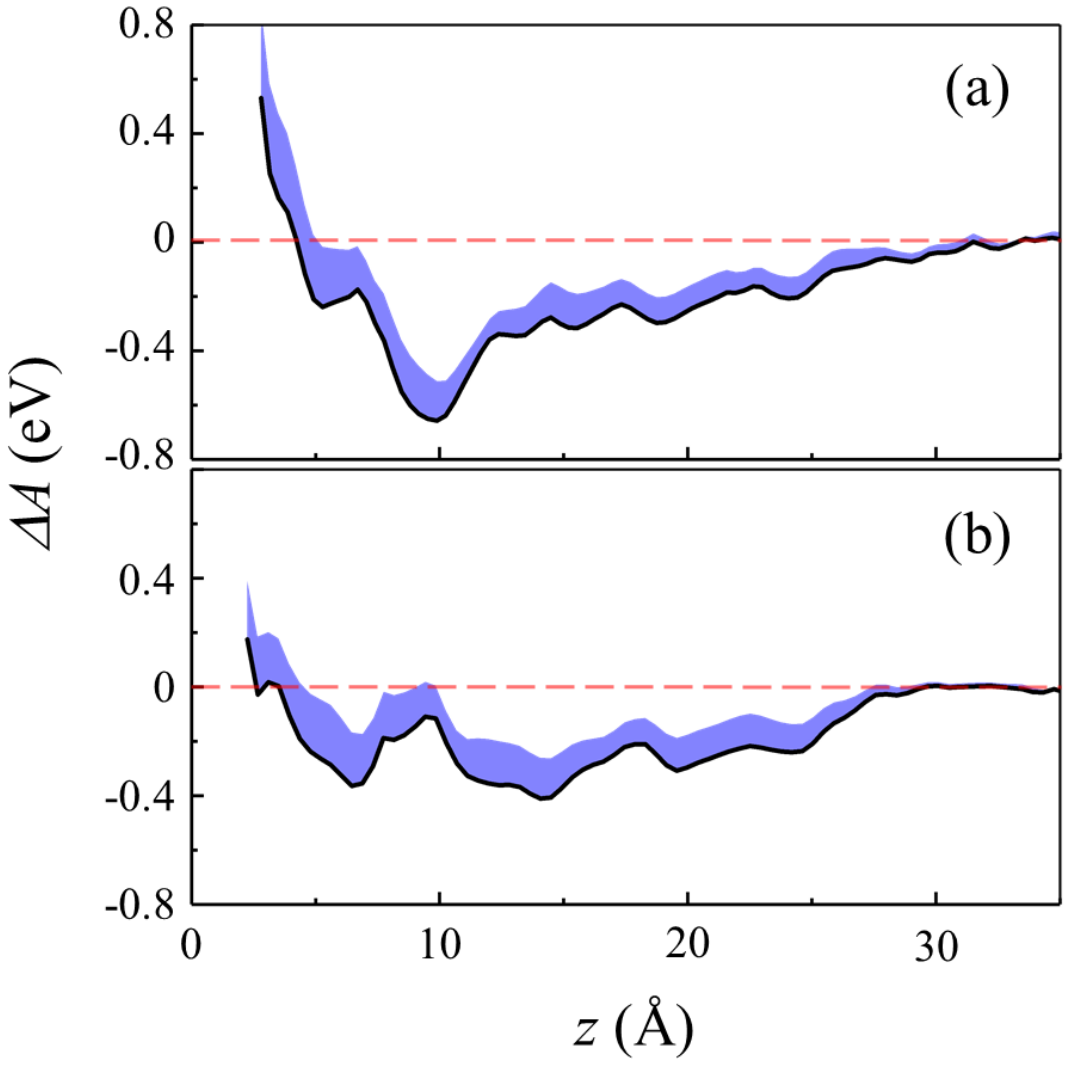

Figure 5.2. Relative Helmhotz free energy (ΔA) profiles (black line) with standard deviation (blue area) from minimum free energy pathway across simulations for the carbonate C atom of EC^- along the axis perpendicular to the electrode surface (z) for o-EC^- in a 1M $LiPF_6$ in 50/50 EC/DMC electrolyte (a) and a 1M $LiPF_6$ in 25/75 EC/DMC electrolyte near graphite electrodes with surface charge densities σ = -9.7 $\mu C/cm^2$.

Further inspection of the metadynamics trajectories from [(a)] and [(b)] reveal that o-EC^- tends to remain tightly bound to two Li^+ cations and at times interacts with a third. This observation is consistent with similar studies which have described the formation of contact ion pairs between cations and ions[141] when the solvent-cation interactions are weak relative to the cation-anion interactions. Snapshots shown in Figure 5.4 show that in [(a)] for o-EC^- to exist at the interface, EC molecules reorient in order to cosolvate the Li^+ cations bound to it. This reorientation compromises the ability of EC to shield the negatively charged electrode by changing the orientation of its dipole. By comparison, in [(b)] the DMC molecules may orient their methyl groups towards the electrode while organizing around the Li^+ cations due to their flexible structure. This interplay between orientation of solvent to screen the electric field emanating from the anode and also orientation around Li^+ cations bound to o-EC^- determines the relative stability of o-EC^- and is likely the reason even in [(b)] not all surface states were found to be favorable. Away from the electrode ($z \approx 10$ - 15 Å) the local abundance of Li^+ cations may increase the solubility of the o-EC^- anion relative to the bulk as solvent rearrangement does not incur the same energy penalty here as at the interface. Therefore, the steady increase in ΔA beyond $z = 18$ Å towards the bulk is likely the result of a continuously decreasing local concentration of Li^+ (though oscillatory in nature) until the bulk composition is reached.

This section indicates that the interplay between electrolyte-electrolyte and electrode-electrolyte interactions are critical in understanding the diffusion behavior of o-EC^- away from the graphite anode towards the bulk where it is unlikely to be reduced to

form CO_3^{2-}. While it was previously though that in electrolytes with relatively low EC concentrations that the tendency to form CO_3^{2-} was the result of the decreased probability of o-EC^- bimolecular reactions occurring due to low concentration, the results outlined here suggests that instead it is the increased presence of DMC at the interface which may help to stabilize o-EC^- on the graphite surface, slowing the rate of its diffusion away. The formation of a highly ordered and compact layer of EC at the interface at higher EC concentrations decreases this stability and promotes the diffusion of o-EC^- away and, by decreasing the probability of its reduction to CO_3^{2-}, increases the probability of it undergoing a bimolecular reaction to form an alkyl carbonate. A secondary effect of the change bulk electrolyte composition is the shrinking of free energy difference between the region near the electrode and the bulk with the addition of more DMC. This suggests that for such electrolytes, it could be expected that more o-EC^- would diffuse away from the interface where it may not contribute to the formation of the SEI at all or result in a thick and diffuse SEI layer.

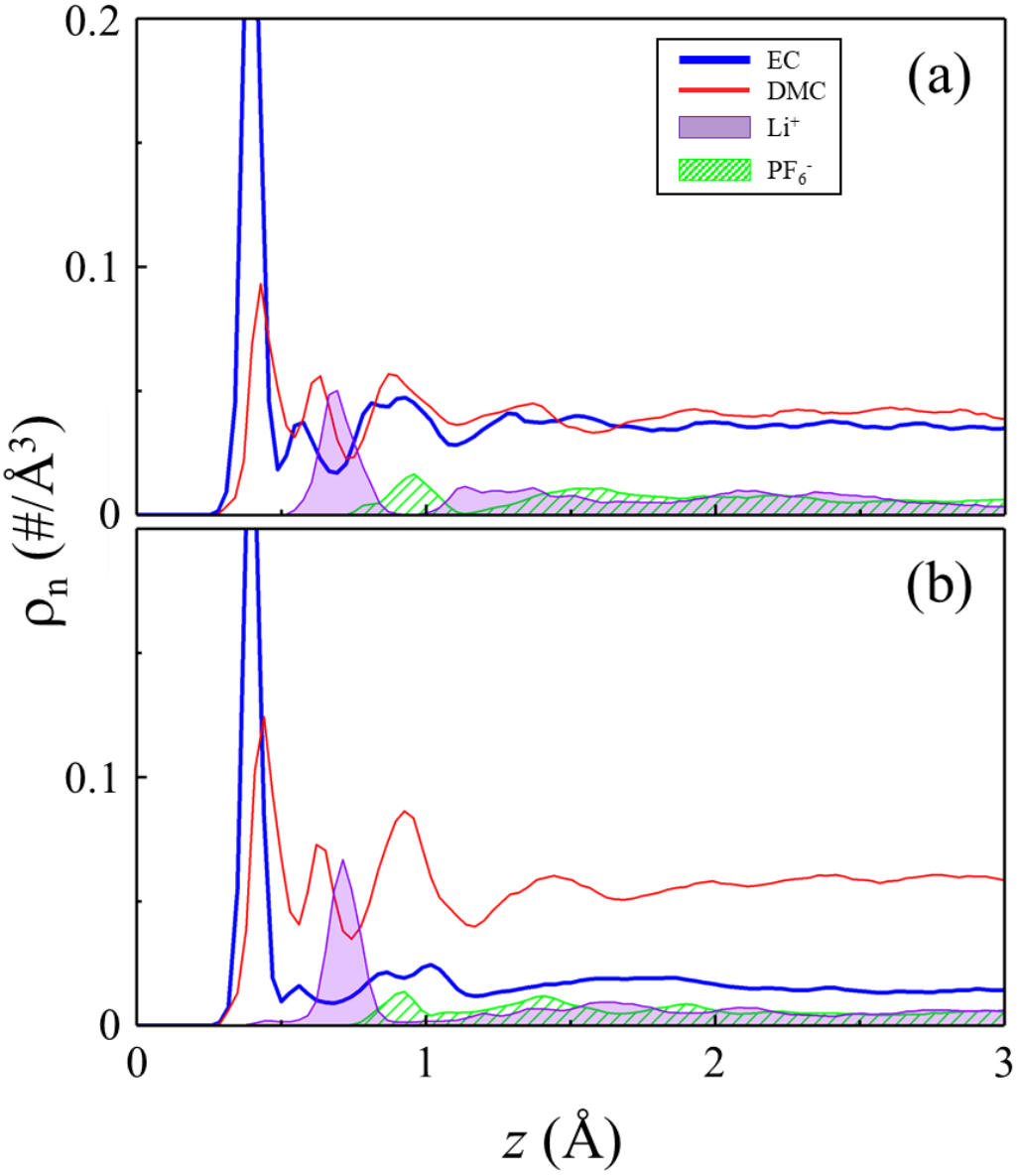

Figure 5.3. Number density (ρ_n) profiles of EC (blue), DMC (red), Li^+ (purple), and PF_6^- (green) along the direction normal to the electrode surface (z) for a 1M $LiPF_6$ in 50/50 EC/DMC electrolyte (a) and a 1M $LiPF_6$ in 25/75 EC/DMC electrolyte (b) near graphite electrodes with surface charge densities σ = -9.7 $\mu C/cm^2$.

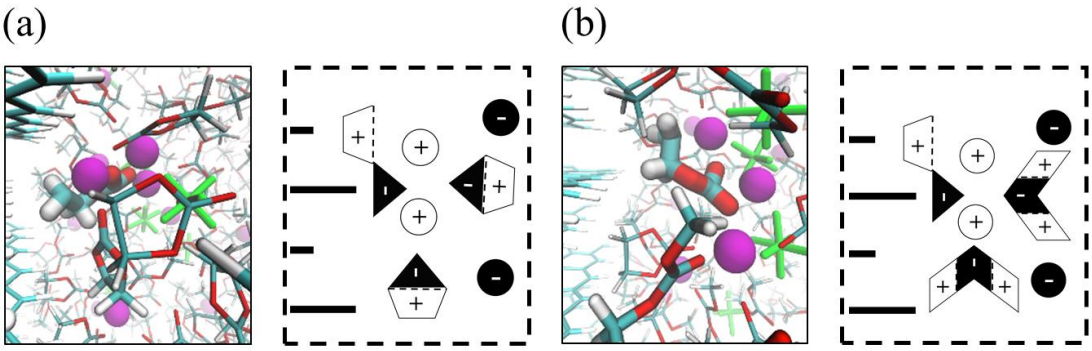

Figure 5.4. Screenshot (left) and schematic (right) of solvation of Li^+ cations interacting with o-EC^- while it is at the electrode surface in 1M $LiPF_6$ in 50/50 EC/DMC electrolyte (a) and 1M $LiPF_6$ in 25/75 EC/DMC electrolyte (b).

5.3.3 Effect of Applied Potential on o-EC^- Transport

The previous section highlighted the effect of the bulk electrolyte composition on the transport of o-EC^- near graphite electrodes, and in particular, discussed how the reorganization of the electrolyte to screen the field emanating from the electrodes alters the ability of the electrolyte to organize around o-EC^- into a stable configuration. It has been observed experimentally that the SEI properties depend upon the rate at which the voltage is changed during the formation cycle[103,104]. Furthermore, it has also been observed that the stability of the SEI depends both on the voltage it was formed at and the electrolyte composition[47]. This section will evaluate the dependence of applied potential on o-EC^- transport in both 50/50 and 25/75 EC/DMC electrolytes.

Figure 5.5 shows the ΔA profiles for o-EC^- in [(a)] the 50/50 electrolyte and [(b)] the 25/75 electrolyte near graphite electrodes with σ = -6.4, -9.7, and -12.1 $\mu C/cm^2$. In [(a)], the less negative surface charge case (σ = -6.4 $\mu C/cm^2$) exhibits the same major

features as the profile previously discussed. While the more negative surface charge case (σ = -12.1 $\mu C/cm^2$) shows a clear change in profile shape. In the first two profiles, only one pronounced minimum is observed; in the less charged case, this minimum is deeper and shifted towards the electrode surface, though it still represents a fully solvated state. In the more negative surface charge case, two shallow minima can be observed corresponding to both surface and fully solvated near-surface states, yet both are near in ΔA to the bulk. By comparison, in [(b)] all three profiles exhibit the same general shape, namely the existence of a surface and near-surface minimum which are both lower in ΔA than the bulk. However, as the electrode is charged more negatively the symmetry of those minima changes with the near-surface minimum being deeper in the less negative case and the surface minimum being deeper in the more negative case.

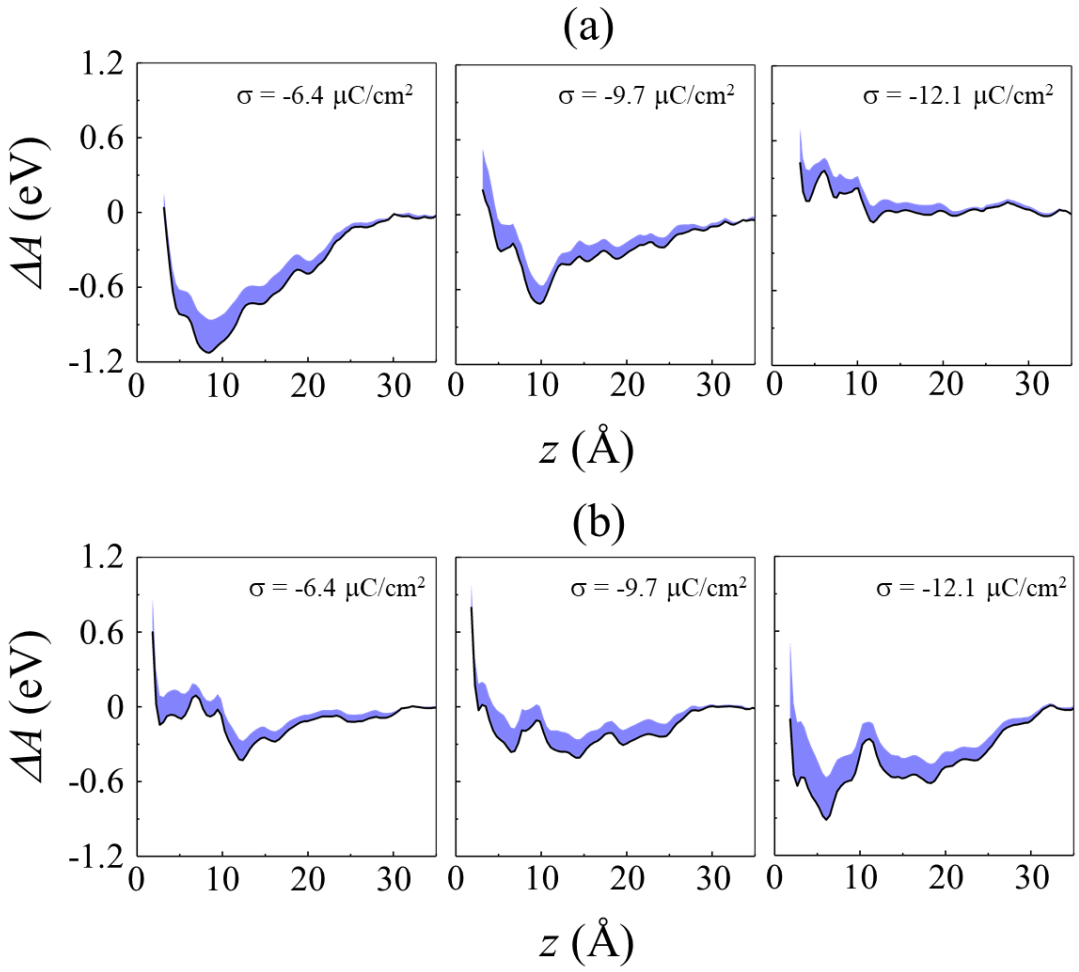

Figure 5.5. Relative Helmhotz free energy (ΔA) profiles (black line) with standard deviation (blue area) from minimum free energy pathway across simulations for the carbonate C atom of EC^- along the axis perpendicular to the electrode surface (z) for o-EC^- in a 1M $LiPF_6$ in 50/50 EC/DMC electrolyte (a) and a 1M $LiPF_6$ in 25/75 EC/DMC electrolyte near graphite electrodes with surface charge densities σ = -6.4, -9.7, and -12.1 $\mu C/cm^2$.

The effect of the electrode charge state on the ΔA profiles can be better understood through inspection of the EC and Li^+ ρ_n profiles which are shown in Figure 5.6. In particular, a depletion of EC at the interface and/or the presence of Li^+ partially precipitated onto the graphite edge appears for all five systems where a stable surface state exists.

Furthermore, in [(a)] the width of the free energy well appears to correspond to the width of the Li^+ peak at $z \approx 7.5$ Å. Indeed, the strong electrostatic interactions between o-EC^- and Li^+ appear to largely determine its spatial preference with some additional dependence, in the case of the first layer, on the structural packing of the solvent molecules.

This section highlights the importance of considering not only the bulk electrolyte composition, but also the operating voltage during the SEI formation cycle. More importantly, it indicates these effects are not fully independent of one another, but should be considered in tandem due to the determination of interfacial structure by the interplay between voltage and composition. While at more moderate potentials, electrolytes containing higher concentrations of EC appear to more effective at trapping o-EC^- near the electrode, but at more negative potentials an abundance of DMC at the interface allows for its incorporation into the first solvent layer when disruption of the tightly packed EC layer begins to occur. Generally, it was observed that across all potentials, it would be more likely for CO_3^{2-} to be formed when DMC is abundant due to the exclusion of o-EC^- from the first solvent layer when sufficient EC is present for a uniform layer to be formed at the interface. Other factors not considered in this chapter such as elevated temperature or the presence of other decomposition products/intermediates would likely effect transport behavior and should be considered in the future to fully understand the SEI formation process. However, due to the ionic nature of both the products and the intermediates, diffusion processes during the early stages of SEI formation are likely to have the most

significant effect on the SEI structure as aggregation/precipitation are expected to limit the mobility of species similar to how the ring-opening reaction limits the mobility of EC^-.

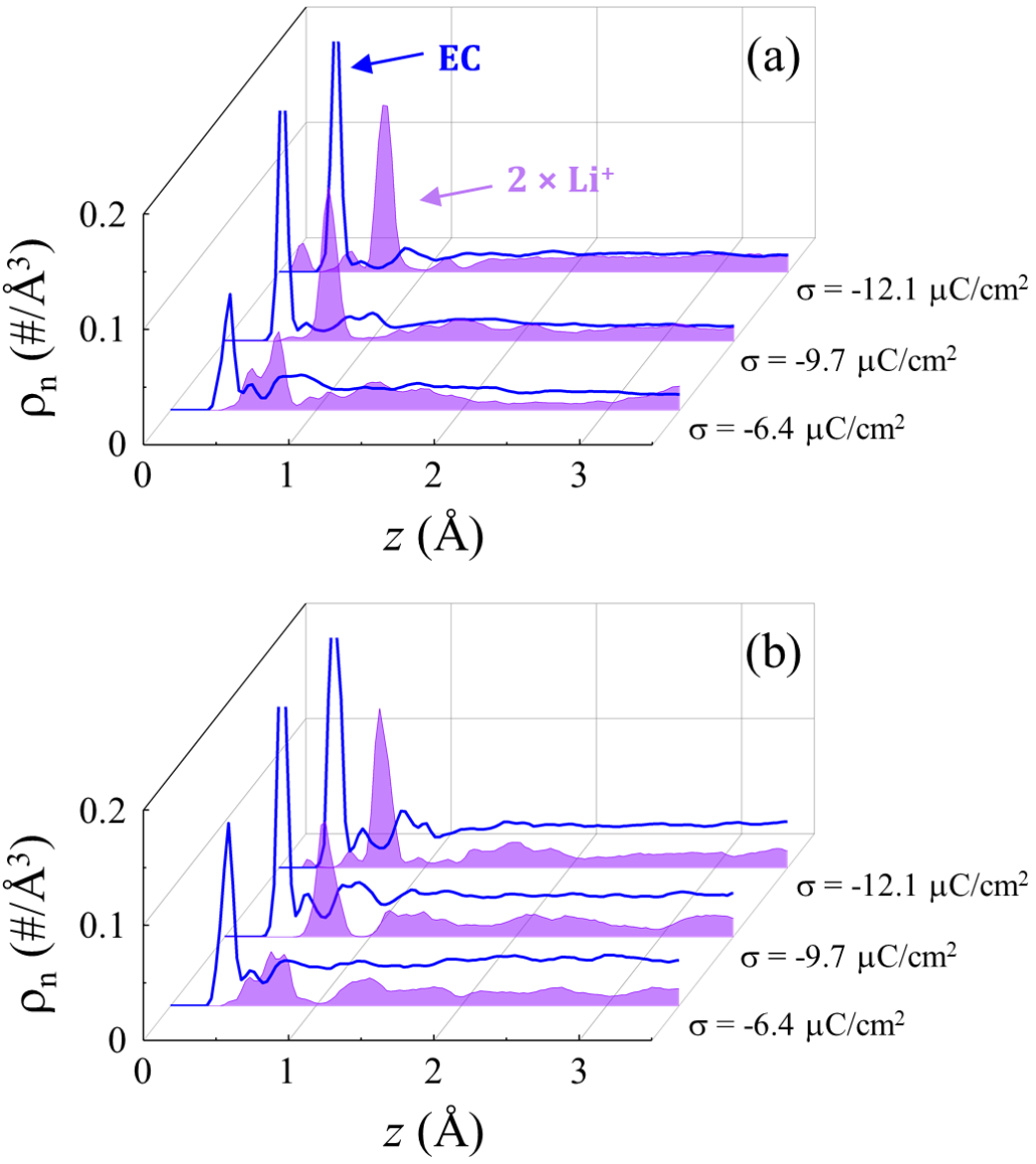

Figure 5.6. Number density (ρ_n) profiles of EC (blue) and Li^+ (purple) along the direction normal to the electrode surface (z) for a 1M $LiPF_6$ in 50/50 EC/DMC electrolyte (a) and a 1M $LiPF_6$ in 25/75 EC/DMC electrolyte (b) near graphite electrodes with surface charge densities σ = -6.4, -9.7, and -12.1 $\mu C/cm^2$. The ρ_n of Li^+ is scaled by a factor of 2 so that the details can be more easily observed.

5.4 SUMMARY

Considerable effort has been directed at the study of reductive decomposition of EC to determine the origin of its ability to form a stable SEI allowing for the operability of the LIB. Previous studies have largely focused on determining the final products through *post mortem* experiments and density functional theory simulations. However, the SEI formation process wherein the decomposition of the electrolyte ultimately results in the formation of a solid film, remains poorly described. Furthermore, mechanistic studies of reduction of the electrolyte have largely neglected diffusion of reduced electrolyte species on subsequent reduction processes. To better understand how diffusion of reduced EC intermediate species affects the composition of the SEI through reaction kinetics and the structure of the SEI through distribution of products, classical molecular dynamics simulations were performed at a graphite electrode/electrolyte interface.

The relative mobility of reduced EC as a ring (c-EC^-) and in the open chain configuration (o-EC^-) were compared to demonstrate the how the ring-opening reaction rate would affect intermediate diffusion. While in the bulk c-EC^- has a self-diffusivity which is larger by less than an order of magnitude, near a graphite electrode with a surface charge which approximates to the reduction potential of EC, the free energy profiles show that c-EC^- would be significantly more likely to diffuse away from the electrode towards the bulk; while both species have no significant free energy well at the interface, o-EC^-

would be held within 20 Å of the interface by an energy well of about 0.7 eV whereas c-EC^- is only held by a similar minimum of 0.2 eV. This finding suggests that the promotion of ring-opening overall serves to hinder intermediate diffusion at the interface. This may result in a non-monotonic temperature effect as increasing temperature will result in increased mobility due to an increase in thermal energy, but it will also improve the ring-opening kinetics which were also shown to be improved by the addition of DMC to EC in Chapter 4. Furthermore, as neither species had a significant minimum at the interface, it is unlikely for a second electron transfer to occur prior to the reduced species moving away from the interface where it can be fully solvated, assuming modest electron transfer rates. Because of this, the two-electron reduction of EC to produce the glycoxide dianion and CO is unlikely to occur given the tendency of SEI formation cycles to be carried out at a charge rate of C/20. Furthermore, for the electrolyte considered in this section (1M $LiPF_6$ in 50/50 EC/DMC) it is also unlikely for o-EC^- to be reduced to form CO_3^{2-} and C_2H_4 as regardless of the ring-opening rate, both c-EC^- and o-EC^- can be expected to be solvated away from the interface.

Given the small predicted ring-opening barrier for c-EC^- shown in Chapter 4, the diffusion behavior of o-EC^- was studied in more detail based on the assumption that ring-opening may occur instantaneously upon the reduction of EC due to the disorder near the interface. In order to elucidate the effect of bulk electrolyte composition on the diffusion of o-EC^- near the electrode, the results from the 50/50 EC/DMC electrolyte were compared with those of a 25/75 EC/DMC electrolyte. Similar to how Chapter 4 demonstrated the

significant effect of DMC on ring-opening kinetics, the additional DMC alters the free energy profile for o-EC^- drastically. While the pronounced minimum for the near-interface solvated stated becomes more shallow (≈ 0.4 eV) a pronounced minimum at the interface can be sampled along some metadynamics trajectories with a depth of ≈ 0.3 eV. From a detailed analysis of the local environment and the interfacial structure, it was found that the formation of the uniform layer of EC molecules with their carbonyl O atoms oriented away from the electrode in the 50/50 electrolyte precludes o-EC^- from being stabilized at the interface. However, in the 25/75 electrolyte insufficient EC is present to form such a layer and the presence of DMC-rich regions at the interface allow for the stabilization of o-EC^- due to the ability of DMC to orient its methyl group towards the electrode thus screening the electric field while also directing its carbonyl O towards the Li^+ cations surrounding o-EC^-; in comparison, EC is shown to rotate its dipole perpendicular to the interface while solvating the same cations. This result suggests that it could be expected to find more CO_3^{2-} within the SEI formed from an electrolyte leaner in EC due to the interfacial structure.

The sensitivity of the o-EC^- mobility was shown not to be restricted to the electrolyte composition. In fact, the interplay between the applied potential and the electrolyte composition can dramatically alter the interfacial structure which in turn affects the diffusion behavior of o-EC^- near the interface. The free energy profiles were constructed for both electrolytes at applied potentials above and below the model system approximating the reduction potential of EC. In the 50/50 electrolyte, the profile exhibits

the same features above the reduction potential with the minimum becoming deeper. However, negative of the reduction potential the presence of Li^+ cations precipitated onto the electrode surface perturbs the interfacial structure and results in metastable states at the interface while nearly eliminating the minimum corresponding to the solvated state. In the 25/75 electrolyte, the two minima are observed in all three cases. At the reduction potential the surface and solvated states were shown to be approximately equal in energy, but above this potential the surface state is higher in energy than the solvated state. Contrarily, below the reduction potential, the surface state is lower in energy than the solvated state. From this analysis, it can be seen that the potential at which the SEI forms would not only affect the rate of electron transfer, but also the mobility of the reduced species. However, this model does not included the effect of other reduced species on the diffusion behavior which could be expected below the reduction potential.

The diffusion behavior summarized here has been largely ignored except at the continuum scale where Fickian diffusion is modeled based on bulk diffusivity and concentration. However, the nanoscale structure at the interface results in nanoscale diffusion effects which may be critical to understanding the formation of the SEI as it is itself only a few to tens of nanometers in thickness. Furthermore, the diffusion behavior which was shown to be sensitive to changes in the interfacial structure induced by modulating the applied potential and by changing the bulk electrolyte composition would also be sensitive to changes in temperature, the inclusion of additives, and the dynamic composition due to the reduction of the electrolyte.

Chapter 6 : Formation of Alkyl Carbonates by Radical Combination

6.1 INTRODUCTION

Since Aurbach and coworkers identified lithium alkyl carbonates as products in the solid electrolyte interphase (SEI),[19,114] their formation has been extensively studied through both experiments[48,117,121,142–147] and simulations[83,107,109,110,148,149] towards understanding how a stable SEI layer is formed. In contrast with the two-electron reduction of ethylene carbonate (EC) to either CO_3^{2-} and C_2H_4 or a glycoxide dianion and CO, the one-electron reduction pathway to either ethylene dicarbonate (EDC^{2-}) and C_2H_4 or butylene dicarbonate (BDC^{2-}) requires two anionic species to thermally react through bimolecular combination. Although it may be thermodynamically favorable for these reactions to occur[107], the kinetics may not be as easily described due to the diffusion component, which has been proposed to be limiting in previous studies[83]. Reactive force field (ReaxFF) simulations have been applied to this reaction[109,110] due to their ability to achieve the necessary scale at reasonable computational cost, however, these simulations suggest a wide range of products would be formed beyond the alkyl carbonates EDC^{2-} and BDC^{2-}. Furthermore, such methods suggest that BDC^{2-} would be the dominant product which would indicate that the C_2H_4 gas evolved during SEI formation[121,146] would then be attributed to the formation of CO_3^{2-}.

Work in this chapter was published in Boyer, M. J.; Hwang, G. S. *Phys. Chem. Chem. Phys.* **2019**, *Under Review*. G.S.H. contributed in part to the planning of the studies and writing of the manuscripts.

Due to the anionic nature of the radical intermediate (EC^-), the description of the local solvation environment would be critical to their interaction in solution. While at high concentrations, reactions may occur due to random collisions, this may not accurately describe such reactions during the early stages of SEI formation where few reduction reactions have occurred. Simulations have predicted that reduced EC is likely to undergo ring-opening and diffuse away from the interface quickly during the early stage of SEI formation, preventing two-electron reduction mechanisms.[150,151] Furthermore, EC^- was shown to strongly interact with Li^+ cations forming contact ion pairs. Similar to the diffusion away from the electrode discussed in Chapter 5, the diffusion of EC^- towards another EC^- molecule should largely depend on the interplay between EC^--EC^- and EC^--electrolyte interactions. Description of how the radical anions interact in solution is critical to understanding their reaction which would also depend on the local environment like the ring-opening reaction in Chapter 4.

In this chapter, classical molecular dynamics (CMD) simulations are utilized to demonstrate the aggregation of o-EC^- molecules in bulk electrolyte and near electrode surfaces as a function of their concentration prior to chemical reactions. As classical force fields cannot describe the formation of chemical bonds, this allows for the decoupling of diffusion and aggregation behavior from the chemical reaction which is then described through the use of *ab initio* molecular dynamics (AIMD) simulations based on density functional theory (DFT). The combining of CMD and AIMD simulations can access time- and size- scales beyond even ReaxFF simulations allowing for a detailed description of the

rate of alkyl carbonate formation under different conditions as well as the competition between EDC^{2-} and BDC^{2-} formation

6.2 METHODOLOGY

Classical molecular dynamics simulations were carried out using the OPLS-AA force field[86–88] within the Gromacs 5.1.4 simulation package[140]. Bulk liquid simulation cells were constructed containing 296 EC molecules, 296 DMC molecules, 45 Li^+/PF_6^- ion pairs, and between 2-25 $Li^+/o\text{-}EC^-$ ion pairs. Simulations were conducted with a graphite electrode modeled as in Section 3.2 with a surface charge density of σ = -9.7 $\mu C/cm^2$ and 500 (250) EC, 500 (750) DMC, and 76 (78) Li^+/PF_6^-. Both bulk and interface simulation boxes were equilibrated following the same procedure as in Section 3.2.

Upon equilibration, production simulations for the bulk systems were carried out at 300K for 10 ns without constraints and for 100 ns while utilizing the well-tempered metadynamics algorithm[65] as implemented within the PLUMED plugin[92]. During metadynamics simulations, the collective variable (CV) is chosen as the radial distance between the carbonyl carbon (C_C) atom of two difference $o\text{-}EC^-$ molecules. Harmonic walls are enacted to limit the CV-space to a distance of 30 Å. Gaussian hills with an initial height 0.10 eV and width σ = 0.5 Å were deposited every 0.1 ps and tempering was applied based on a ΔT of 7200K.

Dynamic composition CMD simulations (MD/MC) were conducted for both interface systems through the combination of CMD simulations and Monte Carlo (MC)

steps similar to the approach of Takenaka and coworkers[149,152,153]. EC molecules were substituted with EC^- (and compensating Li^+ was added) within the simulation box between subsequent NPT and NVT simulations each run for equal time and the sum of which will herein be referred to as the relaxation time (τ). After each CMD step, an EC molecule was chosen from a weighted distribution; the weight (W) was defined as:

$$W = \exp(\alpha z) \tag{6.2.1}$$

(based on tunneling probability[84]) where z is the distance of EC from the graphite edge surface and α is a constant which was assumed to be 1.2 $Å^{-1}$. Simulations consisting of 150 MD/MC cycles were conducted with τ = 20, 100, and 500 ps (all at 300K).

Quantum mechanical calculations were performed using hybrid Becke 3-Lee–Yang–Parr (B3LYP)[122,123] exchange-correlation functionals and the 6-311++g(d,p) basis set within the Gaussian 16 suite of programs[125] as described in Section 4.2. Solvent effects were considered through the polarizable continuum model[126] and acetone was selected as the model solvent.

AIMD simulations were conducted within the Car-Parrinello MD (CPMD) framework as described in Section 4.2. Simulation boxes were constructed containing a $2Li^+/2EC^-$ dimer and 24 (27) solvent molecules for equimolar EC/DMC (pure EC). Metadynamics simulations were performed until a single reaction event occurred 1(2 – 40 ps of simulation time) for both the Li_2EDC and Li_2BDC formation pathways; three trials were conducted for each. From the each set of three trials the minimum free energy pathway was selected as the representative pathway. For the Li_2EDC pathway, the

collective variable (CV) was chosen to be the distance between the radical C atom of ethylene group (C_E) of one EC^- molecule and one of the nucleophilic carboxyl O (O_C) atoms on the other EC^-; in all cases the pair with the shortest distance in the equilibrium structure was selected as the CV. For the Li_2BDC pathway the CV was chosen as the distance between the C_E atoms of each EC^-.

6.3 Results and Discussion

The following sections discuss the formation of the alkyl carbonates EDC^{2-} and BDC^{2-} by the solution phase reaction of two EC^- radicals by first describing how EC^- molecules interact in the bulk as a function of concentration. Next, EC^--EC^- interactions are evaluated near a polarized electrode surface through MD/MC simulations to illustrate the effect of electron transfer rate and electrolyte composition on such interactions. Aggregate structures observed in CMD simulations are then taken as model systems for the study the radical combination reactions using CPMD and metadynamics. Finally, the effect of the local environment on the reaction barriers is discussed.

6.3.1 Concentration Dependent Aggregation of Reduced EC

To elucidate the effect of Li^+/EC^- concentration on EC^- bimolecular interactions in bulk electrolyte conditions, CMD simulations were performed for systems containing 0.04-0.52 M EC^-. Figure 6.1 shows a screenshot of the resulting configuration of cations and anions from a simulation box containing 0.21 M EC^-; inspection of the structure indicates the presence of aggregates containing one or two EC^- molecules as well as Li^+ cations and PF_6^- anions. To more quantitatively evaluate the structure across all concentrations

considered, pair correlation functions (PCFs, g(r)) are shown in Figure 6.2 for C_C-C_C interactions [(a)] between EC^- molecules and C_C-Li^+ interactions [(b)] between EC^- molecules and the Li^+ cations.

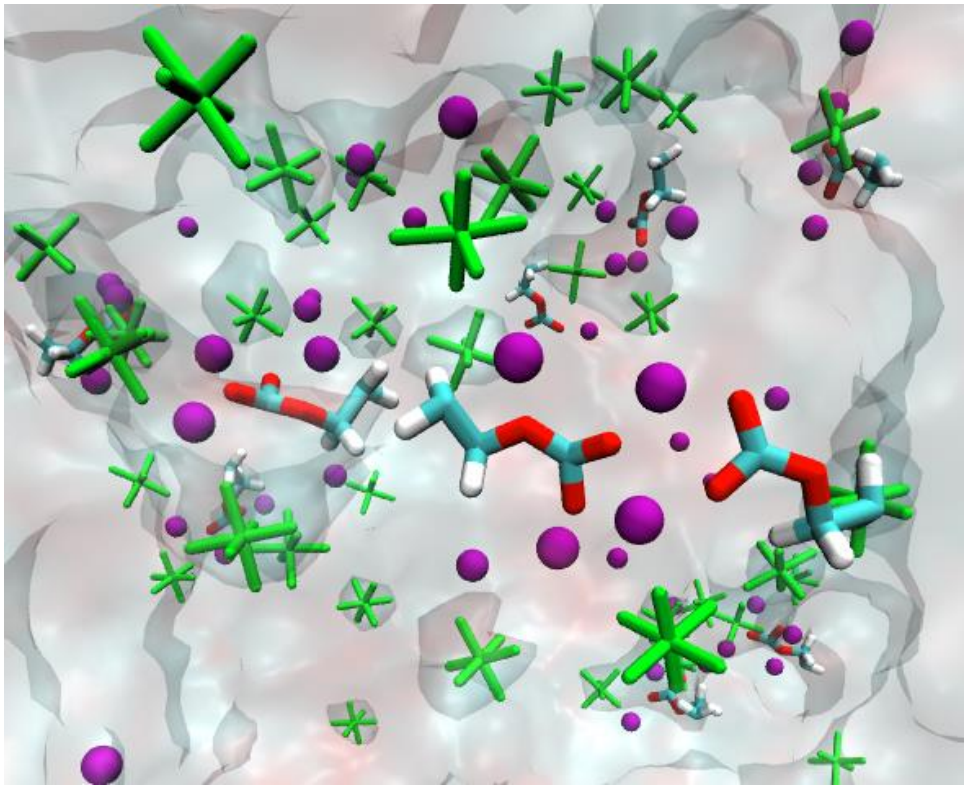

Figure 6.1. Snapshot of salt aggregation in a 1M $LiPF_6$ in 50/50 EC/DMC electrolyte with 0.21 M Li^+/EC^- added.

In [(a)], first nearest-neighbor peaks in g(r) located at r ≈ 5 Å correspond to formation of aggregates of two or more EC^- such as the dimer shown in Figure 6.1, where the carbonate groups are bridged by Li^+ cations. Whereas, the absence of such a peak indicates that all EC^- anions remain isolated from one another, separated by at least one solvation shell. No peaks can be seen for 0.04 and 0.11 M EC^- within 10 Å, which indicates that the radical anions are well-dispersed at these low concentrations. However,

at 0.17 and 0.21 M, a pronounced peak can be seen at r ≈ 5 Å, indicating their aggregation. Additionally, the broad second nearest-neighbor features at r > 7.5 Å suggest non-interacting pairs separated by one or more electrolyte layers exist at these concentrations. At 0.26 and 0.32 M, the first peak increases in magnitude and becomes thinner, indicating a stronger interaction. The absence of any second nearest-neighbor feature, however, suggests the aggregates are now isolated from each other and from any isolated EC^- anions. Finally, at 0.52 M the first peak becomes broad and exhibits two maxima indicating a larger cluster size, due to less specific C_C-C_C interactions.

In contrast to the C_C-C_C g(r), that of the C_C-Li^+ interaction shown in [(b)] does not change considerably with EC^- concentration. At each concentration a split, nearly symmetric peak can be seen around r = 2.5-3.5 Å. The inner maximum corresponds to a Li^+ cation sitting at the vertex of the angle between two O atoms in the carbonate group, while the outer maximum corresponds to Li^+ being solvated by a single O atom similar to the interaction between Li^+ and the carbonyl O of EC. The similarity between the EC^--Li^+ interaction of isolated EC^- and those in aggregates suggests that the aggregation may be

driven by competition between anions for a relatively lower concentration of Li^+ cations.

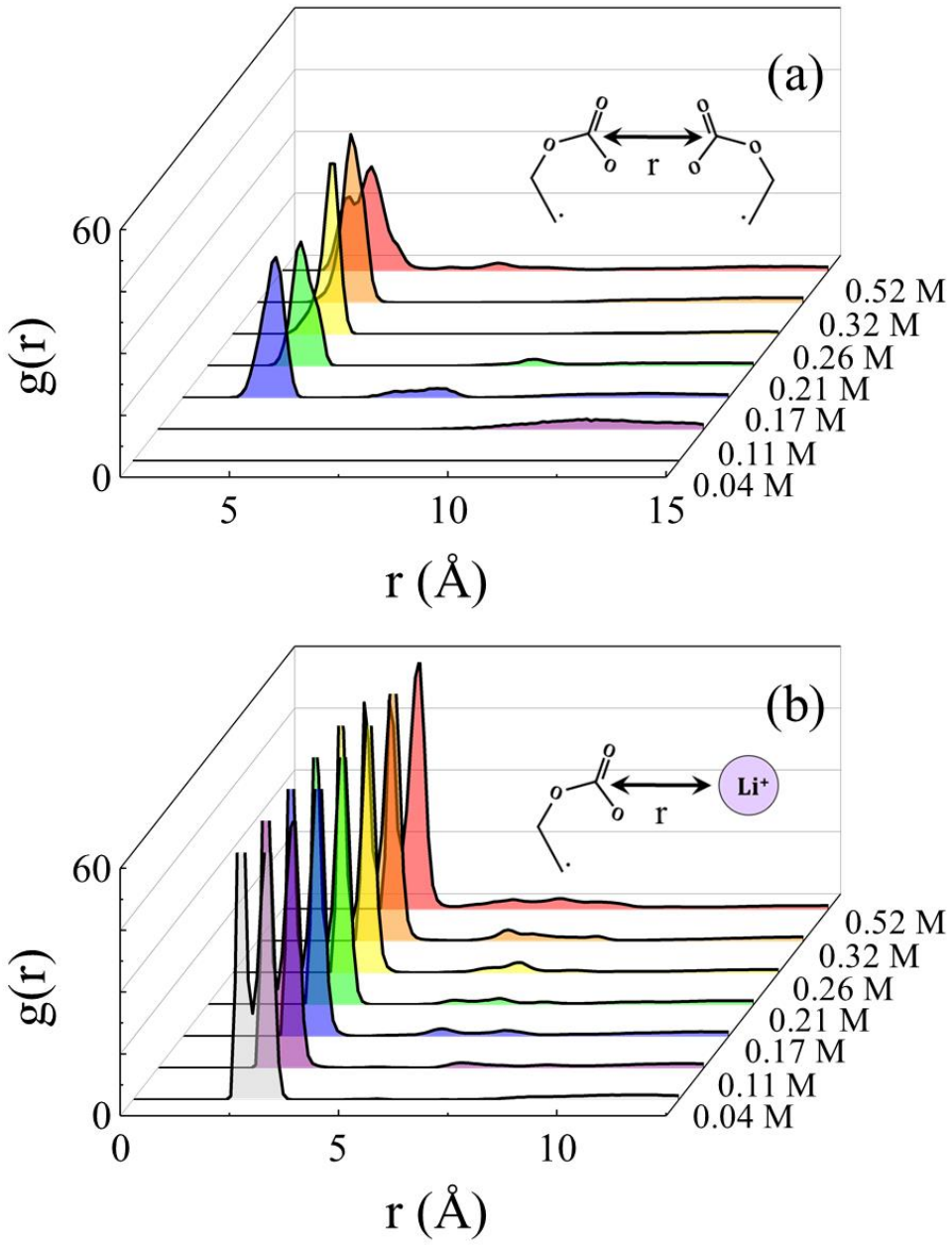

Figure 6.2. Pair correlation functions (g(r)) for EC^--EC^- pair interactions (a) based on the carbonate C atom (C_C) and EC^--Li^+ pair interactions (b) for EC^- concentrations from 0.04 to 0.52 M.

To better describe the formation of aggregates, a clustering analysis was performed based on the C_C-C_C distance between EC^- molecules with a cutoff distance of 5.4 Å based on Figure 6.2(a). The total percentage of EC^- anions which can be found within an aggregate of a given size at each concentration is shown in Figure 6.3. As can be expected, at 0.4 and 0.11 M EC^-, all of the EC^- molecules are isolated over the entire simulation trajectory. At 0.17 and 0.21 M greater than 50% of the EC^- molecules are isolated while the remainder form dimers and trimers. By comparison, at 0.26 and 0.32 M a majority of EC^- anions form dimers and trimers which explains the sudden increase in peak size between the two sets of concentrations in Figure 6.2(a). Finally, at 0.52 M higher order aggregates containing 4-6 EC^- anions appear leading to the splitting of the first peak in Figure 6.2(a).

From the equilibrium configurations, it is observed that for concentrations less than 0.52 M, EC^- primarily exists as isolated molecules, dimers, and trimers. To further evaluate the favorability of each, clusters were extracted from CMD simulations and relaxed through quantum mechanical calculations in implicit solvent. The ground state structures for the isolated EC^- (a), dimer (b), and trimer (c) are shown in Figure 6.4. Relative to the isolated EC^-, both the dimer and the trimer have a free energy of formation (ΔG) of about -0.29 eV per cluster, indicating that both are equally favorable considering thermodynamics alone and that both are more favorable than the requisite number of isolated EC^- anions.

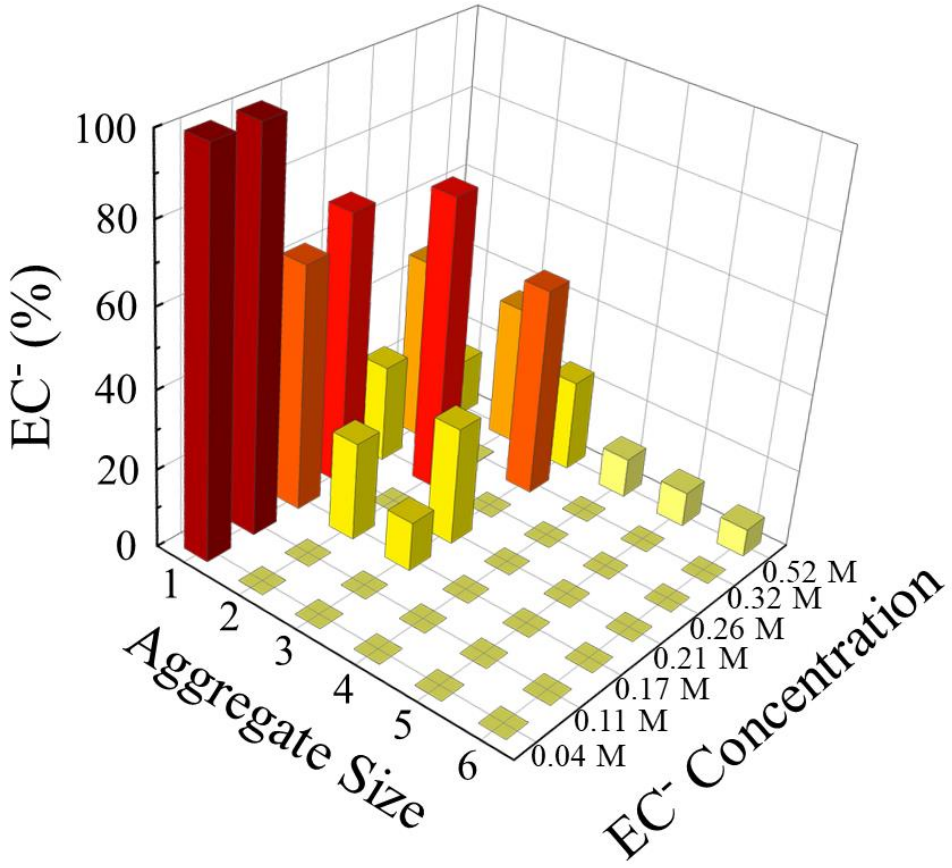

Figure 6.3. EC^- population by aggregate size within CMD simulations for EC^- concentrations from 0.04 to 0.52 M.

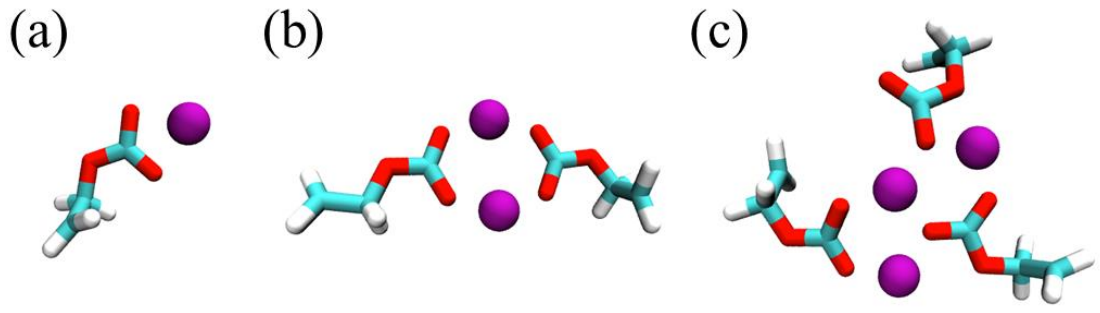

Figure 6.4. Ground state configurations from quantum mechanical calculations for isolated EC^- (a), dimer (b), and timer (c) configurations of Li^+/EC^-.

To further explore the concentration dependence on EC^- aggregation, well-tempered metadynamics simulations were performed to construct relative Helmhotz free energy profiles ($\Delta A(d)$) along the distance (d) between C_C atoms of two EC^- molecules. Figure 6.4 shows the $\Delta A(d)$ for four different concentrations (0.04, 0.11, 0.32, and 0.52 M) of Li^+/EC^-. Based on the equilibrium structure in Figure 6.2(a), the two biased EC^- anions can be described as an aggregate when $d \approx 5$ Å and as separated when $d > 7.5$ Å. The change in ΔA to form an aggregate (ΔA_{agg}) at 0.04 and 0.11 M is shown to be positive, while ΔA_{agg} is negative at 0.32 and 0.52 M. Furthermore, for the latter case ΔA appears to continuously decrease as d decreases, thus suggesting there would be no kinetic trap preventing aggregation at these concentrations. The change in sign of ΔA_{agg} with concentration suggests that the lack of aggregation at low concentrations is not the result of poor kinetics, but rather the existence of a critical concentration at which the assembly of EC^- into dimers and higher order aggregates becomes favorable. This transition is likely the result of competition between isolated EC^- molecules for Li^+ cations resulting in local depletion such that the EC^- anions may only be fully solvated by sharing Li^+ through the bridging interactions which result in dimerization.

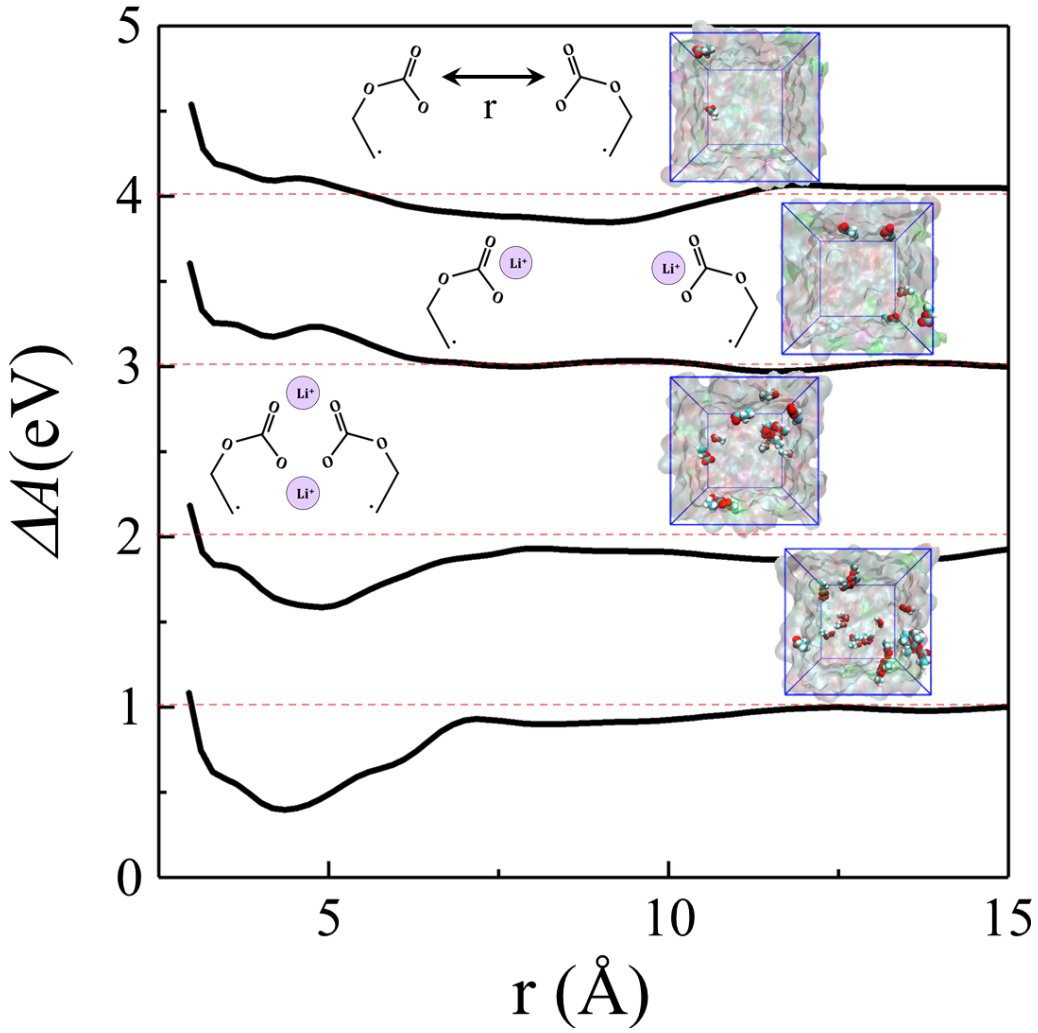

Figure 6.5. Relative Helmholtz free energy (ΔA) profiles for the radial distance between carbonate C atoms of two EC^- anions (r) for EC^- concentrations of 0.04, 0.11, 0.32, and 0.52 M (top to bottom). Schematics in the inset indicate the isolated or dimer nature of the interaction based on r and snapshots in the inset show the distribution of EC^- anions in the simulation box.

This finding suggests that at low concentrations of EC^-, bimolecular reactions would not occur as the well-solvated anions would remain isolated and not interact. Furthermore, the mediation of interactions by the two carbonate groups bridged by Li^+ cations suggests that reactions may pass through dimer or other aggregate structures as an

intermediate once the local concentration is large enough for such a structure to become favorable.

6.3.2 Accumulation and Aggregation of Reduced EC near Graphite Electrodes

In order to evaluate the concentration dependence on EC^- aggregation near a graphite electrode during SEI formation, MD/MC simulations were carried out for 1M $LiPF_6$ in 50/50 EC/DMC and 1M $LiPF_6$ in 25/75 EC/DMC electrolytes near graphite electrodes with surface charge densities of σ = -9.7 $\mu C/cm^2$ or approximately 1.2 V *vs.* Li/Li^+, as shown in Chapter 3. Figure 6.6 shows the number of isolated EC^- anions as a function of the number of EC^- molecules (which is equivalent to the number of MD/MC cycles) for the 50/50 [(a)] and 25/75 [(b)] systems, respectively, for three different values of τ . In the 50/50 system, the number of isolated EC^- initially increases rapidly for all τ up until about 25 EC^- have been added, then the amount of isolated EC^- nearly levels off to a saturation point of about 20 isolated radical anions. While the effect of τ is subtle, it appears as though longer relaxation time results in fewer isolated EC^-. By contrast, in the 25/57 system, the number of isolated EC^- steadily increases over all 150 MD/MC cycles. Here, the effect of τ is more pronounced as there is offset between τ = 500 ps and τ = 100 or 20 ps. Overall, it appears as though lower rates of electron transfer would promote the formation of EC^- aggregates allowing for the formation of alkyl carbonates and by hindering the lifetime of the more mobile intermediate, possibly reduce the irreversible capacity loss during the formation of the SEI.

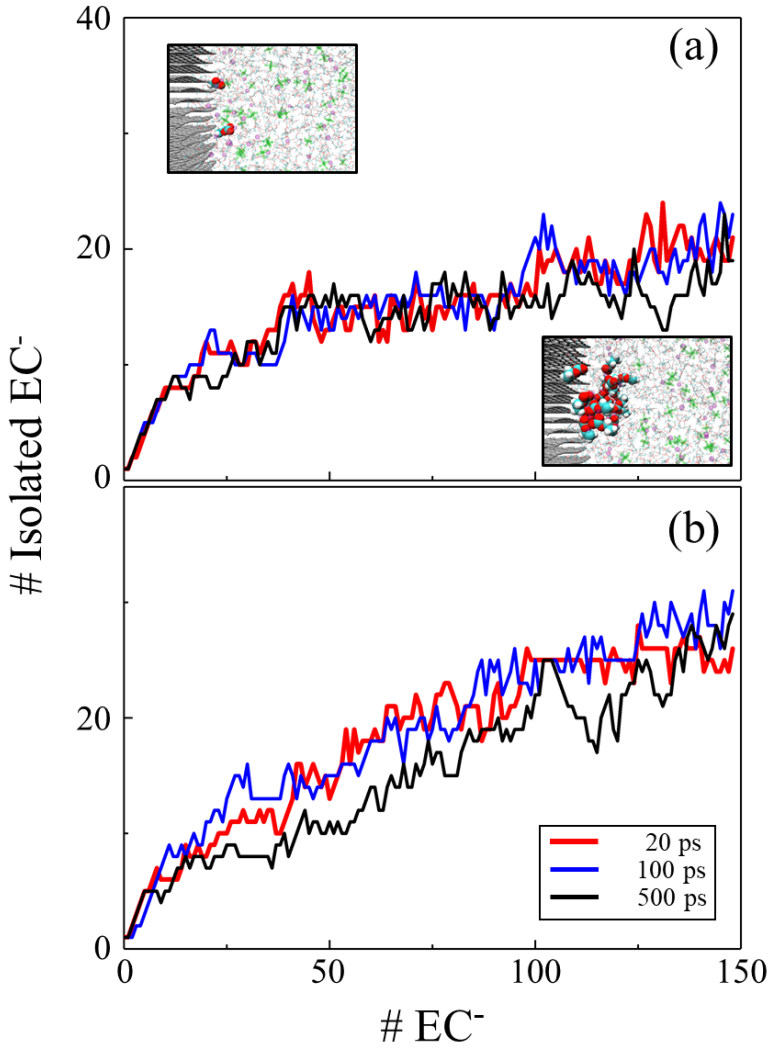

Figure 6.6. The number of isolated EC^- (defined as having no carbonate group pair distance less than a cutoff of 5.4 Å) against number of EC^- molecules from MD/MC simulations conducted with a 1M $LiPF_6$ in 50/50 EC/DMC electrolyte (a) and a 1M $LiPF_6$ in 25/75 EC/DMC electrolyte (b) for relaxation times τ = 20 (red), 100 (blue), and 500 ps (black). Snapshots in the inset of (a) show EC^- distribution for 5 and 25 EC^- molecules.

The diffusion of EC^- near the interface can be directly observed through the time-dependent interfacial structure evolved over the MD/MC simulation. Figure 6.7 shows the evolution of EC^- number density (ρ_n) along the axis perpendicular to the electrode surface

(z) with increasing MD/MC cycles for τ = 20 and 100 ps. In both electrolytes, it can be seen that the shorter τ results in nonzero EC^- ρ_n at larger z as well as larger ρ_n at larger z. In comparison, the 25/75 electrolyte exhibits more significant EC^- diffusion away from the electrode relative to the 50/50 electrolyte. The interfacial structure after 150 MD/MC cycles is visualized in the inset of each plot to demonstrate the EC^- distributions in all three spatial dimensions; it can be seen that in the 50/50 electrolyte EC^- anions pack more densely near the interface than in the 25/75 electrolyte where they are more diffuse, which is consistent with the findings presented in Chapter 5. Additionally, it is shown that shorter relaxation times (which represents higher currents) result in more significant diffusion, and potentially loss, of EC^- as the anions are unable to form more stable complexes/configurations which may mitigate electrostatic repulsion from the electrode or other anions.

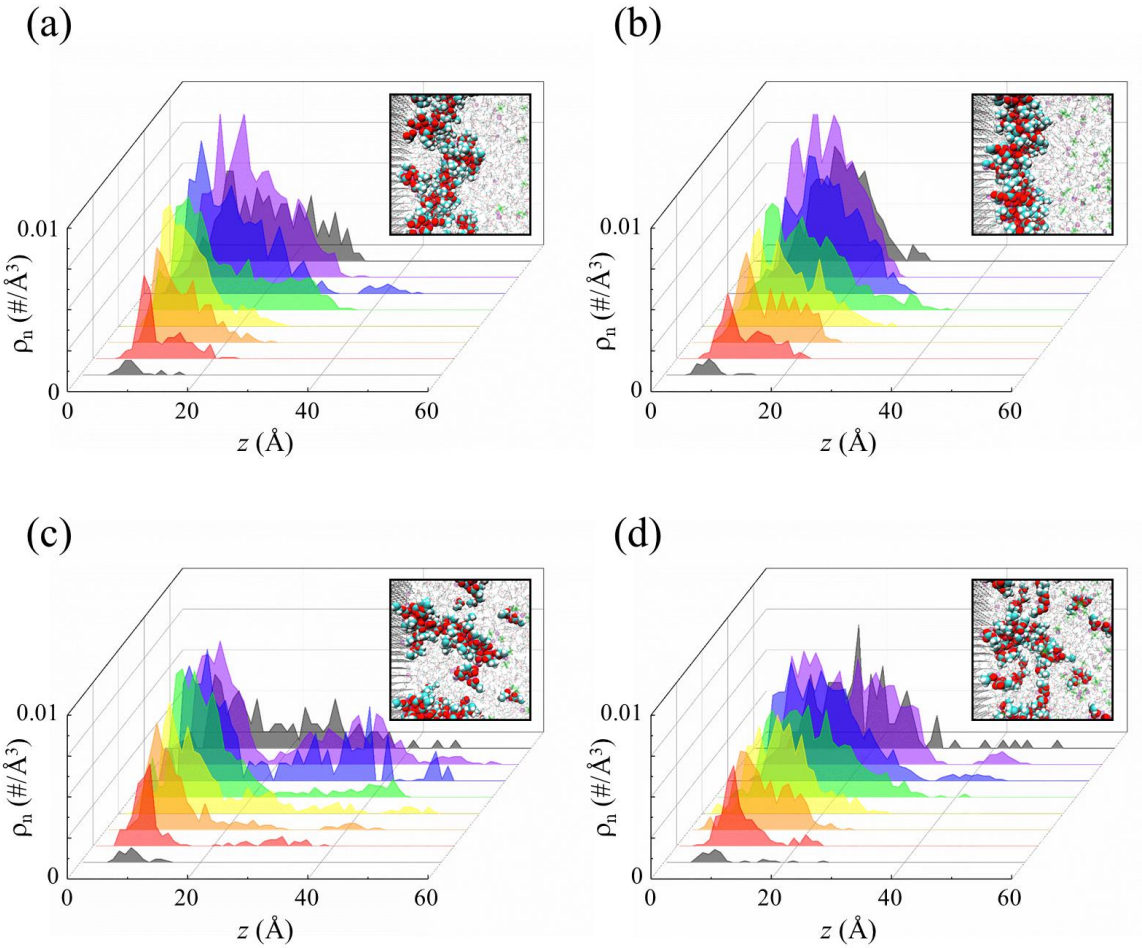

Figure 6.7. Time evolution of EC^- number density (ρ_n) along the direction perpendicular to the graphite electrode surface (z) from MD/MC simulations conducted for 150 cycles with a 1M $LiPF_6$ in 50/50 EC/DMC electrolyte and relaxation time τ = 20 (a) and 100 ps (b) as well as for a 1M $LiPF_6$ in 25/75 EC/DMC electrolyte and relaxation time τ = 20 (c) and 100 ps (d). Snapshots of the interface after the 150th cycle are shown in the inset of each figure with the EC^- molecules highlighted.

6.3.3 Dimer-mediated Bimolecular Combination Reactions

While CMD simulations show that EC^- molecules may readily interact to form dimers, trimers, and (if local concentrations become large) higher order aggregates so long as a critical local concentration is surpassed, AIMD simulations are required to study the

formation of chemical bonds. To investigate how EC^- molecules undergo bimolecular combination within aggregates, the ground state dimer structure from Figure 6.4 was taken as a model aggregate and solvated for use in CPMD simulations coupled with metadynamics. Figure 6.8 shows minimum free energy pathways (MFEPs) identified for the formation of Li_2BDC [(a)] and Li_2EDC [(b)] from a stable $2Li^+/2EC^-$ dimer configuration in 50/50 EC/DMC. The free energy profiles (ΔA) along the reaction coordinates (d_{rxn}) were computed using CPMD metadynamics; note that in both cases the reaction proceeds from right to left along d_{rxn}, as illustrated. For [(a)], the ΔA is somewhat flat from d_{rxn} = 8 – 4.5 Å with a local maximum at d_{rxn} = 5.5 Å before increasing steadily to a maximum at d_{rxn} = 2.8 Å (corresponding to the transition state) and a deep well at d_{rxn} = 1.65 Å (corresponding to the stable Li_2BDC structure). In order to traverse the transition state, a free energy barrier ($\Delta A^{\ddagger}$) of 0.69 eV must be overcome while the change in ΔA ($\Delta\Delta A$) is approximately -2.6 eV. In comparison, in [(b)] ΔA steadily decreases with d_{rxn} until a pronounced minimum is reached at d_{rxn} = 3 - 4 Å. ΔA then sharply increases to a maximum at d_{rxn} = 2.4 Å (corresponding to the transition state) before leading to a deep well at d_{rxn} = 1.6 Å (corresponding to the stable Li_2EDC structure). In order to traverse the transition state, a $\Delta A^{\ddagger}$ of 0.4 eV must be overcome while the $\Delta\Delta A$ is approximately -2.1 eV. By direct comparison, it can be seen that BDC^{2-} would be more thermodynamically favorable, however, the nearly 0.3 eV larger barrier would significantly restrict the rate of its formation relative to EDC^{2-}.

It should also be carefully noted that only one distance is biased in each simulation. While the minima do not occur at the same values of d_{rxn} in [(a)] and [(b)], the low energy configuration may be confirmed through comparison of the floating variables. For example, in [(a)] at for the configuration shown in the inset where d_{rxn} = 4.6 Å, one C_E atom is 4.5 Å from one of the reactive O_C atoms on the other EC^- anion; this distance corresponds to the minimum in d_{rxn} in [(b)]. Similarly, for the configuration shown in the inset of [(b)] where d_{rxn} = 3.2 Å, the distance between C_E atoms is 7.1 Å corresponding to a local minimum in d_{rxn} in [(a)].

To explore the effect of chemical environment on the reaction energetics, the reactions were also evaluated in pure EC. The calculated ΔA profiles for the formation of BDC^{2-} and EDC^{2-} in pure EC and EC/DMC are compared in Figure 6.9. It can be seen that both $\Delta A^{\ddagger}$ become larger in pure EC relative to EC/DMC. Along the BDC^{2-} pathway, the minimum around d_{rxn} = 4.5 Å disappears and instead the ΔA gradually increases as d_{rxn} decreases until the transition state at d_{rxn} = 2.65 Å. In addition to the larger $\Delta A^{\ddagger}$ (≈ 1.5 eV), the shape of the profile suggests that the formation of BDC^{2-} would be extremely sluggish. Along the EDC^{2-} pathway, the same pronounced minimum occurs between d_{rxn} = 3 - 4 Å indicating the stable intermediate configuration may occur within both solvation environments. However, the barrier increases to $\Delta A^{\ddagger} \approx 0.7$ eV in pure EC which, although still lower than that of BDC^{2-} formation, suggests the formation of EDC^{2-} is slow and would result in relatively long-lived intermediate states in pure EC.

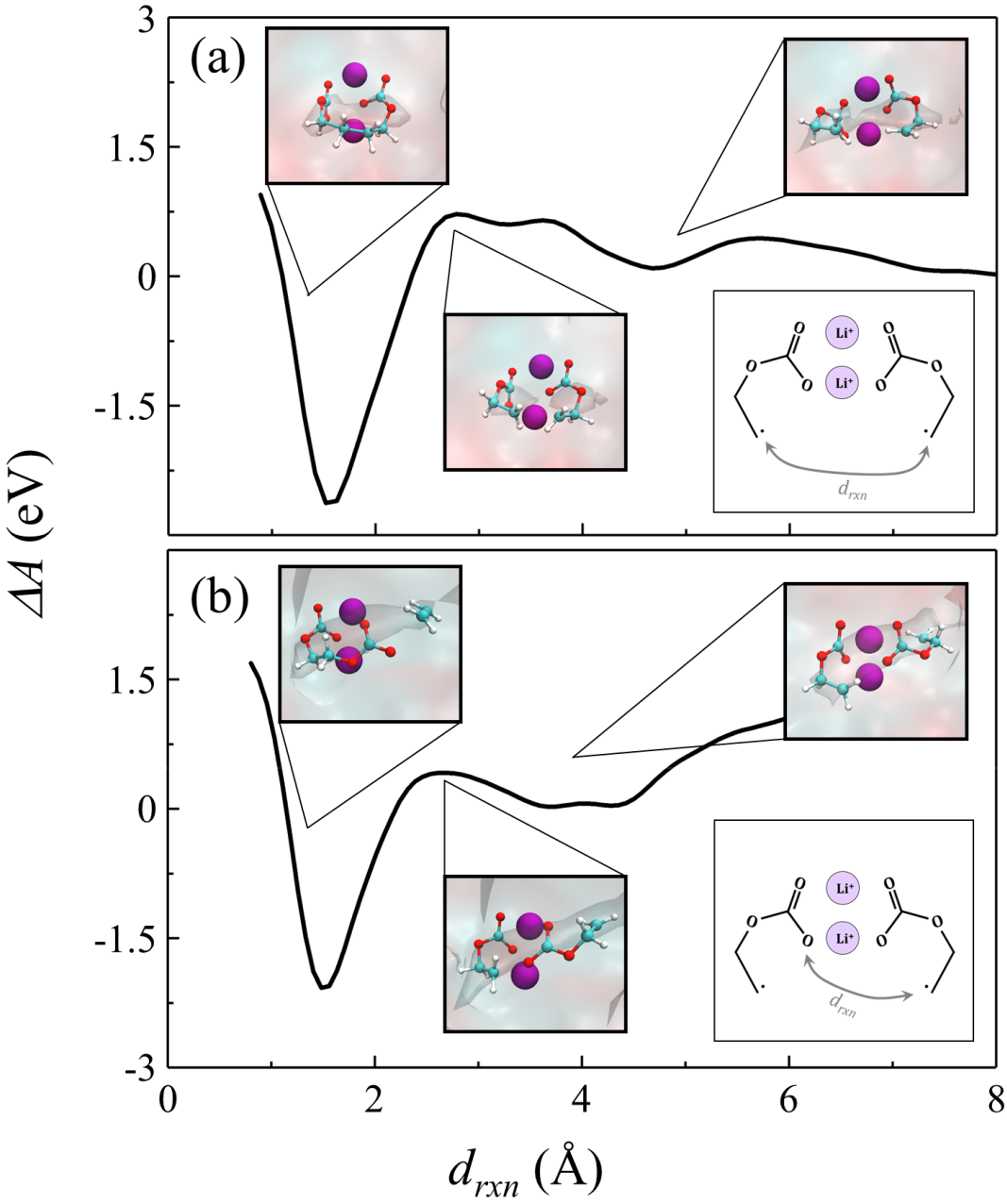

Figure 6.8. Minimum free energy (ΔA) pathways for BDC^{2-} (a) and EDC^{2-} (b) formation in 50/50 EC/DMC from a $2Li^{+}/2EC^{-}$ dimer. Snapshots of selected configurations corresponding to ΔA minima and maxima are shown.

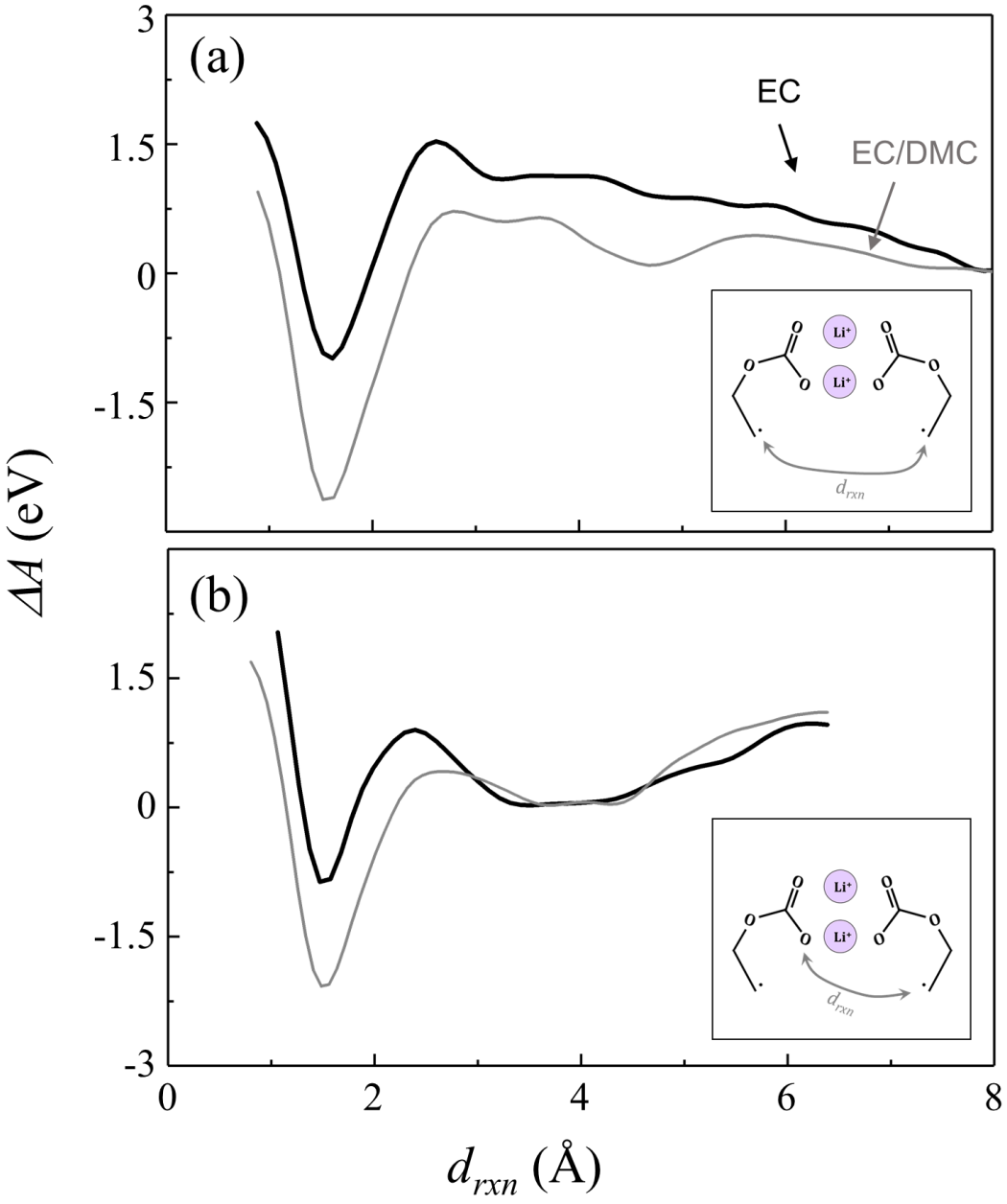

Figure 6.9. Minimum free energy (ΔA) pathways for BDC^{2-} (a) and EDC^{2-} (b) formation in 50/50 EC/DMC (grey) and pure EC (black) from $2Li^{+}/2EC^{-}$ dimer.

6.3.4 Origins of Solvent Effect and Li_2EDC Selectivity

To better understand the origin of the lower barrier for EDC^{2-} formation relative to BDC^{2-}, the molecular structure and electronic states of the C_E atoms participating in these reactions were carefully evaluated for the configurations shown in Figure 6.8 corresponding to minima and maxima in ΔA. These configurations along with the maximally localized Wannier function of the unpaired electron localized on the reacting C_E atom(s) are shown in Figure 6.10; only EC and DMC molecules solvating the Li^+ cations are shown. In both [(a)] and [(b)], both Li^+ cations are tetrahedrally coordinated by O atoms with one solvated by an O_C atom from each EC^- anion and two solvent molecules, and the other by both O_C atoms of a single EC^-, one O_C atom from the other, and a single solvent molecule. A similar configuration can be seen in [(c)] and [(d)], except one solvent molecule is replaced by the C_E atom which forms the C-O bond along the EDC^{2-} pathway.

While this analysis demonstrates the apparent role of Li^+, a quantitative relationship between $\Delta A^{\ddagger}$ and its interactions with O_C and C_E can be obtained through inspection of the simulation trajectory prior to formation of the final product. Figure 6.11 shows the probability density functions (PDFs) for the O_C–Li^+, C_E-Li^+, and d_{rxn} of the opposite reaction distances during the course of the formation of Li_2BDC [(a) in EC/DMC and (b) in pure EC] and EDC^{2-} [(c) in EC/DMC and (d) in pure EC]; the PDFs were constructed from selected frames along the corresponding reaction coordinate where 2.5 Å < d_{rxn} < 4.5 Å. The C_E-Li^+ PDFs in [(a)] exhibit a peak at $d \approx 3.5$ for one C_E and another at $d \approx 4.4$ Å the other. The former case represents a C_E atom weakly interacting with one Li^+ while the

latter suggests a lack of specific interaction between the C_E atom and either Li^+ cation. The C_E-O_C peak spans from 3.5 to 4.5 Å, indicating the entire trajectory occurs within the free energy well along the EDC^{2-} path. Similarly, both C_E-Li^+ pair distances in [(b)] exhibit peaks spanning from $d \approx 4$ Å while the C_E-Li^+ pair distance spans from 3 to 4.5 Å. The shifting of the first C_E-Li^+ PDF to greater distances indicates weaker interaction between the C_E atoms and Li^+. This is likely the result of stronger relative interaction between the surrounding solvent molecules and Li^+ due to the absence of DMC which has been shown to bind to Li^+ less strongly than EC[154].

The O_C-Li^+ PDF in [(c)] exhibits a large pronounced peak at $d \approx 2.0$ Å, while that of the C_E-Li^+ pair distance exhibits a sharp peak at $d \approx 2.3$ with a tail spanning to 4 Å. The C_E-C_E peak spans from 6.7 to 8.5 Å, which suggests that the BDC^{2-} reaction could not occur from this configuration without considerable rearrangement. By contrast, the O_C-Li^+ PDF in [(d)] exhibits a similar large pronounced peak at $d \approx 2.1$Å while the C_E-Li^+ PDF exhibits a broad, asymmetric peak centered at $d \approx 3.9$ Å and spans from 2.9 to 5 Å. Here, the shifting of the interactions to greater distances suggests that both C_E and O_E interact less strongly with Li^+, which again is to be expected in the higher dielectric medium of pure EC. In particular, the disappearance of the pronounced C_E-Li^+ peak at $d \approx 2.4$ Å indicates that the Li^+ cation is no longer solvated by C_E and instead by an additional EC molecule. This outcompeting of C_E for the solvation of Li^+ by solvent molecules in pure EC may contribute to the observed increase in $\Delta A^{\ddagger}$ relative to EC/DMC where the cation is able to better mediate the reaction through stabilizing the transition state where the

electronegative C_E and O_C atoms would experience the greatest electrostatic repulsion. Again, the C_E-C_E peak is broad located beyond 5 Å indicating BDC^{2-} could not form without significant reorganization of one or both EC^- molecules.

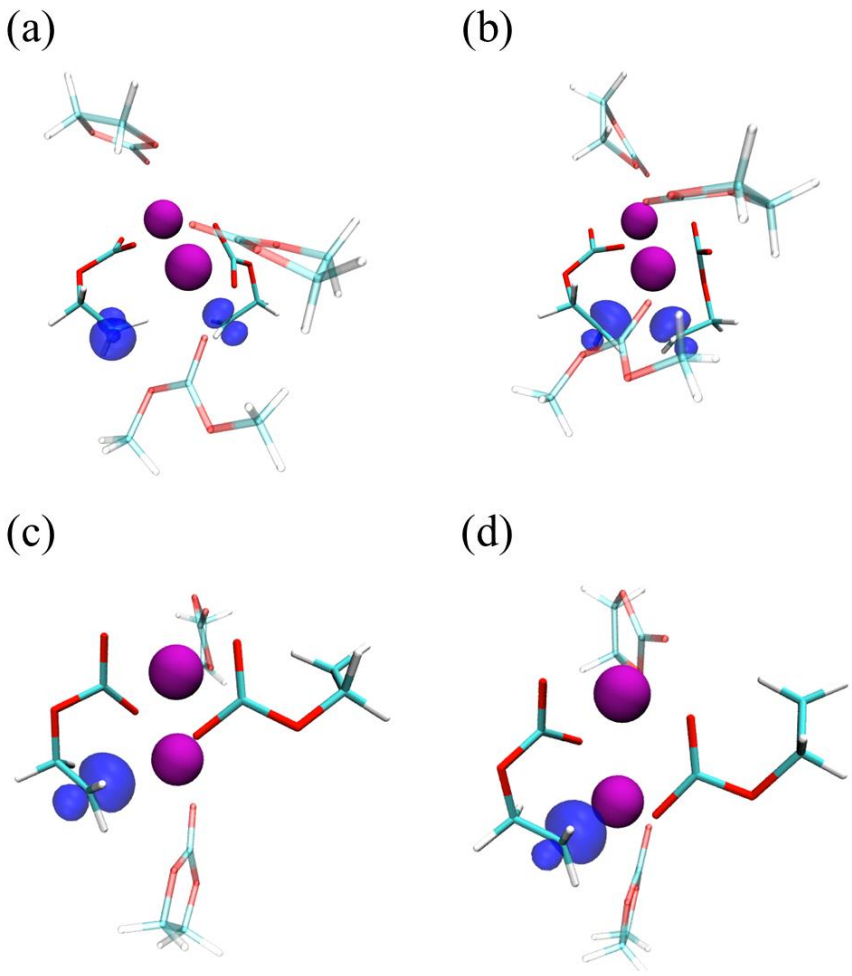

Figure 6.10. Snapshots of the minimum free energy (a) and maximum free energy (b) configurations taken from metadynamics trajectory along the BDC^{2-} formation pathway. The same are shown for the EDC^{2-} formation pathway in (c) and (d), respectively. Solvent molecules which participate in the Li^+ cation primary solvation sheath and maximally localized Wannier functions of the unpaired electron localized on C_E atoms participating in bond formation are shown.

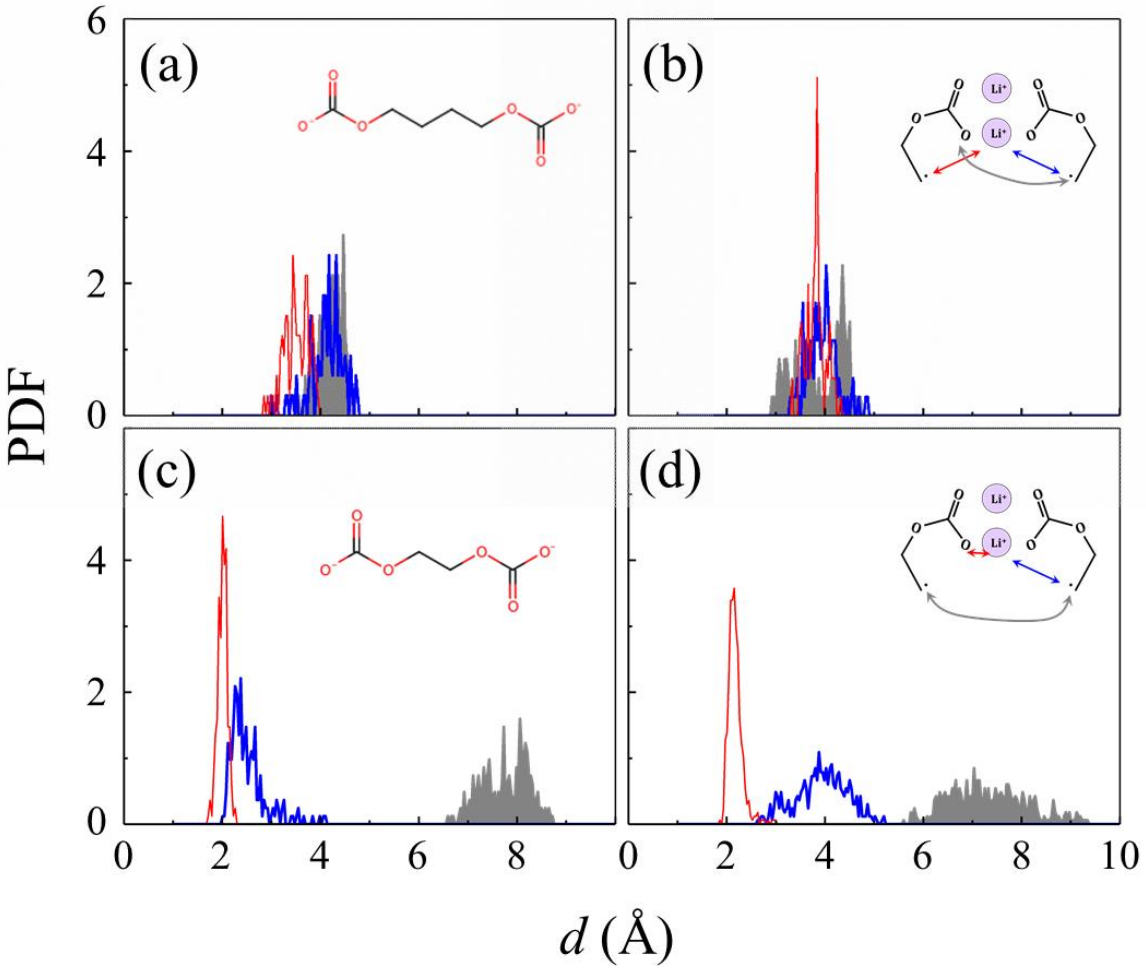

Figure 6.11. Probability density functions (PDFs) of the minimum Li-C_E (red and blue) and C_E-O_C (grey) pair distances for BDC^{2-} formation in 50/50 EC/DMC (a) and pure EC (b) and Li-O_C (red), Li-C_E (blue), and C_E-C_E (grey) pair distances for EDC^{2-} formation in EC/DMC (c) and pure EC (d). Schematics in the insets indicate which product is formed and which interaction distances are shown.

For both the BDC^{2-} and EDC^{2-}, it is shown that the reactive C_E group interacts more strongly with a Li^+ cation in EC/DMC than in pure EC. However, along the BDC^{2-} pathway one C_E atom tends to not interact strongly with either Li^+ cation in either solvent. In addition to this reduction in mediation effect, the increased viscosity in pure EC also likely affects the $\Delta A^{\ddagger}$ of BDC^{2-} formation due to the larger distance the C_E atoms must traverse.

Furthermore, while the BDC^{2-} reaction must pass through the minimum configuration adjacent to the transition state of EDC^{2-} formation, the same is not true of the opposite reaction. For this reason, more configurations are likely to result in EDC^{2-} formation than BDC^{2-} formation even if the $\Delta A^{\ddagger}$s are equivalent. However, the lower barrier for EDC^{2-} in both solvent systems indicates a strong kinetic selectivity towards its formation during the early stages of SEI formation where EC^{-} concentrations are low, yet not so low that dimers do not form in solution. Finally, while the trimer configuration was not explicitly evaluated here, the excess strain imposed by the third EC^{-} anion can be expected to reduce the barrier to EDC^{2-} formation if it has any effect at all as the initial C_E-O_C distances are shorter.

6.4 SUMMARY

The composition of the SEI has been the subject of much debate in the literature even after considerable efforts to determine the predominant reduction product of EC which allows for stable cycling of graphite anodes through both experiments and simulations. While the complexity of the chemical environment create challenges for spectroscopic analysis, molecular simulations are able to explore controlled systems to gain fundamental insights into the underlying processes which make up the SEI formation process. However, oversimplification or improper modeling of the environment may lead to misunderstanding of reactions.

In this chapter, it is demonstrated through CMD simulations that EC^{-} can be stabilized in solution through strong interactions with Li^{+} cations, which would in turn

hinder the formation of alkyl carbonates like EDC^{2-} or BDC^{2-} through bimolecular reactions. However, once a critical concentration of EC^{-} is reached, competition between carbonate groups for Li^{+} cations will result in the formation of dimer and trimer structures wherein a single Li^{+} cation is solvated by O atoms from two EC^{-} molecules, thus bridging the electronegative groups. Clustering analysis showed that at concentrations below about 0.5 M EC^{-}, only dimers and timers form, but above this concentration larger aggregates begin to form if no chemical reactions between EC^{-} anions occur. The formation of these aggregates is demonstrated to result from a shift in thermodynamic favorability through metadynamics simulations. MD/MC simulations showed that near graphite electrodes, diffusion traps allow for the local concentration to increase rapidly with EC^{-} generation. This effect is shown to be enhanced by slower electron transfer rate and by using a more EC-rich solvent.

The bimolecular reaction energetics were then demonstrated based on the dimer structures obtained by CMD simulations using CPMD and metadynamics. While BDC^{2-} formation was shown to be more thermodynamically favorable in the solution phase (in agreement with gas phase calculations), a significant $\Delta A^{\ddagger}$ must be overcome due to electrostatic repulsion between the two electronegative C_E atoms which form the C-C bond. By contrast, the barrier for EDC^{2-} formation is nearly half that of BDC^{2-} due to mediation of the bond formation between O_C and C_E by a Li^{+} cation which mitigates electrostatic repulsion. Furthermore, both reactions are shown to have reduced $\Delta A^{\ddagger}$ in EC/DMC rather than pure EC which is likely both due to stronger solvent – Li^{+} interactions as well as

increased viscosity. These findings indicate EDC^{2-} would likely be the dominant product of EC^{-} bimolecular combination due to kinetic selectivity.

The effects of DMC and Li^{+} cations demonstrated in this chapter further highlight the importance of explicit consideration of solvent in the simulation of chemical reactions which contribute to the formation of the SEI. While Li^{+} is essential to lithium ion battery operation as a charge carrier, it also serves as a catalyst to enhance the formation of SEI products which are able to then stabilize the anode. Similarly, DMC contributes to battery performance beyond simply enhancing the ionic conductivity through reduction of electrolyte viscosity. The secondary roles of these species further demonstrates the benefit of improved fundamental understanding of the chemistry within batteries obtained by molecular simulations.

Chapter 7 : Summary and Future Directions

7.1 SUMMARY

This dissertation outlines a computational framework utilizing classical and *ab initio* molecular dynamics simulations augmented with enhanced sampling techniques like metadynamics to study the reductive decomposition of electrolyte at the anode/electrolyte interface resulting in the formation of the solid electrolyte interphase (SEI) in lithium ion batteries (LIBs). Due to the size- and time-scales at which the relevant phenomena occur, it us unfeasible to study the formation of the SEI at a level of theory capable of describing electron transfer and the breaking/forming of bonds. Instead, the approach taken reduces the system to a reaction/diffusion problem where the interfacial structure and transport processes occurring at the interface are modeling through classical molecular dynamics and the reactions are described through density function theory (DFT) and Car-Parrinello molecular dynamics (CPMD).

The model system discussed in this dissertation represents a highly oriented pyrolytic graphite (HOPG) anode immersed in a standard electrolyte composed of ethylene carbonate (EC), dimethyl carbonate (DMC), and $LiPF_6$. This system has been extensively studied through experiments and an abundance of data has been presented in the literature, yet a comprehensive description of the SEI formation process in this system remains elusive despite commercial use for over a decade. The complexity of the chemical environment as well as the sensitivity of the SEI to ambient conditions resulting in a challenging system for meticulous scientific exploration. However, by understanding the underlying processes which contribute to SEI formation including the interfacial structure prior to reduction, diffusion behavior of reduction intermediates/products near the

interface, and secondary reactions which result in the formation of new intermediates or final products, key descriptors may be identified which allow for engineering of the SEI. Some of the key findings discussed in this dissertation are outlined below:

Field-induced reorganization of electrolyte at the anode/electrolyte interface

When the graphite electrode is charge neutral, the solvent molecules reorganize at the interface based on van der Waals (vdW) interactions which results in the first solvent layer being richer in DMC relative to the bulk composition due to its comparatively bulky methyl groups interacting more strongly with the terminated graphite edges than the ethylene group of EC. The salt molecules, on the other hand, are excluded/depleted from/in the first few layers as they are better solvated in the bulk electrolyte than near the electrode. However, as the anode is polarized towards the lithium intercalation potential and the Fermi level rises, the filling of empty electronic states results in a negative excess surface charge density and an electric field which causes the electrolyte to reorganize. The competition between vdW and electrostatic interactions between the electrolyte and electrode leads to a continuous change in interfacial structure with applied potential as the first solvent layer becomes filled with EC molecules orienting their carbonyl O away from the interface. The uniform orientation of the EC molecules creates a charge layering effect which causes Li^+ cations to accumulate in the next layer. This continues until a critical field which can no longer be screened by the EC is reached. At this point, Li^+ cations will partially desolvate and move to the interface. Because of this, the interfacial structure is a function of not only the bulk electrolyte composition, but also the applied potential and both should be considered when studying the reductive decomposition of the electrolyte. In particular, the overrepresentation of EC due to its ability to efficiently screen the electric

field at negative applied potentials can explain why EC is primarily the reduced species even in mixed carbonate electrolytes containing majority acyclic carbonates.

Strong solvent effect on reduced EC ring-opening kinetics

Upon its reduction, EC initially exists in a ring configuration as c-EC^-. This intermediate may undergo homolytic ring-opening to form another intermediate, o-EC^-, which can then form alkyl carbonates such as ethylene dicarbonate or be reduced further to CO_3^{2-}. However, static DFT calculations based on implicit solvent molecules predict that c-EC^- is relatively stable due to a large ring-opening barrier across a range of solvent models. Even in explicit solvent composed of pure EC, the ring-opening barrier is fairly significant, possibly due to the geometric similarity between EC and c-EC^- as the latter maintains a ring-stacking structure and solvates Li^+ cations as if it were another solvent molecule. This symmetry, however, is disturbed by the inclusion of DMC as a cosolvent. This subsequently lowers the ring-opening barrier by greater than half as c-EC^- interacts more strongly with Li^+ cations in the presence of DMC. While in pure EC, c-EC^- must undergo significant structural reorganization around the Li^+ to traverse its transition state, in EC/DMC there are minimal differences in the Li^+ solvation structure between c-EC^- and the transition state configuration. From this result, it can be observed that the complexity of the chemical environment renders simple models, such as implicit solvent, insufficient to describe the chemical reaction kinetics which affect SEI formation. Furthermore, it highlights the role of DMC beyond simply reducing viscosity to promote ion diffusion. The ability of DMC to reduce the barrier of c-EC^- ring-opening may result in different reduction products altogether, or at least promotes the formation of products reducing the lifetime of monovalent intermediate species.

Near-interface diffusion of reduced EC

While the SEI has been studied extensively, the majority of attention has been paid to the chemical reactions and their kinetics/thermodynamics. Yet, as many reactions involve the anode as an electron source, the transport of species to/from the interface would also be a critical aspect of the overall reaction schema. In particular, once EC is reduced to c-EC^-, the competing rates between the reduction of c-EC^- by the anode, the ring-opening of c-EC^- to o-EC^-, and the diffusion of c-EC^- away from the interface will determine what product is formed. Furthermore, if ring-opening occurs rapidly, then the competing rates between o-EC^- reduction and diffusion away from the interface become the relevant comparison. While reduction rate will depend on factors such as charge rate during the SEI formation cycle and the electrode morphology, the diffusion behavior near the interface can qualitatively demonstrate how likely a species is to remain at the interface where it can be reduced. From metadynamics simulations, it is shown that both c-EC^- and o-EC^- do not need to overcome a significant increase in free energy to diffuse away from the interface and become fully solvated. However, o-EC^- is more likely to remain near the interface when compared to c-EC^- indicating that faster ring-opening kinetics will result in slower intermediate diffusion into the bulk where it may contribute to irreversible capacity fade. While it was demonstrated in more DMC-rich electrolytes some o-EC^- molecules may be trapped at the interface where they can be reduced to CO_3^{2-}, the predominant outcome appears to be diffusion of EC^- (before or after ring-opening) away from the electrode where it can then react to form a final product to be incorporated into the SEI.

Kinetic selectivity of ethylene dicarbonate formation

While alkyl carbonates are discussed in the literature as broad class of SEI-forming decomposition products, two alkyl carbonates have been identified as potential products of bimolecular combination of EC^-: ethylene dicarbonate (EDC^{2-}) and butylene dicarbonate (BDC^{2-}), with the former evolving C_2H_4 as a byproduct. EDC^{2-} forms by the formation of a C-O bond between one of the two carboxyl O atoms on one EC^- and the C atom of the radical CH_2 end group of another, while BDC^{2-} forms by the formation of a C-C bond between the C atoms of the radical CH_2 end groups of two EC^- molecules. While experimental papers largely claim EDC^{2-} as the primary alkyl carbonate, many theoretical papers have claimed BDC^{2-} to be more favorable. While the latter is true when considering thermodynamics alone, the reaction barrier for BDC^{2-} formation in carbonate solvents is almost twice that of EDC^{2-} formation. This occurs because of mediation by Li^+ cations which interact strongly with carboxyl O atoms. While the electrostatic repulsion between two electronegative atoms would result in high energy intermediate states, the interaction between the C and O atoms with Li^+ reduces the repulsion between them. Contrarily, during the formation of the C-C bond both C atoms are farther from the Li^+ cation than either atom involved in the formation of the C-O bond. Because of this difference in barriers, the predominant product is likely to be EDC^{2-} due to kinetics.

7.2 FUTURE DIRECTIONS

While the computational framework described in this dissertation was applied to the study of the early stages of SEI formation for a conventional EC/DMC electrolyte, it can be applied to the study of factors which may alter the early stages of SEI formation such as additives or built upon to evaluate later stages of SEI formation. In particular, this

work identifies interfacial structure at reducing potentials and intermediate transport as two key factors in the overall SEI formation process. While additives have been largely studied based on reduction potential, their distribution at interfaces and the mobility of their reduction products would potentially contribute to their efficacy or lack thereof at forming a more beneficial SEI layer than base electrolytes. Furthermore, the MD/MC method described in Chapter 6 may be expanded to describe reactions beyond EC reduction to explore how the SEI forms based on reaction free energy pathways discussed in this dissertation. Through this approach, the effects of variables such as temperature, applied voltage, and electron transfer rate may be correlated to SEI properties.

References

(1) Yoshino, A.; Sanechika, K.; Nakajima, T. Secondary Battery. US Patent 4,668,595, 1987.

(2) Yoshino, A. *Angew. Chemie - Int. Ed.* **2012**, *51* (24), 5798–5800.

(3) Whittingham, M. S. *Chem. Rev.* **2004**, *104* (10), 4271–4302.

(4) Goodenough, J. B.; Kim, Y. *Chem. Mater.* **2010**, *22* (3), 587–603.

(5) Goodenough, J. B.; Park, K.-S. S. *J. Am. Chem. Soc.* **2013**, *135* (4), 1167–1176.

(6) Armand, M.; Tarascon, J.-M. *Nature* **2008**, *451* (7179), 652–657.

(7) Scrosati, B.; Garche, J. *J. Power Sources* **2010**, *195* (9), 2419–2430.

(8) Winter, M.; Barnett, B.; Xu, K. *Chem. Rev.* **2018**, *118* (23), 11433–11456.

(9) Trigg, T.; Telleen, P.; Boyd, R.; Cuenot, F.; D'Ambrosio, D.; Gaghen, R.; Gagné, J. F.; Hardcastle, A.; Houssin, D.; Jones, A. R.; Kaneko, H. *Global EV Outlook: Understanding the Electric Vehicle Landscape to 2020*; 2013.

(10) Janek, J.; Zeier, W. G. *Nat. Energy* **2016**, *1* (9), 16141.

(11) Yazami, R.; Touzain, P. *J. Power Sources* **1983**, *9* (3), 365–371.

(12) Mizushima, K.; Jones, P. C.; Wiseman, P. J.; Goodenough, J. B. *Mater. Res. Bull.* **1980**, *15* (6), 783–789.

(13) Dey, A. N.; Sullivan, B. P. *J. Electrochem. Soc.* **1970**, *117* (2), 222.

(14) Besenhard, J. O. *Carbon N. Y.* **1976**, *14* (2), 111–115.

(15) Fong, R.; von Sacken, U.; Dahn, J. R. *J. Electrochem. Soc.* **1990**, *137* (7), 2009.

(16) Dahn, J. R. *Phys. Rev. B* **1991**, *44* (17), 9170–9177.

(17) Peled, E. *J. Electrochem. Soc.* **1979**, *126* (12), 2047–2051.

(18) Peled, E. *J. Electrochem. Soc.* **1997**, *144* (8), L208.

(19) Aurbach, D.; Ein-Eli, Y.; Markovsky, B.; Zaban, A. *J. Electrochem. Soc.* **1995**, *142* (9), 2882–2890.

(20) Aurbach, D.; Markovsky, B.; Weissman, I.; Levi, E.; Ein-Eli, Y. *Electrochim. Acta* **1999**, *45* (1), 67–86.

(21) Aurbach, D.; Levi, M. D.; Levi, E.; Schechter, A. *J. Phys. Chem. B* **1997**, *101* (12), 2195–2206.

(22) Aurbach, D. *Solid State Ionics* **2002**, *148* (3-4), 405–416.

(23) Xu, K. *Chem. Rev.* **2004**, *104* (10), 4303–4418.

(24) Xu, K.; von Cresce, A. *J. Mater. Chem.* **2011**, *21* (27), 9849.

(25) Xu, K. *Chem. Rev.* **2014**, *114* (23), 11503–11618.

(26) Yamada, Y.; Iriyama, Y.; Abe, T.; Ogumi, Z. *Langmuir* **2009**, *25* (21), 12766–12770.

(27) Jow, T. R.; Delp, S. A.; Allen, J. L.; Jones, J.-P.; Smart, M. C. *J. Electrochem. Soc.* **2018**, *165* (2), A361–A367.

(28) He, Y. B.; Li, B.; Yang, Q. H.; Du, H.; Kang, F.; Ling, G. W.; Tang, Z. Y. *J. Solid State Electrochem.* **2011**, *15* (9), 1977–1985.

(29) Zhang, Q.; Pan, J.; Lu, P.; Liu, Z.; Verbrugge, M. W.; Sheldon, B. W.; Cheng, Y. T.; Qi, Y.; Xiao, X. *Nano Lett.* **2016**, *16* (3), 2011–2016.

(30) Wang, D. Y.; Sinha, N. N.; Burns, J. C.; Aiken, C. P.; Petibon, R.; Dahn, J. R. *J. Electrochem. Soc.* **2014**, *161* (4), 467–472.

(31) Megahed, S.; Scrosati, B. *J. Power Sources* **1994**, *51* (1-2), 79–104.

(32) Rodrigues, M. T. F.; Sayed, F. N.; Gullapalli, H.; Ajayan, P. M. *J. Power Sources* **2018**, *381* (August 2017), 107–115.

(33) Petibon, R.; Henry, E. C.; Burns, J. C.; Sinha, N. N.; Dahn, J. R. *J. Electrochem. Soc.* **2013**, *161* (1), A66–A74.

(34) Kang, S. J.; Park, K.; Park, S. H.; Lee, H. *Electrochim. Acta* **2018**, *259*, 949–954.

(35) Leifer, N.; Smart, M. C.; Prakash, G. K. S.; Gonzalez, L.; Sanchez, L.; Smith, K. A.; Bhalla, P.; Grey, C. P.; Greenbaum, S. G. *J. Electrochem. Soc.* **2011**, *158* (5), A471–A480.

(36) Ma, L.; Xia, J.; Xia, X.; Dahn, J. R. *J. Electrochem. Soc.* **2014**, *161* (10), A1495–A1498.

(37) Edström, K.; Herstedt, M.; Abraham, D. P. *J. Power Sources* **2006**, *153* (2), 380–384.

(38) Nie, M.; Chalasani, D.; Abraham, D. P.; Chen, Y.; Bose, A.; Lucht, B. L. *J. Phys. Chem. C* **2013**, *117* (3), 1257–1267.

(39) Nie, M.; Abraham, D. P.; Seo, D. M.; Chen, Y.; Bose, A.; Lucht, B. L. *J. Phys. Chem. C* **2013**, *117* (48), 25381–25389.

(40) Zhang, X.; Kostecki, R.; Richardson, T. J.; Pugh, J. K.; Ross, P. N. *J. Electrochem. Soc.* **2001**, *148* (12), A1341–A1345.

(41) Shkrob, I. A.; Zhu, Y.; Marin, T. W.; Abraham, D. *J. Phys. Chem. C* **2013**, *117* (38), 19255–19269.

(42) Shkrob, I. A.; Zhu, Y.; Marin, T. W.; Abraham, D. *J. Phys. Chem. C* **2013**, *117* (38), 19270–19279.

(43) Boyer, M. J.; Hwang, G. S. *Curr. Opin. Chem. Eng.* **2016**, *13*, 75–81.

(44) Li, Y.; Leung, K.; Qi, Y. *Acc. Chem. Res.* **2016**, acs.accounts.6b00363.

(45) Bhatt, M. D.; O'Dwyer, C. *Phys. Chem. Chem. Phys.* **2015**, *17* (7), 4799–4844.

(46) Aurbach, D.; Markovsky, B.; Shechter, A.; Ein-Eli, Y.; Cohen, H. *J. Electrochem. Soc.* **1996**, *143* (12), 3809–3820.

(47) Spahr, M. E.; Palladino, T.; Wilhelm, H.; Würsig, A.; Goers, D.; Buqa, H.; Holzapfel, M.; Novák, P. *J. Electrochem. Soc.* **2004**, *151* (9), A1383–A1395.

(48) Xu, K.; Lam, Y.; Zhang, S. S.; Jow, T. R.; Curtis, T. B. *J. Phys. Chem. C* **2007**, *111* (20), 7411–7421.

(49) Born, M.; Oppenheimer, R. J. *Ann. Phys.* **1927**, *389* (20), 457–484.

(50) Kohn, W.; Sham, L. J. *Phys. Rev.* **1965**, *385* (1951).

(51) Ziegler, T. *Chem. Rev.* **1991**, *91* (5), 651–667.

(52) Parr, R. G.; Yang, W. *Annu. Rev. Phys. Chem.* **1995**, *46*, 701–728.

(53) Hohenberg, P.; Kohn, W. *Phys. Rev.* **1964**, *136* (3B), B864–B871.

(54) Case, D. A.; Wang, J. M.; Wolf, R. M.; Caldwell, J. W.; Kollman, P. A. *J. Comput. Chem.* **2004**, *25* (9), 1157–1174.

(55) Jorgensen, W. L.; Maxwell, D. S.; Tirado-Rives, J. *J. Am. Chem. Soc.* **1996**, *118* (45), 11225–11236.

(56) Feynman, R. P. *Phys. Rev.* **1939**, *56* (4), 340–343.

(57) Verlet, L. *Phys. Rev.* **1967**, *159* (1), 98–103.

(58) Nosé, S. *J. Chem. Phys.* **1984**, *81* (1), 511–519.

(59) Hoover, W. G. *Phys. Rev. A* **1985**, *31* (3), 1695–1697.

(60) Martyna, G. J.; Klein, M. L.; Tuckerman, M. *J. Chem. Phys.* **1992**, *97* (4), 2635–2643.

(61) Kirkwood, J. G. *J. Chem. Phys.* **1935**, *3* (5), 300–313.

(62) Roux, B. *Comput. Phys. Commun.* **1995**, *91* (1-3), 275–282.

(63) Trzesniak, D.; Kunz, A. P. E.; Van Gunsteren, W. F. *ChemPhysChem* **2007**, *8* (1), 162–169.

(64) Laio, A.; Parrinello, M. *Proc. Natl. Acad. Sci. U. S. A.* **2002**, *99* (20), 12562–12566.

(65) Barducci, A.; Bussi, G.; Parrinello, M. *Phys. Rev. Lett.* **2008**, *100* (2), 020603.

(66) Dama, J. F.; Parrinello, M.; Voth, G. A. *Phys. Rev. Lett.* **2014**, *112* (24), 240602.

(67) Megahed, S.; Ebner, W. *J. Power Sources* **1995**, *54* (1), 155–162.

(68) Chung, G.-C.; Kim, H.-J.; Yu, S.-I.; Jun, S.-H.; Choi, J.; Kim, M.-H. *J. Electrochem. Soc.* **2002**, *147* (12), 4391.

(69) Jeong, S.-K.; Inaba, M.; Iriyama, Y.; Abe, T.; Ogumi, Z. *Electrochem. Solid-State Lett.* **2002**, *6* (1), A13.

(70) Jeong, S. K.; Inaba, M.; Iriyama, Y.; Abe, T.; Ogumi, Z. *J. Power Sources* **2003**, *119-121*, 555–560.

(71) Fujimoto, H.; Fujimoto, M.; Ikeda, H.; Ohshita, R.; Fujitani, S.; Yonezu, I. *J. Power Sources* **2001**, *93* (1-2), 224–229.

(72) Shu, Z. X. *J. Electrochem. Soc.* **2006**, *140* (4), 922.

(73) Ding, M. S.; Xu, K.; Jow, T. R. *J. Electrochem. Soc.* **2002**, *147* (5), 1688.

(74) Guyomard, D.; Tarascon, J.-M. *J. Electrochem. Soc.* **1993**, *140* (11), 3071.

(75) Tarascon, J.-M.; Guyomard, D. *Solid State Ionics* **1994**, *69* (3-4), 293–305.

(76) McDowell, M. T.; Lee, S. W.; Nix, W. D.; Cui, Y. *Adv. Mater.* **2013**, *25* (36), 4966–4985.

(77) Lin, D.; Liu, Y.; Cui, Y. *Nat. Nanotechnol.* **2017**, *12* (3), 194–206.

(78) Vatamanu, J.; Borodin, O.; Smith, G. D. *Phys. Chem. Chem. Phys.* **2010**, *12* (1), 170–182.

(79) Jorn, R.; Kumar, R.; Abraham, D. P.; Voth, G. A. *J. Phys. Chem. C* **2013**, *117* (8), 3747–3761.

(80) Boyer, M. J.; Vilčiauskas, L.; Hwang, G. S. *Phys. Chem. Chem. Phys.* **2016**, *18* (40), 27868–27876.

(81) Raguette, L.; Jorn, R. *J. Phys. Chem. C* **2018**, acs.jpcc.7b11472.

(82) Leung, K.; Qi, Y.; Zavadil, K. R.; Jung, Y. S.; Dillon, A. C.; Cavanagh, A. S.; Lee, S.-H.; George, S. M. *J. Am. Chem. Soc.* **2011**, 14741–14754.

(83) Leung, K. *Chem. Phys. Lett.* **2013**, *568-569*, 1–8.

(84) Bard, A. J.; Faulkner, L. *Electrochemical methods: fundamentals and applications*; John Wiley & Sons, 2001.

(85) Banks, C. E.; Davies, T. J.; Wildgoose, G. G.; Compton, R. G. *Chem. Commun. (Camb).* **2005**, No. 7, 829–841.

(86) McDonald, N. A.; Jorgensen, W. L. *J. Phys. Chem. B* **1998**, *102* (41), 8049–8059.

(87) Rizzo, R. C.; Jorgensen, W. L. *J. Am. Chem. Soc.* **1999**, *121* (20), 4827–4836.

(88) Price, M. L. P.; Ostrovsky, D.; Jorgensen, W. L. *J. Comput. Chem.* **2001**, *22* (13), 1340–1352.

(89) Hess, B.; Kutzner, C.; van der Spoel, D.; Lindahl, E. *J. Chem. Theory Comput.* **2008**, *4* (3), 435–447.

(90) Martyna, G. J.; Tobias, D. J.; Klein, M. L. *J. Chem. Phys.* **1994**, *101* (5), 4177–4189.

(91) Martyna, G. J.; Tuckerman, M. E.; Tobias, D. J.; Klein, M. L. *Mol. Phys.* **1996**, *87* (5), 1117–1157.

(92) Tribello, G. A.; Bonomi, M.; Branduardi, D.; Camilloni, C.; Bussi, G. *Comput. Phys. Commun.* **2014**, *185* (2), 604–613.

(93) Paek, E.; Pak, A. J.; Hwang, G. S. *J. Electrochem. Soc.* **2012**, *160* (1), A1–A10.

(94) Pak, A. J.; Paek, E.; Hwang, G. S. *J. Phys. Chem. C* **2014**, *118* (38), 21770–21777.

(95) Rosolen, J. M. *J. Electrochem. Soc.* **1996**, *143* (8), 2417.

(96) Hossain, M. S.; Tryk, D.; Yeager, E. *Electrochim. Acta* **1989**, *34* (12), 1733–1737.

(97) Chernyak, Y. *J. Chem. Eng. Data* **2006**, *51* (2), 416–418.

(98) Cocero, M. J.; Mato, F.; Isaiasgarcia, I.; Cobos, J. C. *J. Chem. Eng. Data* **1989**, *34* (4), 443–445.

(99) Leung, K.; Budzien, J. L. *Phys. Chem. Chem. Phys.* **2010**, *12* (25), 6583.

(100) Vatamanu, J.; Borodin, O.; Smith, G. D. *J. Phys. Chem. C* **2012**, *116* (1), 1114–1121.

(101) Paek, E.; Pak, A. J.; Kweon, K. E.; Hwang, G. S. *J. Phys. Chem. C* **2013**, *117* (11), 5610–5616.

(102) Paek, E.; Pak, A. J.; Hwang, G. S. *J. Chem. Phys.* **2015**, *142* (2), 024701.

(103) Tran, T. D.; Feikert, J. H.; Pekala, R. W.; Kinoshita, K. *J. Appl. Electrochem.* **1996**, *26* (11), 1161–1167.

(104) Bhattacharya, S.; Riahi, A. R.; Alpas, A. T. *Mater. Res. Soc. Symp. Proc.* **2011**, *1388*, 20–25.

(105) Xu, K.; von Cresce, A.; Lee, U. *Langmuir* **2010**, *26* (13), 11538–11543.

(106) Jow, T. R.; Xu, K.; Borodin, O.; Ue, M. *Electrolytes for Lithium and Lithium-Ion Batteries*; Jow, T. R., Xu, K., Borodin, O., Ue, M., Eds.; Modern Aspects of Electrochemistry; Springer New York: New York, NY, 2014; Vol. 58.

(107) Wang, Y.; Nakamura, S.; Ue, M.; Balbuena, P. B. *J. Am. Chem. Soc.* **2001**, *123* (47), 11708–11718.

(108) Yu, J.; Balbuena, P. B.; Budzien, J.; Leung, K. *J. Electrochem. Soc.* **2011**, *158* (4), A400–A410.

(109) Bedrov, D.; Smith, G. D.; van Duin, A. C. T. *J. Phys. Chem. A* **2012**, *116* (11), 2978–2985.

(110) Islam, M. M.; Van Duin, A. C. T. *J. Phys. Chem. C* **2016**, *120* (48), 27128–27134.

(111) Peled, E. *J. Electrochem. Soc.* **1998**, *145* (10), 3482–3486.

(112) Buqa, H.; Würsig, A.; Vetter, J.; Spahr, M. E.; Krumeich, F.; Novák, P. *J. Power Sources* **2006**, *153* (2), 385–390.

(113) Zhang, X.; Kostecki, R.; Richardson, T. J.; Pugh, J. K.; Ross, P. N. *J. Electrochem. Soc.* **2001**, *148* (12), A1341–A1345.

(114) Aurbach, D.; Gofer, Y.; Ben-Zion, M.; Aped, P. *J. Electroanal. Chem.* **1992**, *339* (1-2), 451–471.

(115) Wang, Y.; Nakamura, S.; Tasaki, K.; Balbuena, P. B. *J. Am. Chem. Soc.* **2002**, *124* (16), 4408–4421.

(116) Yu, J.; Balbuena, P. B.; Budzien, J.; Leung, K. *J. Electrochem. Soc.* **2011**, *158* (4), 400–410.

(117) Dedryvère, R.; Gireaud, L.; Grugeon, S.; Laruelle, S.; Tarascon, J.-M.; Gonbeau, D. *J. Phys. Chem. B* **2005**, *109* (33), 15868–15875.

(118) Borodin, O.; Zhuang, G. V.; Ross, P. N.; Xu, K. *J. Phys. Chem. C* **2013**, *117* (15), 7433–7444.

(119) Malmgren, S.; Rensmo, H.; Gustafsson, T.; Gorgoi, M.; Edström, K. *ECS Trans.* **2010**, *25* (36), 201–210.

(120) Bryngelsson, H.; Stjerndahl, M.; Gustafsson, T.; Edström, K. *J. Power Sources* **2007**, *174* (2), 970–975.

(121) Ota, H.; Sakata, Y.; Inoue, A.; Yamaguchi, S. *J. Electrochem. Soc.* **2004**, *151* (10), A1659–A1669.

(122) Becke, A. D. *Phys. Rev. A* **1988**, *38*, 3098–3100.

(123) Lee, C.; Yang, W.; Parr, R. G. *Phys. Rev. B* **1988**, *37*, 785–789.

(124) Perdew, J. P.; Burke, K.; Ernzerhof, M. *Phys. Rev. Lett.* **1996**, *77* (18), 3865–3868.

(125) Frisch, M. J.; Trucks, G. W.; Schlegel, H. B.; Scuseria, G. E.; Robb, M. A.; Cheeseman, J. R.; Scalmani, G.; Barone, V.; Petersson, G. A.; Nakatsuji, H.; Li, X.; Caricato, M.; Marenich, A. V.; Bloino, J.; Janesko, B. G.; Gomperts, R.; Mennucci, B.; Hratchian, H. P.; Ortiz, J. V.; Izmaylov, A. F.; Sonnenberg, J. L.; Williams-Young, D.; Ding, F.; Lipparini, F.; Egidi, F.; Goings, J.; Peng, B.; Petrone, A.; Henderson, T.; Ranasinghe, D.; Zakrzewski, V. G.; Gao, J.; Rega, N.; Zheng, G.; Liang, W.; Hada, M.; Ehara, M.; Toyota, K.; Fukuda, R.; Hasegawa, J.; Ishida, M.; Nakajima, T.; Honda, Y.; Kitao, O.; Nakai, H.; Vreven, T.; Throssell, K.; Montgomery, J. A., J.; Peralta, J. E.; Ogliaro, F.; Bearpark, M. J.; Heyd, J. J.; Brothers, E. N.; Kudin, K. N.; Staroverov, V. N.; Keith, T. A.; Kobayashi, R.; Normand, J.; Raghavachari, K.; Rendell, A. P.; Burant, J. C.; Iyengar, S. S.; Tomasi, J.; Cossi, M.; Millam, J. M.; Klene, M.; Adamo, C.; Cammi, R.; Ochterski, J. W.; Martin, R. L.; Morokuma, K.; Farkas, O.; Foresman, J. B.; Fox, D. J. Gaussian 16, Revision A. 03, 2016.

(126) Miertus, S.; Scrocco, E.; Tomasi, J. *Chem. Phys.* **1981**, *55*, 117–129.

(127) Bayly, C. I.; Cieplak, P.; Cornell, W.; Kollman, P. A. *J. Phys. Chem.* **1993**, *97* (40), 10269–10280.

(128) R. Car; Parrinello, M. *Phys. Rev. Lett.* **1985**, *55*, 2471–2474.

(129) Http://www.cpmd.org/. CPMD.

(130) Goedecker, S.; Teter, M.; Hutter, J. *Phys. Rev. B* **1996**, *54* (3), 1703–1710.

(131) Troullier, N.; Martins, J. L. *Phys. Rev. B* **1991**, *43* (3), 1993–2006.

(132) Bonomi, M.; Branduardi, D.; Bussi, G.; Camilloni, C.; Provasi, D.; Raiteri, P.; Donadio, D.; Marinelli, F.; Pietrucci, F.; Broglia, R. A.; Parrinello, M. *Comput. Phys. Commun.* **2009**, *180* (10), 1961–1972.

(133) Borodin, O.; Smith, G. D. *J. Phys. Chem. B* **2009**, *113* (6), 1763–1776.

(134) Ong, M. T.; Verners, O.; Draeger, E. W.; Van Duin, A. C. T.; Lordi, V.; Pask, J. E. *J. Phys. Chem. B* **2015**, *119* (4), 1535–1545.

(135) Halls, M. D.; Tasaki, K. *J. Power Sources* **2010**, *195* (5), 1472–1478.

(136) Han, Y.-K.; Moon, Y.; Lee, K.; Huh, Y. S. *Curr. Appl. Phys.* **2014**, *14* (6), 897–900.

(137) Cheng, L.; Assary, R. S.; Qu, X.; Jain, A.; Ong, S. P.; Rajput, N. N.; Persson, K.; Curtiss, L. A. *J. Phys. Chem. Lett.* **2015**, *6* (2), 283–291.

(138) Dahbi, M.; Ghamouss, F.; Tran-Van, F.; Lemordant, D.; Anouti, M. *J. Power Sources* **2011**, *196* (22), 9743–9750.

(139) Lee, S.-B.; Pyun, S.-I. *Carbon N. Y.* **2002**, *40*, 2333–2339.

(140) Abraham, M. J.; Murtola, T.; Schulz, R.; Páll, S.; Smith, J. C.; Hess, B.; Lindah, E. *SoftwareX* **2015**, *1-2*, 19–25.

(141) Han, S.; Borodin, O.; Seo, D. M.; Zhou, Z. *J. Electrochem. Soc.* **2014**, *161* (14), 2042–2053.

(142) Zhuang, G. V.; Ross, P. N. *Electrochem. Solid-State Lett.* **2003**, *6* (7), A136–A139.

(143) Zhuang, G. V; Yang, H.; Ross, P. N.; Xu, K.; Jow, T. R. *Electrochem. Solid-State Lett.* **2006**, *9* (2), A64–A68.

(144) Xu, K.; Zhuang, G. V.; Allen, J. L.; Lee, U.; Zhang, S. S.; Ross, P. N.; Jow, T. R. *J. Phys. Chem. B* **2006**, *110* (15), 7708–7719.

(145) Novák, P.; Joho, F.; Lanz, M.; Rykart, B.; Panitz, J.-C.; Alliata, D.; Kötz, R.; Haas, O. *J. Power Sources* **2001**, *97-98*, 39–46.

(146) Lanz, M.; Novák, P. *J. Power Sources* **2001**, *102* (1-2), 277–282.

(147) Dedryvère, R.; Leroy, S.; Martinez, H.; Blanchard, F.; Lemordant, D.; Gonbeau, D. *J. Phys. Chem. B* **2006**, *110* (26), 12986–12992.

(148) Ushirogata, K.; Sodeyama, K.; Futera, Z.; Tateyama, Y.; Okuno, Y. *J. Electrochem. Soc.* **2015**, *162* (14), A2670–A2678.

(149) Fujie, T.; Takenaka, N.; Suzuki, Y.; Nagaoka, M. *J. Chem. Phys.* **2018**, *149* (4), 044113.

(150) Boyer, M. J.; Hwang, G. S. *Electrochim. Acta* **2018**, *266*, 326–331.

(151) Boyer, M. J.; Hwang, G. S. *J. Phys. Chem. C* **2019**, *123* (29), 17695–17702.

(152) Takenaka, N.; Suzuki, Y.; Sakai, H.; Nagaoka, M. *J. Phys. Chem. C* **2014**, *118* (20), 10874–10882.

(153) Takenaka, N.; Fujie, T.; Bouibes, A.; Yamada, Y.; Yamada, A.; Nagaoka, M. *J. Phys. Chem. C* **2018**, *122*, 2564–2571.

(154) Wang, Y.; Balbuena, P. B. *Int. J. Quantum Chem.* **2005**, *102* (5), 724–733.

Vita

Mathew J. Boyer was born in Reading, PA and received his primary education in Saint Clair, PA and his secondary education in Pottsville, PA where he graduated in 2010. He attended Lehigh University in Bethlehem, PA where he received his B.S. in Chemical Engineering graduating with Highest Honors in 2014. In August 2014, he began his graduate studies at the University of Texas at Austin in the McKetta Department of Chemical Engineering in pursuance of a doctorate in Chemical Engineering.

Permanent address (or email): mat_boyer@outlook.com

This dissertation was typed by Mathew J. Boyer.